UNIVERSIDADE ESTADUAL DE CAMPINAS
Instituto de Física Gleb Wataghin

HÍTALO RODRIGUES MENDES

Inclusion of charge carriers creation and transport in semiconductor detectors in the PENELOPE Monte Carlo simulation code: effects on the radiographic image formation.

Inclusão da criação e transporte de portadores de carga em detectores semicondutores no código de simulação Monte Carlo PENELOPE: efeitos na formação da imagem radiográfica.

Campinas
2023

Hítalo Rodrigues Mendes

Inclusion of charge carriers' creation and transport in semiconductor detectors in the PENELOPE Monte Carlo code: effects on the radiographic image formation.

Inclusão da criação e transporte de portadores de carga em detectores semicondutores no código de simulação Monte Carlo PENELOPE: efeitos na formação da imagem radiográfica.

Thesis presented to the Institute of Physics Gleb Wataghin of the University of Campinas in partial fulfillment of the requirements for the degree of Doctor in Science, in the area of Applied Physics.

Tese apresentada ao Instituto de Física Gleb Wataghin da Universidade Estadual de Campinas como parte dos requisitos exigidos para a obtenção do título de Doutor em Ciências, na área de Física Aplicada.

Supervisor: Prof Dra. Alessandra Tomal

Este exemplar corresponde à versão final da tese defendida pelo aluno Hítalo Rodrigues Mendes, e orientada pela Prof Dra. Alessandra Tomal.

CAMPINAS
2023

Ficha catalográfica
Universidade Estadual de Campinas
Biblioteca do Instituto de Física Gleb Wataghin
Lucimeire de Oliveira Silva da Rocha - CRB 8/9174

M522i

Mendes, Hítalo Rodrigues, 1993-
Inclusion of charge carriers creation and transport in semiconductor detectors in the PENELOPE Monte Carlo simulation code : effects on the radiographic image formation / Hítalo Rodrigues Mendes. – Campinas, SP : [s.n.], 2023.

Orientador: Alessandra Tomal.
Tese (doutorado) – Universidade Estadual de Campinas, Instituto de Física Gleb Wataghin.

1. Método de Monte Carlo. 2. Radiologia. 3. Detectores nucleares de semicondutor. I. Tomal, Alessandra, 1983-. II. Universidade Estadual de Campinas. Instituto de Física Gleb Wataghin. III. Título.

Informações Complementares

Título em outro idioma: Inclusão da criação e transporte de portadores de carga em detectores semicondutores no código de simulação Monte Carlo PENELOPE : efeitos na formação da imagem radiográfica
Palavras-chave em inglês:
Monte Carlo method
Radiology
Semiconductor nuclear counters
Área de concentração: Física Aplicada
Titulação: Doutor em Ciências
Banca examinadora:
Alessandra Tomal [Orientador]
Rickson Coelho Mesquita
Mario Antonio Bernal Rodriguez
Ana Paula Perini
Maurício Moralles
Data de defesa: 18-05-2023
Programa de Pós-Graduação: Física

Identificação e informações acadêmicas do(a) aluno(a)
- ORCID do autor: https://orcid.org/0000-0002-1097-1295
- Currículo Lattes do autor: http://lattes.cnpq.br/5485787721130965

MEMBROS DA COMISSÃO EXAMINADORA DA TESE DE DOUTORADO DO ALUNO HÍTALO RODRIGUES MENDES - RA 140672 APRESENTADA E APROVADA AO INSTITUTO DE FÍSICA GLEB WATAGHIN, DA UNIVERSIDADE ESTADUAL DE CAMPINAS, EM 18/05/2023.

COMISSÃO JULGADORA:

- Profa. Dra. Alessandra Tomal – Presidente e orientadora (IFGW/UNICAMP)

- Prof. Dr. Rickson Coelho Mesquita (IFGW/UNICAMP)

- Prof. Dr. Mario Antonio Bernal Rodriguez (IFGW/UNICAMP)

- Dra. Ana Paula Perini (Universidade Federal de Uberlândia – Instituto de Física)

- Dr. Maurício Moralles (Instituto de Pesquisas Energéticas e Nucleares - IPEN)

OBS.: Ata da defesa com as respectivas assinaturas dos membros encontra-se no SIGA/Sistema de Fluxo de Dissertação/Tese e na Secretaria do Programa da Unidade.

CAMPINAS

2023

Acknowledgments

I would like to express my heartfelt gratitude and appreciation to William, whose unwavering support, dedication, and companionship have played a pivotal role in shaping my academic journey over the course of these years. Your presence as a partner has been a constant source of encouragement, motivation, and strength, and I am truly grateful for the unwavering support you have provided.

My parents hold a special place in my heart, and their unconditional love, guidance, and constant encouragement have been the driving force behind my accomplishments. I am deeply grateful for their presence and support. Their words of encouragement, gestures of support, and presence have made a significant difference in my life.

I would like to extend my heartfelt appreciation to Prof. Dr. Alessandra Tomal for her invaluable guidance, assistance, teachings, patience, and mentorship throughout the entirety of this research. Her expertise, insights, and support have been instrumental in shaping my understanding, refining my research skills, and navigating the challenges encountered along the way.

I am sincerely grateful to my esteemed colleagues in the Medical Radiological Physics Group, with special mention to Rodrigo and Giovanna. Their collaboration, shared experiences, and discussions have enriched my research journey in countless ways. Their unwavering support and willingness to lend a helping hand have made this endeavor more rewarding and enjoyable.

I am deeply grateful to the esteemed professors of the Postgraduate Physics program for their contributions to my education. I am truly fortunate to have had the opportunity to learn from their wealth of knowledge and experience. To the dedicated and efficient staff at the Postgraduate Office, I extend my sincere thanks for their prompt assistance, professionalism, and unwavering support whenever I sought their guidance. I would like to express my deepest appreciation to Maria Emília Seren Takahashi, for her exceptional assistance throughout the duration of the project. Her guidance, expertise, and generosity in sharing resources have been invaluable in the successful completion of this research. The opportunity to work alongside her and benefit from her vast knowledge and experience has been a privilege, and I am truly grateful for her unwavering commitment to my success.

To my fellow Postgraduate colleagues, Danelise, Luís, Pedro, and Gabriela, I extend my heartfelt gratitude for their invaluable assistance, camaraderie, and unwavering support. We have not only shared academic endeavors but have also forged deep friendships and created unforgettable memories throughout the years. From late-night study sessions to celebratory gatherings at bars and restaurants, we have experienced the ups

and downs of this journey together. We have laughed, celebrated milestones, and supported each other through various life events, from New Year's Eve parties to weddings. These shared experiences and cherished moments have strengthened our bond and made our time together truly memorable. I am grateful for their enduring friendship and for being the companions I could rely on during this remarkable journey.

I would like to express my sincere appreciation to my undergraduate colleagues, especially Carlos, Lucas, and Marcelli, for their friendship, support, and camaraderie throughout the years. You have become dear friends, who have been a part of my life for over ten years, I am profoundly grateful for your enduring presence and support.

This project received financial support from the Ministry of Science, Technology and Innovation” and the “National Council for Scientific and Technological Development (CNPq Process 140629/2018-1).

“Quanto mais aumenta nosso conhecimento, mais evidente fica nossa ignorância”.
John F. Kennedy

Resumo

A radiografia de tórax é um exame comumente realizado que se tornou especialmente importante durante a pandemia de COVID-19. Devido aos riscos associados à exposição à radiação ionizante, estudos que se concentram na aquisição e otimização de imagens radiográficas usam métodos computacionais, em especial a simulação Monte Carlo (MC) variando diferentes parâmetros e tecnologias sem expor pacientes. No entanto, a maioria dos códigos MC sobrestimam a resolução espacial de detectores e modelam as etapas de detecção apenas considerando o ruído quântico, sem incluir outras componentes de ruído presentes em um detector real. Como resultado, um modelo de detector mais realista pode afetar significativamente a qualidade da imagem final. Além disso, uma modelagem mais realista da detecção por simulação MC é dificultada porque vários códigos, por exemplo o PENELOPE, não simulam campos elétricos e a estrutura cristalina em sólidos, que são parâmetros importantes a serem considerados em um detector real. Este estudo se concentra na implementação das etapas de criação e transporte de pares elétron-buraco (*EHP*) em detectores semicondutores no código MC PENELOPE e avaliar o impacto da modelagem detalhada do processo de detecção na aquisição e otimização de tecnologia de imagens. A inclusão do transporte de cargas no código PENELOPE foi chamada de THOR (*Transport of electrons and HOles in semiconductoRs*). Dentre os materiais de detecção, os semicondutores foram escolhidos pois são um dos materiais mais usados em radiografia devido a sua característica de converter raios X em carga elétrica diretamente, resultando em menos perdas no processo de detecção. O código THOR foi validado usando estudos na literatura por meio das grandezas: Fator Swank, Função de Transferência de Modulação (*MTF*), Espectro de Potência de Ruído (*NPS*) e Eficiência Quântica Detecção (*DQE*), resultando em diferenças relativas inferiores às incertezas de simulação. Além disso, o código foi usado para explorar diferentes características dos detectores: material e espessura do sensor, tamanho de pixel e campo elétricos aplicados. Para quantificar influência na aquisição de imagens, foram realizadas simulações usando os códigos sem e com o transporte de *EHP*. A geometria de simulação consistiu em objetos simuladores homogêneos compostos de tecido mole, dois modos de detecção (integração de energia e contagem de fótons), dois materiais de detecção (a-Se e CdTe) e feixes polienergéticos. As imagens foram avaliadas usando o contraste, relação sinal-ruído (*SNR*) e relação contraste-ruído (*CNR*). Além disso, o histograma do valor do pixel de cada imagem foi construído para explorar as diferenças entre os códigos e usar técnicas de processamento de imagem, como janelamento de histograma para aumentar o contraste. Portanto, a inclusão do transporte *EHP* na simulação do detector resulta em mudanças nas imagens radiográficas tanto qualitativa quanto quantitativamente. Além disso, o código THOR desenvolvido neste trabalho pode ser usado para explorar novos tipos e configurações de detectores, mostrando possibilidades promissoras além do escopo deste trabalho.

Palavras-chave: simulação Monte Carlo, radiografia, pares elétron-buraco, detectores semicondutores, contadores de fótons, integradores de energia.

Abstract

Chest radiography is a commonly performed exam that has become especially important during the COVID-19 pandemic. Due to the risks associated with exposure to ionizing radiation, studies that focus on the acquisition and optimization of radiographic images use computational methods, especially Monte Carlo (MC) simulation, varying different parameters and technologies without exposing patients. However, most MC codes overestimate the detector's spatial resolution and model the detection steps only considering quantum noise, without including other noise components present in a real detector. As a result, a more realistic detector model can significantly affect the quality of the final image. Furthermore, more realistic modeling of detection by MC simulation is difficult because several codes, for example, PENELOPE, do not simulate electric fields and the crystalline structure in solids, which are important parameters to be considered in a real detector. This study focuses on the implementation of the creation and transport steps of electron-hole pairs (*EHP*) in semiconductor detectors in the MC PENELOPE code and evaluates the impact of detailed modeling of the detection process on the acquisition and optimization of imaging technology. The inclusion of charge transport in the PENELOPE code was called THOR (*Transport of electrons and HOles in semiconductoRs*). Among the detection materials, semiconductors were chosen because they are one of the most used materials in radiography due to their characteristic of directly converting X-rays into electrical charge, resulting in less loss in the detection process. The THOR code was validated using studies in the literature through the magnitudes: Swank Factor, Modulation Transfer Function (*MTF*), Noise Power Spectrum (*NPS*), and Detective Quantum Efficiency (*DQE*), resulting in relative differences lower than the simulation uncertainties. Furthermore, the code was used to explore different characteristics of the detectors: sensor material and thickness, pixel size and applied electric fields. To quantify the influence on image acquisition, simulations were performed using the codes with and without *EHP* transport. The simulation geometry consisted of homogeneous phantom objects composed of soft tissue, two detection modes (energy integration and photon counting), two detection materials (a-Se and CdTe) and polyenergetic beams. Images were evaluated using contrast, signal-to-noise ratio (*SNR*) and contrast-to-noise ratio (*CNR*). Furthermore, the histogram of the pixel value of each image was constructed to explore the differences between the codes and use image processing techniques such as histogram windowing to increase the contrast. Therefore, the inclusion of the *EHP* transport in the detector simulation results in changes in the radiographic images both qualitatively and quantitatively. Furthermore, the THOR code developed in this work can be used to explore new types and configurations of detectors, showing promising possibilities beyond the scope of this work.

Keywords: Monte Carlo simulation, radiography, electron-hole pairs, semiconductor detectors, photon-counting, energy integrating.

List of Figures

List of Tables

List of Abbreviations

Abbreviation	**Definition**
ARTEMIS	pArticle transport, Recombination, and Trapping in sEM-conductor Imaging Simulations
CNR	Contrast-to-Noise Ratio
CR	Computed Radiography
DCS	Differential Cross Section
DQE	Detective Quantum Efficiency
DR	Digital Radiology
EHP	Electron-Hole Pair
EI	Energy Integrating
ESF	Edge Spread Function
FOM	Figure of Merit
LSF	Line Spread Function
MAD	Mean Absorbed Dose
MC	Monte Carlo
MCGPU	Monte Carlo on Graphics Processing Units
MTF	Modulation Transfer Function
NPS	Noise Power Spectrum
PCD	Photon Counting Detector
PENELOPE	PENetration and Energy LOss of Positrons and Electrons
PHS	Pulse-Height Spectrum
PSF	Point Spread Function
SNR	Signal-to-Noise Ratio
THOR	Transport of electrons and HOles in semiconductoRs

List of Symbols

Symbol	Definition
C_1	average angular deflection produced by multiple elastic scatterings
C_2	maximum average fractional energy loss between consecutive hard elastic events
$EABS$	energy threshold for particle absorption in MC simulation
E	photon energy
E_{dep}	Energy deposited
E_g	energy bandgap
$ethr$	energy thereshold
f	spatial frequency
F	applied electric field
K_{air}	air kerma
I	Swank Factor
L	detector thickness
WCC	cut-off energy for inelastic hard collisions
WCR	cut-off energy for Bremsstrahlung emission
$W_{\pm}$	energy necessary to create an electron-hole pair
μ	attenuation coefficient
δ	attenuation depth
μ_e	electron mobility
μ_h	hole mobility
τ_e	electron lifetime
τ_h	hole lifetime
η	quantum efficiency

Contents

Chapter 1

Introduction

The field of radiology, which originated with Wilhelm Conrad Roentgen's discovery of X-rays in 1895 [1], has revolutionized medical imaging and diagnosis. Roentgen's accidental finding of X-rays, opened up new possibilities for visualizing the human body's internal structures without the need for invasive procedures [2, 3]. Over the years, the technology behind radiology has undergone remarkable advancements. Early X-ray machines were bulky, required long exposure times, and posed significant radiation risks to both patients and operators. However, as the field progressed, improvements in X-ray tube design, image detectors, and radiation protection measures resulted in safer and more efficient imaging techniques [3, 4].

Among the most frequent examinations in radiology, chest X-rays stand out [5], and are used mainly to detect pneumonia, airway infection, lung cancer, and trauma [6, 7]. In the world, 236 chest X-rays per 1000 patients are obtained yearly [8]. In Brazil, only in 2022, over 20 million chest X-rays were performed [9]. Due to the COVID-19 pandemic, there was an even greater interest in chest X-rays for screening, diagnosis, and management of patients with suspected or known COVID-19 infection [10]. However, the use of ionizing radiation results in negative effects on the biologic tissue. [11–13]. In the case of children, since they have a longer life expectancy, there is a larger probability of adverse effects of radiation occurrence [11, 14]. But there is a necessity to perform chest X-ray exams in children, since pneumonia is largely responsible for infant mortality, representing 13 and 19% of deaths in children under 5 years of age in Brazil [15] and the world [16], respectively. In this scenario of risk (adverse effects of ionizing radiation) versus benefit (the possibility of a diagnosis), the X-ray exams optimization is essential, aiming to obtain an image with the highest quality by adjusting the dose deposited in the patient, following the ALARA principle (*As Low As Reasonable Achievable*) [11, 17].

In recent decades, with the development of digital detectors, there has been an important migration to this type of technology, which has many advantages, such as ease of storage, the possibility of carrying out computational image processing, and greater detection efficiency, enabling the reduction in the dose deposited in the patient [18].

Furthermore, in digital radiography, the process of obtaining images for diagnosis consists of three independent steps: image acquisition, processing, and visualization [18]. The first step includes the patient's exposure to X-rays and radiation detection, meaning that all the physics of X-rays interaction with the matter occurs in this stage. In the second step, computational algorithms are used to increase the image quality, for instance, histogram equalization and windowing to reduce noise and increase the contrast, respectively [19]. The third step consists of the radiography visualization in high-resolution monitors [2, 18]. Figure 1.1 illustrate the three independent steps for the process of obtaining images.

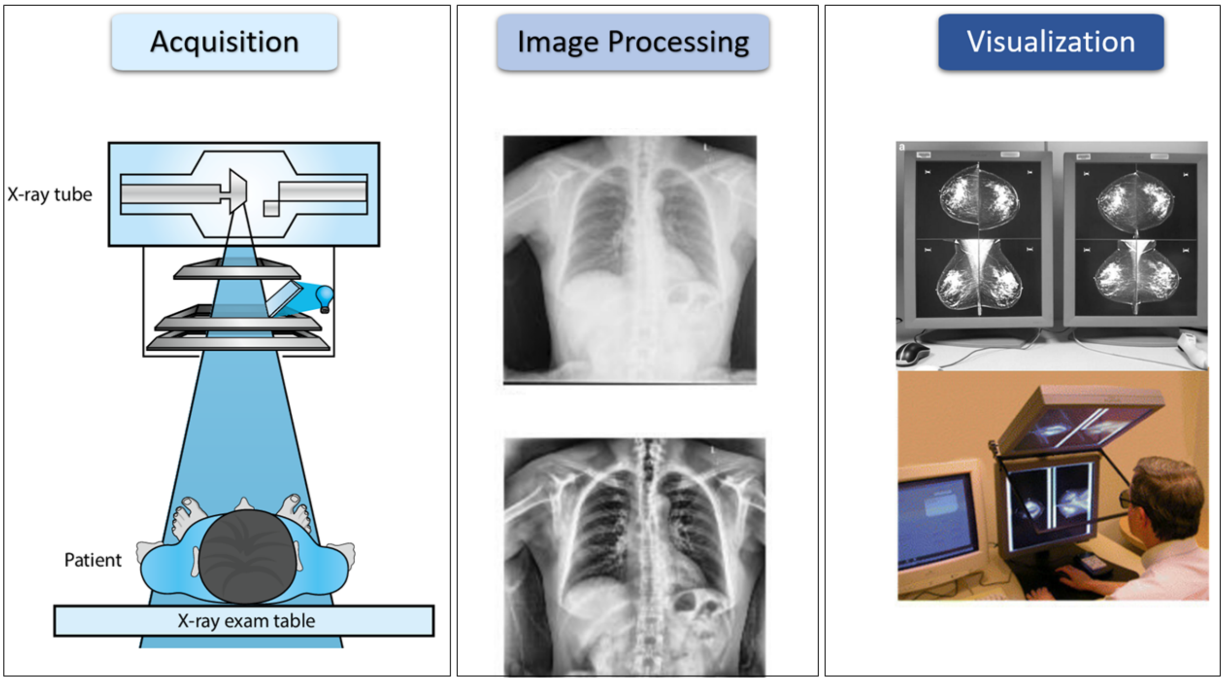

Figure 1.1: The three independent steps for the process of obtaining images for diagnosis: image acquisition, processing, and visualization. Source: adapted from Alexander [20], Dovganich et al. [21], Haygood et al. [22], Chistyakov et al. and [23].

One of the most important features to consider in the image acquisition step is the radiation detection process. The main objective of digital detection is to convert the X-rays leaving the body to an electrical signal [24], which can be based on different technologies. Figure 1.2 illustrate the propagation of the signal through the various energy conversion stages of an imaging system. The initial number of photons (N_0) reach the detector where the probability of interaction depends on the detector material and thickness [2, 25]. The fluctuation of the quanta interacting defines the signal-to-noise ratio (SNR) of the imaging system which increases as the square root of the number of quanta interacting with the detector [26]. The maximum SNR of the imaging system will occur at this point. However, since each detection technology has distinct processes to convert the X-rays into charge, either directly or indirectly, the SNR will reduce as the passage of the signal through the imaging system because gains and losses, g_1 and g_2 on Figure 1.2, respectively.

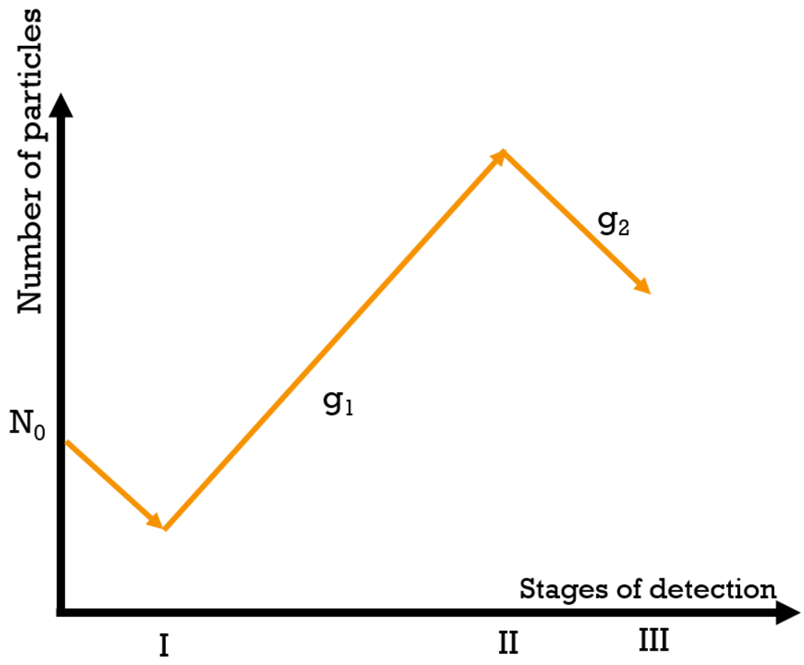

Figure 1.2: Number of quanta or charges at different stages in an imaging system, showing the gains and losses at each stage. Source: adapted from Yaffe and Rowlands [26].

The main digital detector technologies are computed radiography (CR) detectors, indirect and direct digital radiology (DR) detectors, and photon counting detectors (PCD) [2, 25]. CR and DR detectors are energy-integrating detectors, meaning that the signal is proportional to the absorbed energy from X-rays [27]. The CR detectors use photostimulable phosphors in which a fraction of the absorbed energy from X-rays is trapped and can be read out later using a laser light [2, 28]. DR is divided into indirect and direct. The first uses a combination of a layer of scintillator material and a semiconductor [25]. The scintillator converts X-ray into photons in the visible portion of the electromagnetic spectrum, and these photons are converted into charge [24] by the semiconductor layer. For direct DR, photoconductors are used to convert the X-rays directly into charge, avoiding losses in the detection process [29]. PCDs also use photoconductors to convert the X-ray into charge, but for each electrical pulse produced by a photon, thresholds are implemented and only if the pulse height is above this threshold a photon is counted [27, 30]. Therefore, PCDs have information about the photons' energy, being possible to use different thresholds and produce multi-energy (spectral) images with only one exposure [31].

Monte Carlo (MC) simulation is a valuable tool to study the process of detection in radiology because it does not present limitations to evaluate a large number of exposure conditions and physical parameters compared to experimental methods [32, 33]. However, most studies focused on the simulation of image acquisition and optimization simulate only the transport of photons and electrons in the detector (stage I on Figure 1.2), but not the entire process to convert the X-ray into an electrical signal [34–36]. This can result in an overestimation of the spatial resolution and disregarding sources of image noise. This limitation in MC codes exists because most codes used in Medical Physics, for instance, the PENELOPE code [37], do not simulate electrical field (used mainly in direct DR) and the crystalline structure in solids.

Currently, with the advent of virtual clinical trials (VCT) in radiology, there is an increase in the interest in generating images via MC simulation to optimize imaging protocols, improve image quality, to develop and test new imaging technologies and techniques [38]. VCTs are conducted entirely in a digital environment, without the need for physical patient contact or the collection of physical samples [39]. For instance, the U.S. Food and Drug Administration (FDA) has been exploring the use of VCT in mammography as a means of accelerating the approval process for new mammography devices and imaging technologies [40]. However, to conduct these trials is necessary to simulate images as realistic as possible considering both anthropomorphic phantoms to model the body and to simulate in detail the detection process.

This study focuses on evaluating the impact of the detection process detailed modeling on the acquisition and optimization of imaging. Among the digital detectors used in radiology, semiconductors (direct DR and PCD) was the focus of this work because they are the state of art [27, 30, 41]. Especially in the case of PCD, which had been of great interest due to its improvements in spatial resolution (via smaller detector pixel design), permitting multi-energy imaging and eliminating electronic noise and reducing artifacts, due to the use of energy thresholds [41]. To model the detection process in detail, the creation and transport of electron-hole pairs (*EHP*) in semiconductors was included in the PENELOPE MC code [37] and the penEasy v. 2015 [42] extension. The PENELOPE was chosen because it is freely distributed and open source, has a clear and well-documented structure and is validated in the energy range of interest [37]. The penEasy extension was chosen because of its possibility to separate the simulation results into tallies, where each tally can be enabled or disabled if the user chooses. The penEasy tallies can be used for medical imaging, dosimetry and studying each interaction in the detection process. The tally of interest for the simulation of radiographic images is the "Tally Pixelated Imaging Detector" (PID) which simulates the generation of pixelated images considering different detector types, number of pixels and detection modes. In addition, the PENELOPE code was chosen because the research group has collaborative projects with code developers [43]. The inclusion of *EHP* creation and transport was made in the tally PID and it was named THOR (Transport of electrons and HOles in semiconductoRs). Validation of the THOR code was made using studies in the literature. With the THOR code different exposure conditions, detector materials, thicknesses and pixel size can be simulated. The detectors simulated in this work were characterized by the Swank Factor, Modulation Transfer Function (*MTF*), Noise Power Spectrum (*NPS*) and Detective Quantum Efficiency (DQE). Furthermore, the impact of the detailed modeling of detectors in the image acquisition was evaluated by comparing the pixel value histograms, the quantification of image quality via contrast, signal-to-noise ratio (SNR) and contrast-to-noise ratio (CNR).

The thesis is organized as follows:

Chapter 2 describes the theoretical foundations, including the main types of digital detectors and the metrics used to characterize them.

Chapter 3 includes a literature review of the main studies in the detailed simulation of digital detection, image acquisition and optimization studies.

Chapter 4 describes the detailed model for the creation and transport of *EHP* in direct DR and PCDs including the implementation on the Monte Carlo code.

Chapter 5 contains the model *EHP* transport model validation, the methodology and the results to characterize a detector in terms of noise, efficiency, spatial and energy resolution.

Chapter 6 focuses on the impact of detailed detector simulation in image acquisition and optimization studies.

Finally, chapter 7 presents the conclusions of this work and future perspectives.

Chapter 2

Background

This chapter briefly describes the electron and photon transport via *MC* simulation. Moreover, the physics for image formation in the main digital radiography detectors and the quantities used to characterize a detector in terms of efficiency, noise, energy, and spatial resolution are presented.

2.1 Monte Carlo simulation of radiation transport

MC simulation uses sampling of random numbers and statistical models to estimate mathematical functions and operations of complex systems [33]. In Medical Physics, the *MC* is used to simulate the transport of ionizing radiation to obtain dosimetric quantities and produce images [32].

In this work, the PENELOPE MC code v. 2014 [37] code with the penEasy v. 2015 [42] extension were used to simulate the transport of photons and electrons. PENELOPE is an acronym for *PENetration and Energy LOss of Positrons and Electrons* (photon simulations were included after the code was created in 1996) [37].

Photons and electrons can undergo numerous competing interactions with matter in which energy is lost and secondary particles are produced. This gives rise to a cascade of events called the particle history [37]. Quantitative information on the radiation transport can be obtained by averaging over all simulated histories. With the differential cross section (*DCS*) is possible to characterize each interaction and create probability distributions that are dependent on the particle energy and angle [44]. The *DCS* has dimensions of area/(solid angle $(\Omega)\times$ energy(E)). The atomic *DCS*s adopted in the PENELOPE code are a combination of analytical functions and using numerical tables [37]. Moreover, MC simulation operates using the principle that ionizing radiation can be modeled as a Markov process, meaning that future values of an interaction event are only determined by present parameters. For instance, to determine which interaction will occur to an electron is necessary to know only the particle's present position, direction, and energy, information about how this electron was created and how many interactions already went through are not relevant. Therefore, it is possible to stop the particle simulation at any point and resume from this state without introducing any bias in the results.

A simulation starts by defining the initial particle type, energy, position and direction, the number of histories, the maximum simulation time, and the geometry form and composition. A history ends when the primary and secondary particles are absorbed, the simulation finishes either when the maximum number of histories or the maximum simulation time is reached. Figure 2.1 shows a flowchart of the photon history simulation. Since the focus of this work was to simulate the image formation in radiography, the flowchart in Figure 2.1 was constructed using photons as the initial particle. However, in the PENELOPE code, electrons and positrons can also be the initial particle.

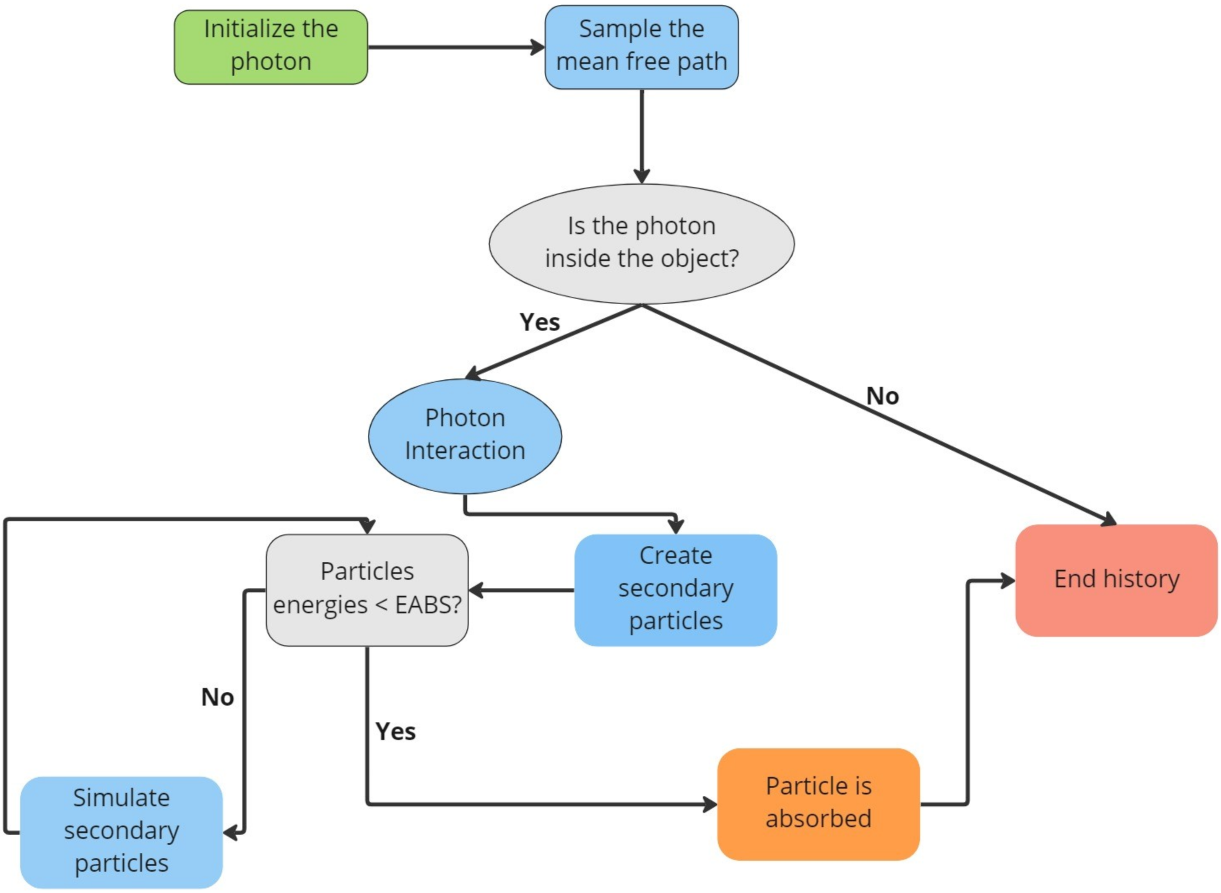

Figure 2.1: Flowchart of the Monte Carlo simulation process presenting the sampling of mean free path, determination of which interaction will occur, creation of secondary particles and the criteria for ending a story.

The next sections show a description of photon and electron simulation in the PENELOPE code. The types of interactions that will be presented are the ones relevant for the energies used in radiography (40 to 150 keV [2]), even though the PENELOPE code energy range is from 50 eV to 1 GeV.

2.1.1 Simulation of photons

The simulation of a photon starts by defining its energy, and randomly choosing its initial directions. The photon's mean free path is sampled using the equation:

$$s = \frac{1}{\mu} ln(1 - \epsilon), \tag{2.1}$$

where μ is the linear attenuation coefficient and ϵ is a random number between 0 and 1. If s is larger than the object size there is no interaction, and if s is lower, a type of interaction is sampled. If in a simulation there are two or more objects, when a particle arrives at the interface between them, it is stopped at the interface and the simulation continues with the interaction properties of the new medium. Meaning that a new mean free path is sampled with the μ referent to the new medium.

The possible photon interactions for the energy range usually used in radiology are the photoelectric absorption, coherent (Rayleigh) and incoherent (Compton) scatterings [2]. In the photoelectric absorption, a photon transfers all of its energy to an atom, ionizing it. As a result, an electron is ejected and its kinetic (E_e) is given as the difference between the energy that the photon (E) and the electron binding energy to the atom (U_i) [45]. As a consequence of the photoelectric effect, there is a vacancy in the atom that can be filled by an electronic rearrangement. In this process, excess energy is released via characteristic X-rays (fluorescence) or *Auger* electrons. Coherent or elastic scattering is an interaction process where the incident photon is deflected from its path without transferring energy and momentum to the electrons in the medium [45], this scattering occurs preferentially for small angles [45]. In Compton scattering, the incident photon of energy E transfers part of its energy to a weakly bound electron in the atom. The photon is then scattered with an energy E' at an angle θ in relation to its initial direction, while the electron will be ejected at an angle θ_e with an energy E_e [46]. The photon energy is never completely converted into electron energy, that is, in a Compton scattering there will always be an electron and a photon as secondary particles. Figure 2.2 shows the kinematics of each photon interaction described.

The μ present in the equation 2.1 is the sum of each interaction cross sections, as shown in:

$$\mu = \tau + \sigma_C + \sigma_R, \tag{2.2}$$

where τ is referent to the photoelectric effect, σ_C to the Compton scattering, σ_R to the coherent scattering [47]. The ratio between the cross-section for an interaction and the total attenuation coefficient is the probability of that interaction occurring [37].

In the MC simulation, the *DCS* for each interaction type is used to determine

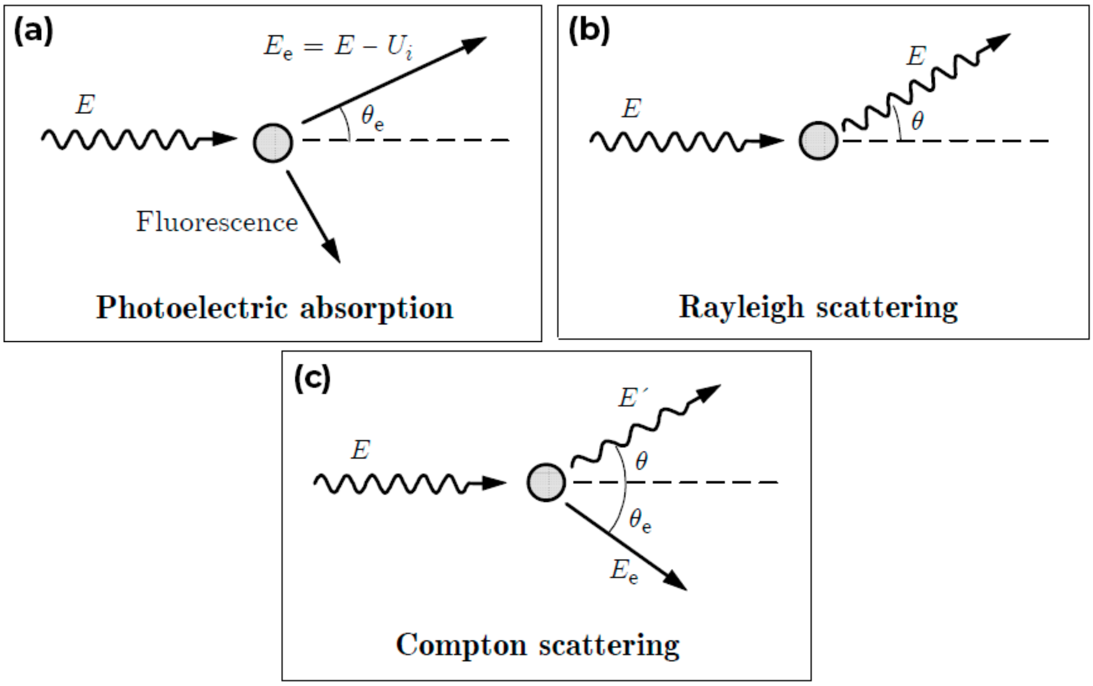

Figure 2.2: Illustration of the kinematics of a) Photoelectric absorption, b) Rayleigh and c) Compton scatterings. Source: PENELOPE v. 2014 manual [37].

which interaction will occur, the energy loss and angular deflection of photons, besides the initial state of secondary particles, if one is produced. If the photon energy after the interaction is below a threshold specified by the user ($EABS$), then the photon is considered as absorbed, on the other hand, if its energy is above the $EABS$ then simulation continues. This also happens for the secondary particles.

2.1.2 Simulation of electrons

Charged particles have a hundred percent probability of interacting in the medium, since the Coulomb force has a long-range, and there are several electrons distributed in the medium [46]. The possible electron interactions with the medium are elastic scattering, inelastic collisions and Bremsstrahlung emission [46]. Elastic scattering results in a change of electron direction without loss of energy. In an inelastic collision, the initial electron loses energy (W) by ionizing the atom with a change of direction, where the secondary electron kinetic energy (E_s) is equal to W - U_i. Similarly with the photoelectric effect, after the inelastic collisions fluorescence or Auger electrons are emitted to fill the vacancies. Bremsstrahlung emission occurs when a charged particle interacts with the atom's nuclei and the energy lost in this interaction is converted into a photon. Similarly, with photons, the probability of each interaction occurring is obtained from the DCSs, as well as energy lost and scattering angles. Figure 2.3 shows illustrations for each type of charged particle interaction.

Because of the large number of electron interactions, modeling each interaction

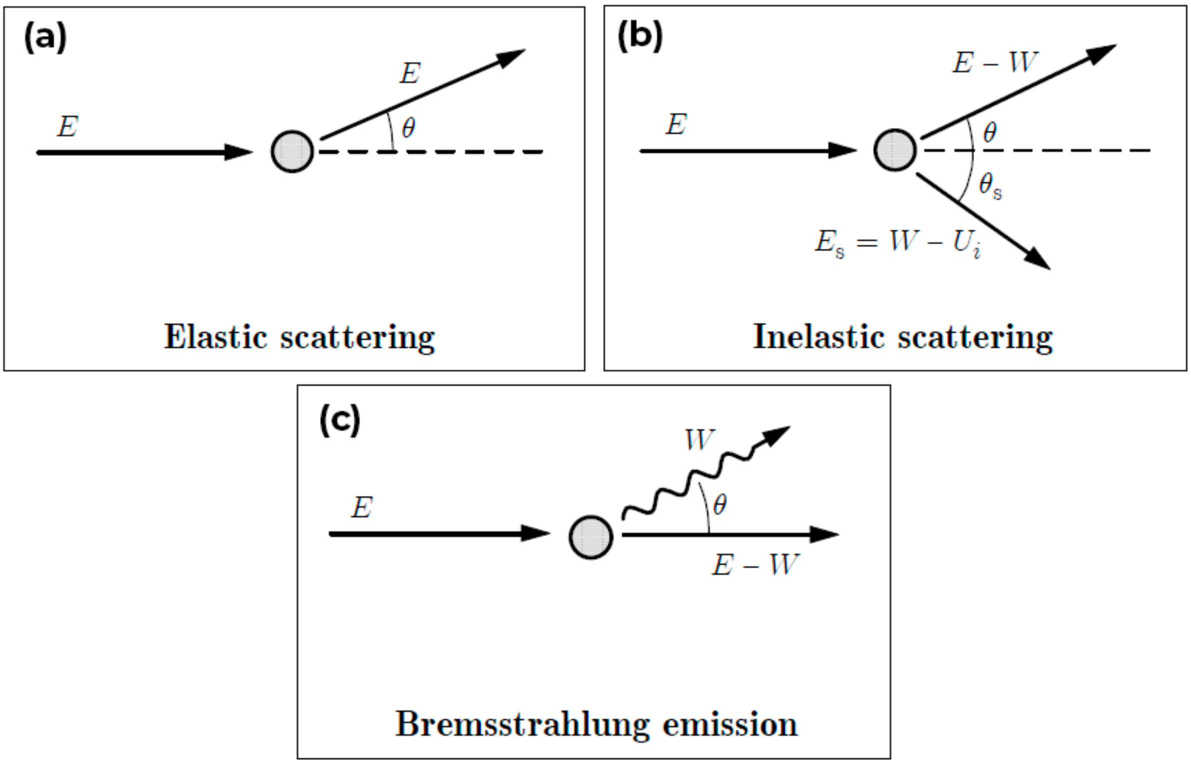

Figure 2.3: Illustration of the kinematics of electrons a) elastic and b) inelastic scattering, c) Bremmstrahlung emission. Source: PENELOPE v. 2014 manual [37].

would result in lower simulation velocity. The PENELOPE code uses a mixed simulation procedure: soft collisions are modeled using multiple scattering theory and hard collisions are simulated individually [37]. The parameters that control if a collision is interpreted as soft or hard are: the average angular deflection (C_1) produced by multiple elastic scatterings in a path with length equal to the mean free path between consecutive hard elastic events, the maximum average fractional energy loss (C_2) between consecutive hard elastic events, the cut-off energy for inelastic hard collisions (WCC) and Bremsstrahlung (WCR). If $C_1 = C_2 = 0$, then each electron is simulated individually, this case is the most detailed simulation possible.

2.2 Detectors in digital radiography

The detector is one of the defining features of a digital radiography system. The detector converts the spatial pattern of the X-ray transmitted by the body into an electronic signal [24]. For all the detector technologies there are a sequential of operations that include:

- Interaction with the X-rays transmitted by the body and absorption of their energy.
- Conversion to a usable signal - generally electronic charge.
- Signal collection.

- Readout, amplification, and digitization.

The conversion of X-ray to a usable signal can be either direct or indirect depending on the different detector technologies. Moreover, the mode of detection can be energy integrating, i.e., the signal is proportional to the energy deposited, or photon counting, where each photon that was counted has the same weight [27]. The detector types available in digital radiography are computed radiography (*CR*) detectors, indirect and direct digital radiography (*DR*) detectors and photon counting detectors (*PCD*).

2.2.1 Computed radiography

CR technology is based on the use of photostimulable phosphors systems. When photostimulable phosphors absorb X-rays, a fraction of the absorbed energy is trapped and can be read out later using a laser light [2]. Figure 2.4 shows the operating principle of a photostimulable phosphor system.

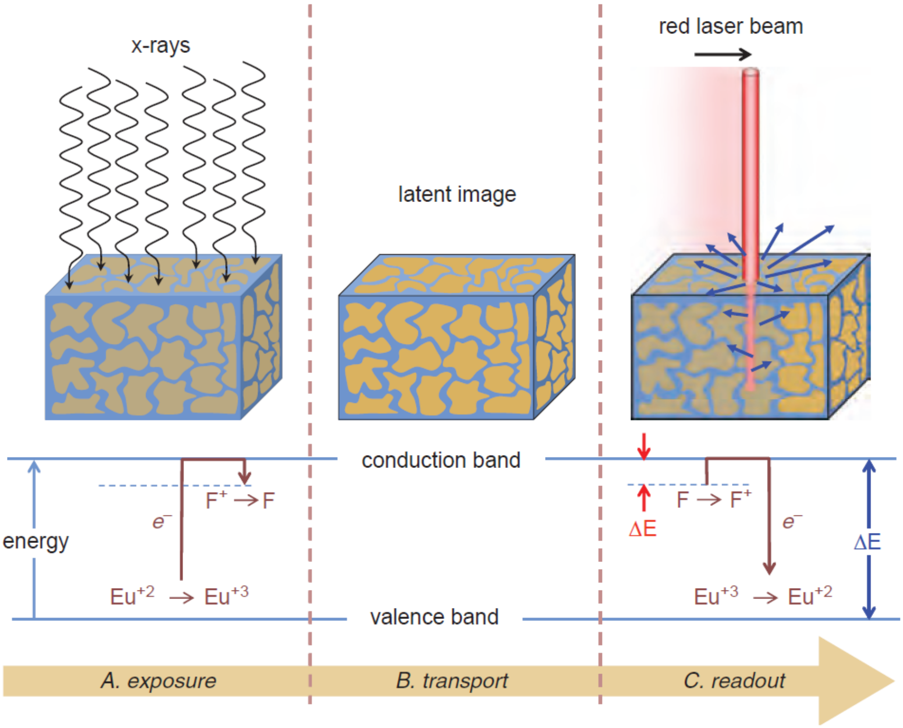

Figure 2.4: Operating principle a photostimulable phosphor system showing the (A) X-ray exposure, (B) latent image and (C) the readout process. Source: Bushgerg et al [2].

CR imaging plates usually are composed of approximately 85% BaFBr and 15% BaFI, and doped with europium. This doping procedure creates defects in the solid, giving rise to F-centers, allowing electrons to be trapped more efficiently [28]. The absorbed energy from the incident X-rays in the detector excites electrons associated with the europium atoms and a fraction of them interact with F-centers, trapping them in a higher energy. The trapped electrons can remain in this metastable state for minutes to weeks, with only slight fading over time. The number of trapped excited electrons is proportional to the number and energy of the incident X-rays at each detector position. A red laser light scans the exposed imaging plate, and a fraction of the trapped electrons gain enough energy to reach the conduction band, become mobile, and then drop to the ground energy state, emitting blue light that is channeled to a photomultiplier tube. After the readout, the image plate is exposed to a very bright light source to empty the F-centers that still had trapped electrons, therefore erasing the latent image [2].

2.2.2 Indirect digital radiography

Indirect *DR* detectors combine a layer of scintillator material (phosphor) with amorphous silicon (a-Si) active matrix readout array [25]. Phosphors are crystalline materials to which impurities have been added to create energy levels within the forbidden bandgap [24]. After the interaction with X-rays, electrons excited into the conduction band have a chance of being captured by these impurity centers and de-excited in nanoseconds. On their way down to their ground state (valence band) the electrons pass through the energy levels in the forbidden bandgap. As the electrons transition between the energy levels, photons are emitted. The energy of these photons is equal to the difference in energy levels and this determines the light wavelength. A notable feature is that the conversion gain for the conventional phosphors used in indirect *DR* is an order of magnitude greater than the photostimulable phosphors used in *CR* detectors (Section 2.2.1) [28]. The CR lower conversion gain is mainly due to losses in the readout process [2]. A schematic of a typical indirect conversion *DR* image detector is shown in Figure 2.5.

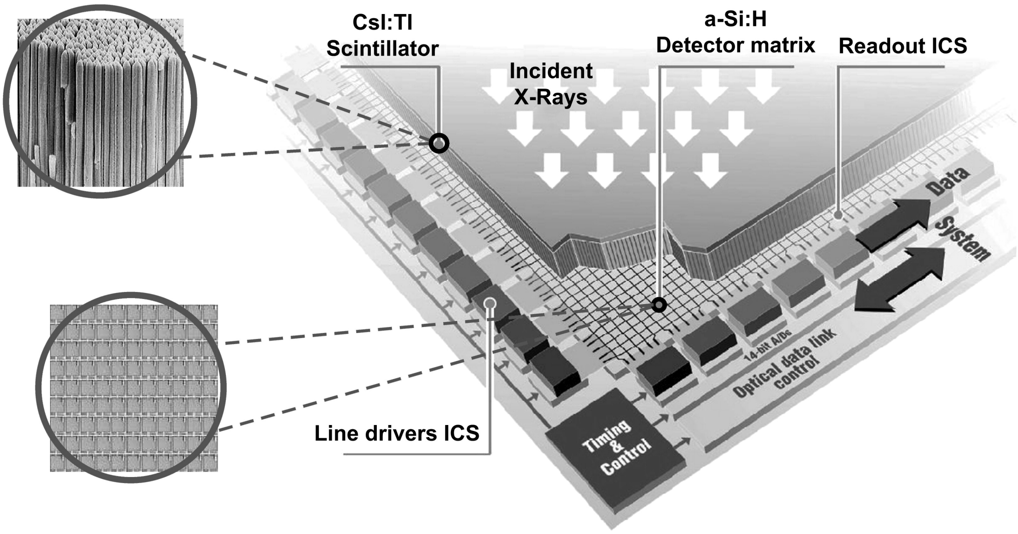

Figure 2.5: Illustration of an indirect *DR* detector cross-section showing the CsI scintillator, the photoconductor detector matrix and the readout integrated circuit. Source: Cowen et al. [25].

Most of the *DR* detectors use a layer of thallium-activated cesium iodine (CsI:Tl) [2, 25, 48] to absorb the X-rays and convert them to visible light [25]. Because of its high effective atomic number (Z = 55 and 53, respectively), CsI is a great X-ray absorber [25]. Moreover, CsI is grown in columnar crystals (seen in Figure 2.5 at the upper left corner), and the columns act as light pipes to reduce the lateral spread of light, and therefore, increasing the spatial resolution [2]. For standard projection radiography, the typically used CsI layer thickness is between 500-600 μm [25, 49, 50].

The active matrix array consists of millions of individual pixel electrodes connected by thin film transistors (TFT), one for each pixel acting as switches [51]. The pixels are light-sensitive elements (photoconductors), and the fluorescent light emitted during the X-ray exposure illuminates the photoconductors freeing charge carriers (electrons and positively charged holes) [25]. During X-ray exposure, all switches are non-conducting, to charge accumulates in storage capacitors (C_{ij}), which are positioned at the junctions of the photoconductors [25]. The quantity of charge accumulated at each pixel is proportional to the fluence of photons absorbed at that position [25]. The active matrix array has M × N capacitors C_{ij}, whose charge can be read through addressing the TFT via the gate control line (i) and data transfer line (j) [25, 51]. The output signal is then amplified prior to digitization and transferred to the system computer [25].

2.2.3 Direct digital radiography

In a direct-conversion *DR* system, X-rays are converted into charge without both the need for a readout process and fluorescent layer [25]. This is achieved by a layer of X-ray photoconductor material. These photoconductor materials when exposed to X-rays induce free-electrical charge carriers, an *EHP* [24, 51]. After their formation, the *EHP*s start a random thermal motion that results in their diffusion away from their point of origin [52]. An electric field is applied to the photoconductor material and due to its influence, the *EHP* will have a drift velocity parallel to the applied field direction [52]. The motion will be the combination of a random thermal velocity and the drift velocity. Figure 2.6 shows an illustration of the detection process in a direct *DR* detector. A few key factors in a photoconductor are the spatial resolution, X-ray sensitivity, quantum efficiency and dark current.

Spatial Resolution

Photoconductors that directly convert X-rays into *EHP*s have several distinct advantages, one of which is their intrinsic high resolution because of the applied electric field [51, 52]. However, some factors limit the resolution of these detectors such as the range of electrons generated by the photoelectric effect, the K-fluorescence, Compton scattered photons and Coulombic repulsion between the drifting charges [51, 53].

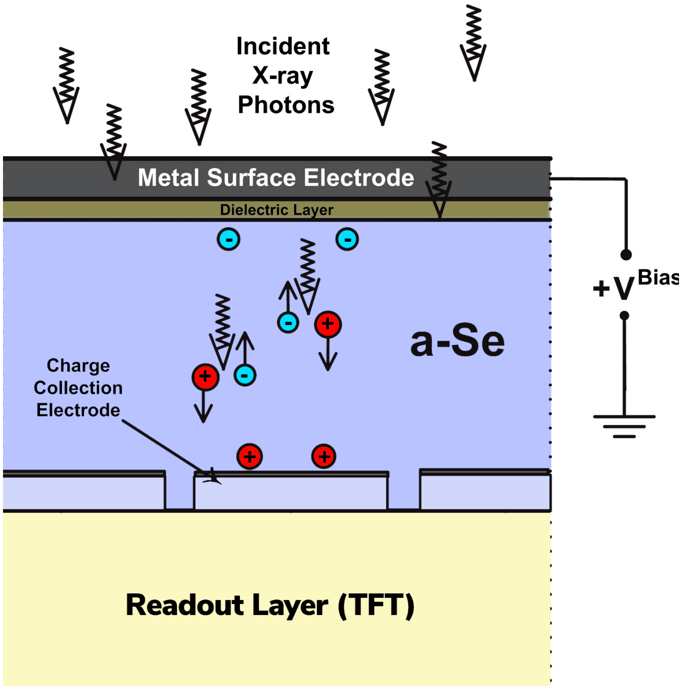

Figure 2.6: Illustration of a direct *DR* detector, showing the creation of electron-hole pairs, their drift caused by the electric field, and the charge collection.

X-ray sensitivity

The X-ray sensitivity is related to the number of *EHP*s created by each interacting X-ray. The charge generated (Q_{total}) from absorbing a photon of energy E is given by:

$$Q_{total} = \frac{E}{W_{\pm}}, \tag{2.3}$$

where $W_{\pm}$ is the amount of energy necessary to create an *EHP*. Therefore, increasing the X-ray sensitivity means decreasing the $W_{\pm}$ value. For most photoconductors the $W_{\pm}$ is only dependent on the energy bandgap (E_g) [51]. However there is a special case, the $W_{\pm}$ for a-Se is strongly dependent on the applied electric field due to the recombination between electrons and holes [51, 54, 55]. Usually the electric field used in a-Se detectors is 10 V/μm where the $W_{\pm}$ value is around 50 eV [51, 54, 56], but for higher electric fields, such as 70 V/μm this value decreases to 12 eV [57].

Quantum efficiency

For a detector with thickness equal to L, the X-ray quantum efficiency (η) is given by:

$$\eta = 1 - exp[-\mu(E, Z) \times L], \tag{2.4}$$

where μ is the photoconductor linear attenuation coefficient, which depends on its atomic number (Z) and the X-ray energy (E).

Photoconductors must have a high η, which can be achieved by either increasing L or using photoconductors with high Z. However, those are drawbacks, the probability that free charges will be trapped increases with L. On the other hand, the K-fluorescence photons' energy will increase with Z, which will decrease the spatial resolution. Figure 2.7 shows the thickness where the beam has been attenuated by 63% ($\delta = 1/\mu$), as a function of the energy for a few photoconductors.

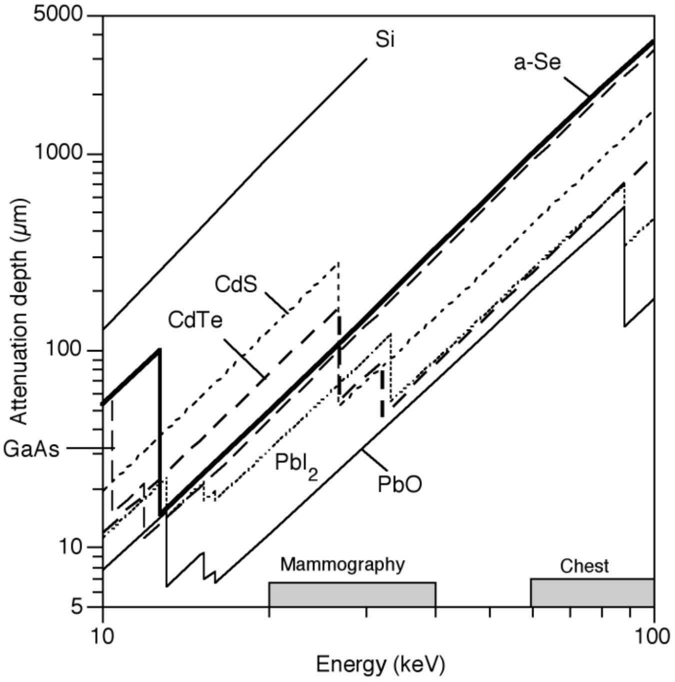

Figure 2.7: Thickness where the beam has been attenuated by 63% ($\delta = 1/\mu$) versus photon energy (keV). Source: Kasap et al. [51].

The detector should be at least thicker than δ. For instance, for an a-Se detector, δ is equal to 48 e 976 μm for 20 and 60 keV photons, typical energies for mammography and chest radiology, respectively. Therefore, if $L = 2\delta$, the detector thickness should be approximately 100 and 2000 μm, respectively. In mammography, typical a-Se detector thickness is 200 μm [58, 59], which is thicker than δ. However, detectors used in chest radiography are around 500 μm [25] (one-quarter of the δ), chosen to avoid high charge trapping and low spatial resolution [25].

Dark current

Dark current consists of the charges generated in the detector when no outside radiation is entering. In X-ray detectors, dark current can be created due to the depletion of carriers from the defect states within the bandgap, carrier injections from the metal contacts with the photoconductor and thermal generation of charges [29]. Because the dark current is a source of noise, it should be as small as possible. Small dark conductivity generally requires a wide bandgap semiconductor, but that conflicts with the high sensitivity condition [51]. The dark current should preferably not exceed 10 pA mm^2, depending on the clinical application [60].

Typical photoconductors

Photoconductors used in medical imaging must have several attributes, including low $W_\pm$, high η, and low dark current, and these are difficult to achieve in a single material [56, 61]. Detectors based on amorphous selenium (a-Se) are successful and the most used [25, 56]. However, mercuric iodine (HgI_2), lead iodine (PbI_2), lead oxide (PbO), and cadmium zinc telluride (CdZnTe) are present in the literature [29, 60, 61]. Table 2.1 shows the comparison of the physical properties of the photoconductors most used in the literature [29, 61, 62]: δ at 20 and 60 keV, E_g, $W_\pm$, the electron (μ_e) and hole (μ_h) mobilities, and the product of their mobility and lifetime ($\mu_e\tau_e$, $\mu_h\tau_h$), the dark current, the normal operating field, and the reported maximum detector size.

Table 2.1: Comparison of the physical properties of the most common photoconductors [29, 60, 62, 63]

Property	a-Se	HgI_2	PbI_2	PbO	CdZnTe
Density (g/cm^3)	4.3	6.3	6.2	4.8	5.8
δ (μm) at 20 keV	48	32	28	11.8	60
δ (μm) at 60 keV	976	252	259	218	280
Bang gap (E_g)	2.2	2.1	2.3	1.9	1.7
$W_\pm(eV)$	50 at 10 V/μm	≈ 5	≈ 5.5	8 - 20	≈ 5
μ_e (cm^2/Vs)	0.003 - 0.006	88 - 100	8	-	1000
$\mu_e\tau_e$ (cm^2/V)	0.3 - 3×10^{-6}	$10^{-5} - 10^{-4}$	7×10^{-8}	$\approx 3.5 \times 10^{-7}$	$\approx 2 \times 10^{-4}$
μ_h (cm^2/Vs)	0.12	3 - 4	0.02 - 0.15	-	120
$\mu_h\tau_h$ (s)	0.6 - 6×10^{-6}	$\approx 10^{-7}$	$\approx 2 \times 10^{-6}$	$\approx 10^{-8}$	$\approx 3 \times 10^{-6}$
Dark current (pA/mm^2)	1	6	10 - 50	40	25
Normal operating field (V/μm)	10	0.5	0.5	1	0.25
Reported Max. Size (cm^2)	43×43	20×25	20×25	18×20 cm^2	7.7×7.7

Due to its low atomic number ($Z = 34$), selenium has the lowest values for δ (i.e., the lowest X-ray absorption). Moreover, the $W_\pm$ is the largest for selenium, followed by the PbO, and is highly dependent on the electric field [51]. At very high electric fields (above 70 V/μm) holes generated in a-Se detector can gain enough energy to create additional *EHPs* through impact ionization, resulting in an avalanche gain up to 1000 [29, 57]. There are studies for avalanche gain implementation in medical imaging, however, an increase in dark current and high spatial frequency noise are drawbacks [57]. The μ_e for a-Se is orders of magnitude smaller than the other common semiconductor materials, making it one of the most undesirable properties of a-Se. On the other hand, a-Se has a very low dark current, 1 pA/cm^2 [51], and can be coated onto a large area with great uniformity [29].

HgI_2 is the closest competitor to a-Se for both mammography and general radiology due to its good spatial resolution, acceptable dark current and homogeneity [60]. However, the long-term stability of HgI_2 has not been as thoroughly studied as stabilized a-Se detectors. HgI_2, PbI_2 and CdZnTe have a high X-ray absorption and high X-ray sensitivity, with $W_\pm$ around 5 eV [29, 60]. Therefore, they can absorb a large percentage of the incident photons with relatively thinner photoconductor thicknesses and create a large number of *EHP*, decreasing the noise. The dark current of CdZnTe, PbI_2 and PbO detectors are worse than those of HgI_2 detectors. However, the X-ray detectors made with CdZnTe are mechanically and chemically more stable than HgI_2 [29]. Another limitation of CdZnTe is the small detector size: 7.7 × 7.7 cm^2 [29].

2.2.4 Photon Counting Detectors

All detectors showed before are energy integrating, meaning, that the detected signal is proportional to the total energy deposited by all photons, losing information about the energy of each photon [27]. In energy-integrated detectors, higher energy photons deposit more energy in the detector. Therefore, they have a larger influence on the final image than low-energy photons. However, contrast between tissues decreases with the energy, meaning that ideally low energy photons should have more weight in the image [30]. Additionally, dark current and Swank noise are added to the signal [31].

*PCD*s process incoming X-ray photons individually, having the potential to overcome these issues. This individual processing is achieved by means of dedicated electronic circuits, based on the use of one or more detection thresholds. Additionally, an appropriate choice of detection thresholds for *PCD*s allows for full noise rejection, leading to a higher contrast-to-noise ratio [30]. The diagram shown in Figure 2.8 illustrates the operating principles of a *PCD*. Each detected photon results in a pulse, whose pulse height is proportional to the photon energy. By implementing different energy thresholds is possible to remove electronic noise and sort the registered photons into several energy bins.

Figure 2.9 shows the cross-section of a hybrid pixel detector, for example,

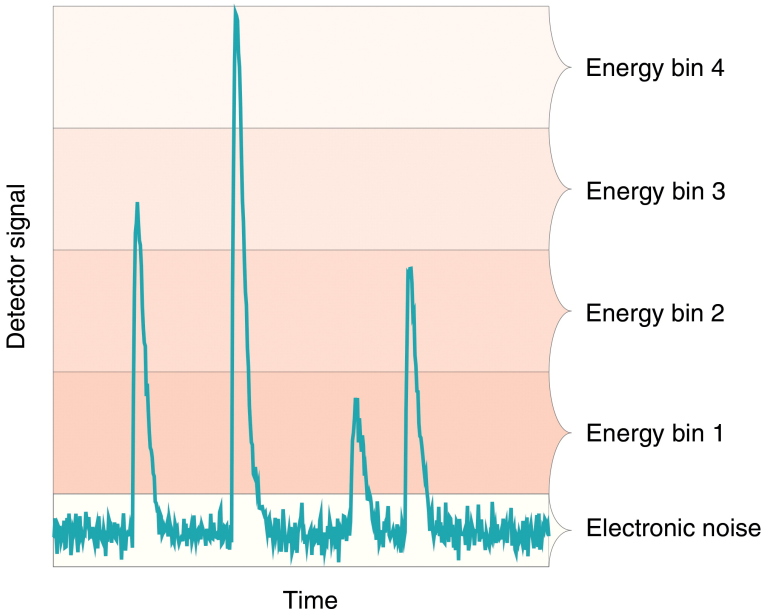

Figure 2.8: Diagram illustrating the operating principles of a photon-counting detector where different energy bins are employed to determine if a pulse produced by X-ray interactions is counted. Source: Willemink et. al [64].

the Medipix2. In *PCD*s, each sensitive element is connected to its individual readout electronic chain, provided by an application-specific integrated circuit (ASIC). The hybrid detector consists of two superimposed layers. The top layer is the detecting material or sensor, in which X-rays can interact and their interaction is detected. The bottom layer is the readout electronics and defines the segmentation and pixel pitch of the *PCD*. Sensor material and readout electronics are processed on two different substrates and are electrically connected via the bump-bonding and flip-chip techniques, realized by placing a drop (with a diameter in the order of 10–20 μm) of solder material (e.g., In, PbSn, Au) between two metal pads attached to sensor and ASIC. Each pixel of a hybrid pixel detector needs individual bump bonding. Each pixel cell of the readout ASIC features a complete signal processing cell, where the signal is proportional to the number of electron-hole pairs generated in the sensor volume, if this signal is larger than a threshold value the photon is counted.

Ideally, when a photon interacts with the sensor material in a specific pixel, the signal should be processed in the same pixel. However, the signal created from the photon's initial energy can be shared between two or more pixels due to the range of secondary particles, such as Compton scattered photons and fluorescence [31].

A major disadvantage in PCDs is pulse pile-up, which is when the second photon is detected in a pixel while the signal from the first photon is being processed, resulting in a single event being detected at higher energy and decreasing the number of counts [30, 31].

Most of the detecting materials used *PCD*s are semiconductors, therefore the

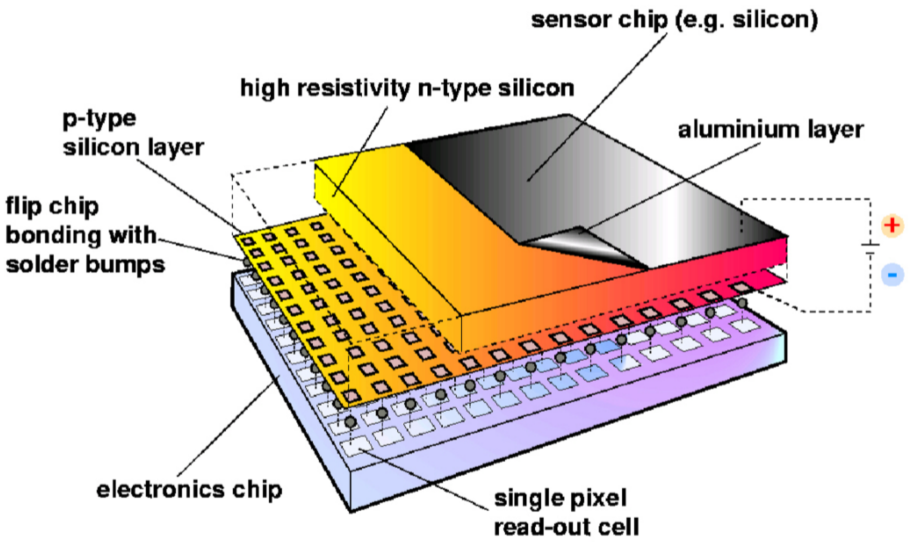

Figure 2.9: Cross-section of a hybrid pixel detector (Medipix2). A depleted semiconductor sensor is bump-bonded to a dedicated ASIC. The ASIC provides per-pixel circuits for signal discrimination and readout. Source: Russo et al. [31].

interaction of X-ray with the detector is the same as in the case of direct *DR* systems (Section 2.2.3). The sensors already used in the literature are silicon [65], gallium arsenide (GaAs) [66], cadmium telluride (CdTe) [65, 67] and high purity germanium (HPGe) [68]. For the X-ray energies used in radiography, silicon is not indicated due to its low atomic number (Z = 14). The high-Z sensors (CdTe, GaAs and HPGe) have a larger probability of photoelectric effect. Moreover, they have a lower cross-section for Compton Scattering than silicon [69]. However, the fluorescence photons are a major problem, since their energies are relatively high ($\sim$10 keV for Ga and As, $\sim$23 keV for Cd and $\sim$27 keV for Te) [70]. The relatively high energy of these characteristic X-rays results in the mean free paths: $\sim$40 μm for Ga, $\sim$50 μm for As, $\sim$110 μm for Cd, and $\sim$60 μm for Te [69], which are comparable to commonly used pixel pitches ($\sim$50 μm) [31, 65], resulting in a deterioration of spatial and energy resolution of *PCD*s.

2.3 Characterization of detectors

Detectors can be characterized in terms of their energy and spatial resolution, noise and efficiency. This section defines these properties and describes the metrics used to quantify them.

The energy resolution is the capacity of the detector to separate two energies [52], and is more relevant in spectroscopy detectors (e.g., the ones used in nuclear medicine [2]). However, in *PCD*s used in radiology, where is possible to create energy bins by establishing thresholds, the energy resolution is also a relevant parameter [30]. The Swank

Factor (I) is the energy resolution metric that will be described in this section.

The spatial resolution is a property that describes the ability of an imaging system to distinctly represent two objects as they approach and become smaller [2, 46]. The limit of spatial resolution is reached when the two objects overlap [2]. The spatial resolution is limited by focal size, beam divergence and detector used. *DR* detectors tend to have better spatial resolution than *CR* [49]. The Modulation Transfer Function (MTF) is the spatial resolution metric that will be described in this section.

Due to the radiation interaction with matter's stochastic nature, images generated by photons are of a statistical nature. The noise describes the detected signal fluctuation that degrades the image quality and, consequently, difficult the differentiation between structures [2]. There are several sources of noise, such as quantum, electronic and structural, with the quantum noise being one of the most relevant because it is affected by the incident beam intensity [71]. The Noise Power Spectra *NPS* is the noise metric that will be described in this section.

The efficiency quantifies the detector's ability to convert the input pulse into the final signal. The η was shown in Section 2.2.3, and in this section the Detective Quantum Efficiency (DQE) will be described.

2.3.1 Swank Factor

The Swank Factor (I) is a statistical factor that arises from fluctuations in X-ray detection and is a common energy resolution metric. For instance, for direct *DR*, is the fluctuations in the number of *EHP* detected per absorbed X-ray [72, 73]. A greater I implies in a better detector energy resolution [74]. In an X-ray imaging system, the interaction with the X-rays creates a pulse, which is usually integrated rather than counted [75], and the pulses in general are not of uniform size but are distributed according to some probability distribution [75, 76]. This distribution is called pulse-height spectrum (PHS) [51]. Three major factors contribute to the form of this distribution are:

- The incident X-ray energy distribution, i.e, spectrum;
- The absorbed energy distribution which results from variable absorption processes;
- The optical pulse distribution (for indirect *DR* detectors) and the distribution of *EHP* detected (for direct *DR* detectors).

The Swank Factor is calculated as:

$$I = \frac{M_1^2}{M_0 M_2}, \tag{2.5}$$

where M_0, M_1 and M_2 are the respective moments of the *PHS*, considering both the energy deposition and conversion of X-rays in *EHP* or an optical pulse [72, 76]. The moments can be calculated by:

$$M_j = \int_0^\infty E^j \times PHS(E)dE. \tag{2.6}$$

Figure 2.10 shows examples of *PHS*, the first case in Figure 2.10 shows an ideal *PHS*, all X-rays produce equal amounts of charge, resulting in a delta function, therefore $I = 1$. The second case shows a single peak broadened by statistical processes associated with the physics of detection, therefore, I decreases to approximately 0.95. The third case shows an extra peak caused by K-fluorescence escape, resulting in a lower I, around 0.75.

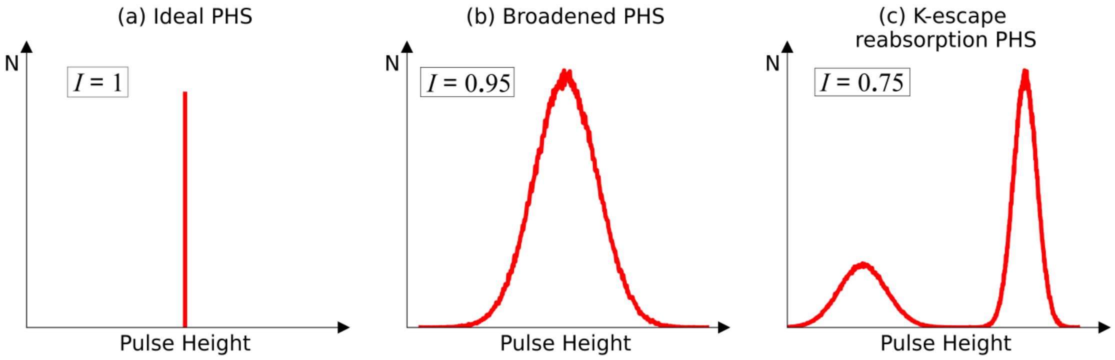

Figure 2.10: Example of *PHS* that may be observed and the corresponding Swank Factor value. Source: adapted from Kasap et al. [51].

2.3.2 Modulation Transfer Function

If a signal with a sinusoidal waveform with a spatial frequency of f is detected, usually the detected signal has the same f value but its amplitude of the signal tends to be lower as f increases. This reduction is a result of resolution losses in the imaging system. Figure 2.11 shows examples of input sinusoidal signals with frequencies of 1, 2, and 4 cycles/mm (on the left side), and the detected amplitude was 87%, 56%, and 13%, respectively. Decomposing the recorded signals on Figure 2.11 into its constituent frequencies (i. e. applying the Fourier Transform) results in peaks located at the corresponding frequencies. A real input signal contains numerous sinusoidal waves, therefore, the Fourier transform would then result in the smooth *MTF* curve shown in Figure 2.12 where the three frequencies in Figure 2.11 are indicated with an arrow.

The *MTF* is used to describe the spatial resolution of a detector. The frequency in which the *MTF* is 10% is often considered the limiting spatial resolution, i.e., the size of the smallest structure detectable.

The *MTF* is usually calculated by measuring the line spread function (*LSF*), which is the response of the detector from a signal in the form of a line. A perfect

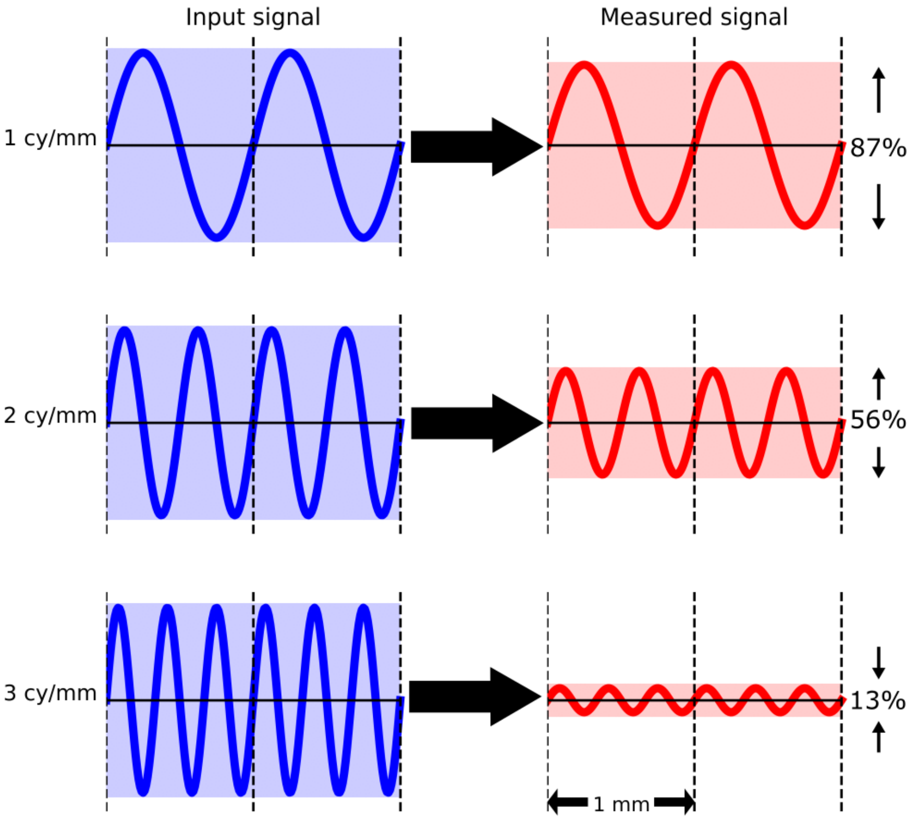

Figure 2.11: Sinusoidal input signals incident on the detector and its attenuation after measured by the imaging system. Source: adapted from Bushberg [2].

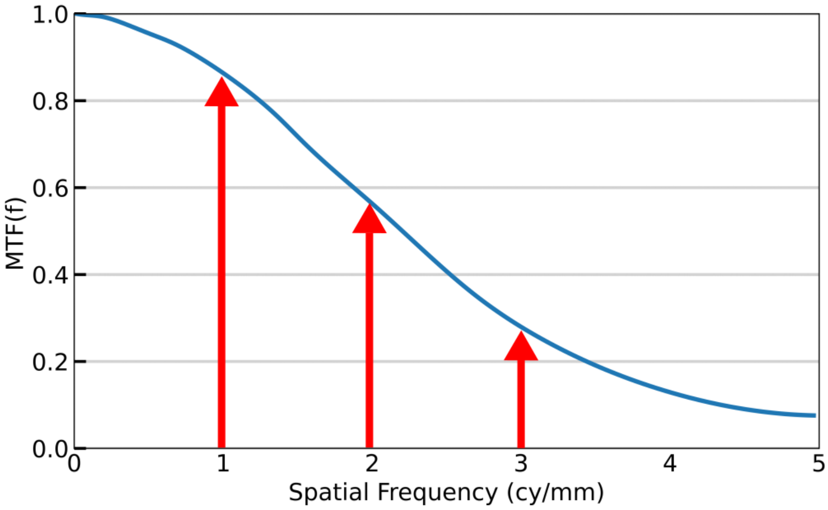

Figure 2.12: *MTF* curve obtained from the Fourier transformation of the input signal. Source: adapted from Bushberg et al [2].

line source in the frequency domain represents an infinite number of sinusoidal functions. Therefore, the *LSF*'s Fourier transform computes the full MTF curve as shown by:

$$MTF(f) = \left| \int_{-\infty}^{\infty} LSF(x) e^{-2\pi i f x} dx \right|, \tag{2.7}$$

The *MFT(f)* can also be obtained by measuring the point spread function (*PSF*) and edge spread function (*ESF*), which are the detector response from a point signal and a sharp edge, respectively. The *LSF* is obtained by the convolution of the *PSF* with a line, also the *LSF* is the derivative of the *ESF* as:

$$LSF(x) = \int_{y=-\infty}^{\infty} PSF(x,y)dy, \tag{2.8}$$

$$LSF(x) = \frac{d}{dx} ESF(x). \tag{2.9}$$

Figure 2.13 shows visually the difference between the *PSF*, *LSF* and *ESF* [2]. With the *LSF* obtained by either a direct measurement or by the *PSF* or *ESF* the *MTF(f)* is calculated using the equation 2.7. Experimentally is more practical to measure the *ESF*.

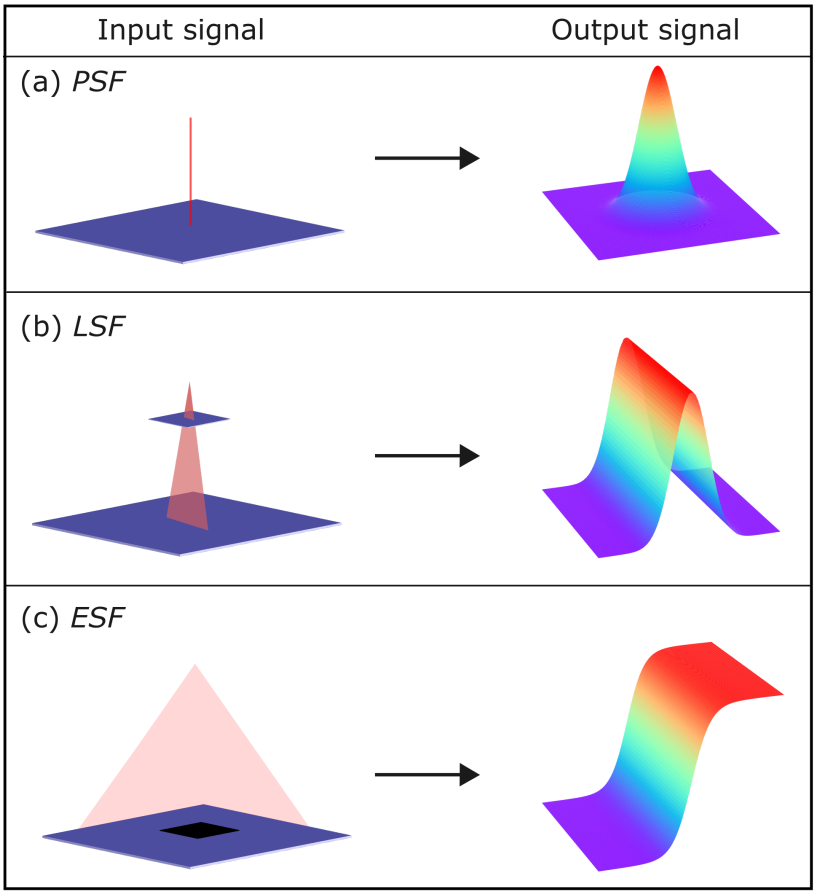

Figure 2.13: (a) Input point signal forming the *PSF* as the output, (b) a slit signal forming the *LSF* and (c) a full field reaching a high absorbent material, such as tungsten, creating a sharp edge and resulting in the *ESF* as the output signal. Source: adapted from Bushberg et al. [2].

2.3.3 Noise Power Spectra

The standard deviation (σ) is a quantity normally used to evaluate the noise present in the image, being used for estimating quantities such as *CNR* and *SNR*. However, σ does not carry the noise pattern information, since it only presents an average of the fluctuations between pixels in a region of interest [2]. For instance, Figure 2.14 shows two images with the same standard deviation but the noise textures are different, with the left containing high-frequency noise and the right image low-frequency noise.

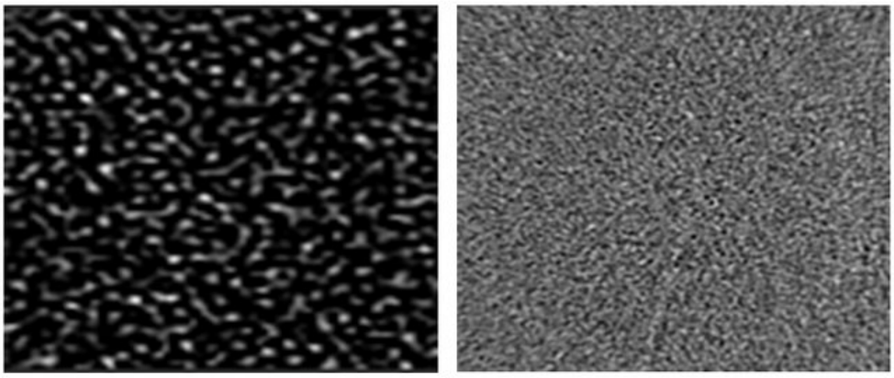

Figure 2.14: Example of images with the same standard deviation but different noise textures. Source: Khodajou-Chokami et al. [77].

The *NPS* is used to characterize the noise texture by describing the noise of an image as a function of the spatial frequency [2]. For a two-dimensional image, the *NPS* is calculated as:

$$NPS(f_x, f_y) = \left| \int_y \int_x [PV(x,y) - \overline{PV}] e^{-2\pi i (x f_x + y f_y)} dx dy \right|^2, \tag{2.10}$$

where f_x e f_y are the spatial frequencies in the x and y directions. $PV(x,y)$ is the image signal in a pixel located at the (x,y) position, and $\overline{PV}$ is the average signal in a region of interest. The PV in radiography represents the gray level.

The variance (σ^2) is calculated integrating the *NPS* over all frequencies:

$$\sigma^2 = \int_{f_y} \int_{f_x} NPS(f_x, f_y) df_x df_y. \tag{2.11}$$

The normalized *NPS* (*NNPS*) is calculated as [78]:

$$NNPS = \frac{NPS}{\overline{PV}^2}. \tag{2.12}$$

2.3.4 Detective Quantum Efficiency

The *DQE* is historically the most used quantity to evaluate the performance of the X-ray detector. It describes the efficiency in converting the *SNR* related to the incident beam reaching the detector (SNR_{in}) into the final (SNR_{out}). The *DQE* is determined as:

$$DQE = \frac{SNR_{out}^2}{SNR_{in}^2}, \tag{2.13}$$

Considering that *MTF(f)* describes the signal processed by the imaging system and *NPS(f)* describes how the system processes noise, the signal-to-noise ratio SNR_{out} can be defined as [2]:

$$SNR_{out}^2 = \frac{|MTF(f)|^2}{NPS(f)}, \tag{2.14}$$

Air kerma (K_{ar}) is proportional to the number of incident photons and the squared SNR_{in} can be defined as the K_{ar} multiplied by a conversion factor, q, which is the photon intensity per unit area per unit of K_{ar} [2]:

$$SNR_{in}^2 = K_{air} \times q \tag{2.15}$$

Combining the equations (2.13), (2.14) and (2.15) it is possible to calculate the *DQE* as.

$$DQE(f) = \frac{|MTF(f)|^2}{NPS(f) \times K_{ar} \times q} \tag{2.16}$$

The *DQE* depends on the spatial frequency, *f*. When f is equal to zero, *DQE* represents the ratio between the detected and incident energy in the image detector, called the quantum detector efficiency (QDE).

The *DQE* characterizes the efficiency of the incident beam in a detector of an X-ray system, and can thus be used as an optimization figure of merit.

Chapter 3

Literature Review

This thesis focuses on the impact of *EHP* simulation in semiconductor detectors on image acquisition and optimization in thorax radiography. Therefore, this chapter presents a brief description of the most relevant studies and results regarding the *MC* simulation of digital radiology detectors. In addition, a brief description of the most relevant studies in the literature on optimization in radiography is also presented.

3.1 Detailed simulation of radiography detectors

Detailed simulation of imaging detectors has been a topic of notice interest for several types of digital detectors, such as those for computed radiography (*CR*) [79, 80] and indirect digital radiography (*DR*) [81, 82] detectors. However, the focus of this review is on direct *DR* and photon counting detectors (*PCD*).

Direct *DR* and *PCD* detectors use photoconductors to convert the X-rays directly into electrical signal [2, 30, 51]. Direct *DR* detectors are energy integrating, meaning that the signal is proportional to the energy deposited in the detector by all photons without specific information about an individual photon or its energy [27]. *PCD*s counts individual photons by defining thresholds, and if an electric pulse produced by a photon has a height lower than the threshold then the photon is not counted [30].

As stated, the sensor material for direct *DR* and *PCD*s is a photoconductor, which is composed of semiconductor materials [25, 51]. The studies that simulate the detailed process of detection using semiconductors are usually divided into: the interaction of X-rays and/or electrons with the sensor and creation and transport of *EHP*. The following sections summarize the studies in the literature that simulate each step.

3.1.1 Interaction of X-rays with the sensor

Most studies use already established *MC* codes to simulate the interaction of photons and electrons with the sensor material. The MCGPU v. 1.5 (*MC* on Graphics

Processing Units) code [40, 83] uses the interaction physics and material-specific interaction cross sections from the PENELOPE v. 2006 *MC* code [84] to create a new code using Graphics Processing Units (GPU) to accelerate the simulations. The ARTEMIS (pArticle transport, Recombination, and Trapping in sEM-conductor Imaging Simulations) code [72] and Sundberg *et al.* [85] used the PENELOPE v. 2006 [84]. A study by Magalhães and Tomal [86] used the PENELOPE v. 2014 [37] and modified a tally on the penEasy 2015 code [42] to include the creation and transport of *EHP*. Nilsson *et al.* [87] and Alsager and Spyrou [88] used the MCNPX (*MC* N-Particle) [89] code. Korn *et al.* [90] and Hoheisel *et al.* [91] used the program ROSI (ROentgenSImulations) [92]. The Allpix Squared code [93] and Day and Tanquay [94] used the GEANT4 *MC* code [95]. Stierstorfer [96] used the *MC* code MOCASSIM (Siemens Healthcare GmbH, Forchheim, Germany).

All the MC codes cited (PENELOPE code [84], the MCNPX (*MC* N-Particle) code [89], the program ROSI [92], the GEANT4 toolkit [95] and the *MC* code MOCASSIM simulate the interaction of photons and electrons. However, the MCGPU and studies by Magalhães and Tomal [86] and Korn *et al.* [90] did not include the electron transport, by considering that the secondary electrons created from photons interactions were locally absorbed after the ionization of atoms.

3.1.2 Creation of electron-hole pairs

Photons and fast electrons create *EHP* as they travel and interact with the matter [52]. In the previously published studies [40, 72, 83, 85–88, 93], the main approach to determine the number of *EHP* created per interaction is using the ratio $E_{dep}/W_{\pm}$, considering E_{dep} as the energy deposited by a particle interaction and the $W_{\pm}$ as the energy necessary to create an *EHP*.

The method used to determine the number of pairs created differs in each study. Alsager and Spyrou [88] and Sundberg et al. [85], computed the ratio $E_{dep}/W_{\pm}$ as the exact number of pairs created. In other studies, the number of *EHP*s was sampled using either a Gaussian [40, 83, 93] or a Poisson [86] distribution, where the mean is the ratio $E_{dep}/W_{\pm}$ and the standard deviation was a metric for energy resolution such as the Swank Factor [40, 83] and the Fano Factor [86].

The $W_{\pm}$ values used in these studies were obtained experimentally [40, 83, 85, 86, 88], this value already takes into consideration the recombination of electrons and holes. However, for the ARTEMIS code [72], $W_{\pm}$ was calculated using a semiempirical formula developed by Que and Rowlands [53] that takes into consideration the sensor's energy bandgap (E_g) and phonon energy. The recombination of pairs is included in the ARTEMIS code. The use of this semiempirical formula results in $W_{\pm}$ values considerably lower than other studies, for instance, the $W_{\pm}$ for amorphous selenium is 50 eV in the MCGPU v. 1.5 [40, 83] and for the ARTEMIS code is around 5 eV [72].

3.1.3 Transport of electron-hole pairs

When *EHP* is created, both the electron and the hole take part in a random thermal motion that results in their diffusion away from their point of origin [52]. Moreover, in semiconductor detectors, an electric field is applied to collect the charges, therefore there is a drift velocity in the electric field direction [2]. This section summarizes how the studies in the literature simulate the transport of *EHP*.

The study by Hoheisel et al. [91] was focused on simulating the *MTF* and used a correction factor to include the *EHP* transport effect, this factor depended on the detector thickness and electric field [91]. Therefore, there was no transport of *EHP* included in the simulations. The MCGPU does not include the transport of *EHP*, all the pairs were considered as detected in the same pixel that they were created.

There are studies focused on approximating the diffusion effect and Coulomb repulsion that is responsible as they traverse the detector without simulating the tracks of each pair. Random sampling with a Gaussian distribution is the most used method to simulate the transport of *EHP* [85, 86, 88, 90, 94, 96]. The main differences are how the standard deviation was obtained. For Magalhães and Tomal [86], Korn et al. [90], and Alsager and Spyrou [88] the Gaussian distribution was used to determine the final position of each *EHP*. In these cases, the standard deviation took into consideration the drift due to the electric field applied and the random thermal diffusion. The studies from Day and Tanquay [94] and Stierstorfer [96] took a different approach, for each energy-deposition event, the energy was distributed among detector elements assuming a Gaussian charge cloud, where the charge cloud width was the standard deviation for the distribution. In both cases, the charge cloud width was fitted from the measured data. Instead of sampling the *EHP* final position, Sundberg et al. [85] used a Gaussian distribution to sample the *EHP* drift velocity due to the thermal motion, and assumed that the drift velocity from the external electric field to be constant. The induced current on each electrode was calculated using these two velocities and the external electric field.

The ARTEMIS code [72] uses a more detailed modeling of *EHP*s transport, the code tracks each pair considering charge trapping, the drift due to external field, the Coulombic interactions between the charge carriers in the neighborhood, and the diffusion due to Brownian motion. This is achieved by updating the carrier position after discrete time steps, that are fixed by the user. The carrier's new position depends on the electric field, both external and from the other charge carriers. Also, at each simulation step, recombination and trapping are checked, by a sampling of random numbers using their probability function.

Another study that presents a more detailed simulation of transport is Nilsson et al. [87]. This study was performed using the General *MC* Semiconductor (GEMS) simulator [97]. GEMS is a full-band ensemble MC simulator, i.e., it is based on a numeric representation of the band structure where a lookup table was constructed, containing the radial distributions for different phonon energies and depth of the absorption event, phonon scattering mechanisms were also considered.

The Allpix Squared code has a differential among the other cases, a precise three-dimensional electric field description was included, whereas other studies considered the applied electric field as linear. The COMSOL Multiphysics software was used in Allpix Squared code to formulate and solve the differential form of Maxwell's equations together with a set of initial and boundary conditions and post-process the results to evaluate non-linear electric field components within the simulated device.

Several studies [40, 83, 85, 88, 94, 96] included the electronic noise by adding in each element a random amount of energy sampled from a zero-mean Gaussian distribution with standard deviation varying between studies.

In studies that simulate *PCD*s, there is an extra step: counting the photons considering thresholds. The studies by Sundberg et al. [85], Nilsson et al. [87], Korn et al. [90], Day and Tanquay [94] and Stierstorfer [96] simulate photon counting by comparing the energy in the pixel to different energy thresholds. Day and Tanquay [94] added an extra step, they used charge summation logic for charge-sharing suppression. In this case, when a pulse is registered simultaneously in two or more neighboring pixels, the pulses are assumed to have originated from the same X-ray interaction, and a count is attributed to the pixel with the greatest pulse, therefore, increasing the detector's spatial resolution.

3.1.4 Limitations of the studies

For the MCGPU [40, 83] and studies by Magalhães and Tomal [86] and Sundberg et al. [85], there is a limitation for high energies, where the simulations are less precise. The MCGPU code [40, 83] does not include the simulation of electrons, which are modeled on PENELOPE v. [84], the drift of charge carriers due to the electric field, and trapping. Since this code is focused on mammography studies, where X-ray energies vary between 10 and 30 keV [2], these limitations are less relevant than for the energies more commonly used in chest radiography (between 40 and 150 keV [2]). Because the MCGPU uses GPUs, it has the highest simulation velocity among the available codes ($\sim 10^8$ histories per second). In the study by Magalhães and Tomal [86], only the energy deposited by photoelectric interactions was considered for *EHP* creation and transport to increase simulation speed. Since the photon energy range used in the study was below 10 keV, where the photoelectric effect has a probability of 98% for silicon,[69], this choice of simplification is acceptable, but for higher energies more detailed in the simulation is needed. For Sundberg et al. [85], the increase of the electron track length with energies becomes a problem when the initial charge cloud sizes are on the same order of magnitude as the pixel size.

The ARTEMIS code presents the most detailed model for the creation and transport of *EHP* in this review, including features such as the recombination and trapping that are not present in other studies in this review. However, due to its high level of detail, the ARTEMIS's simulation velocity is the lowest among the codes present, around 10^{-1} histories per second. Similarly, the study from Nilsson et al. [87], due to the detail in simulating the phonon transport, presents a low simulation velocity where the time needed to simulate the charge collection was approximately 24 hours per absorption event.

Some studies [87, 90, 91, 94, 96] divided the simulation into two codes, first simulating photons and electrons using established MC codes and then extracting tables with information about these simulations and modeling *EHP* separately. While other studies [40, 72, 83, 86, 88] coupled the simulation of X-rays and *EHP* into one code. Dividing the simulations into two different codes presents a few limitations, the tables extracted from the simulations are large since it contains information for each interaction. Therefore, creating a problem of storage if several conditions and geometries wanted to be studied, also opening and reading these tables can be limited by the memory RAM size available.

The lack of generalization is another limitation in the previous studies. In MCGPU [40, 83] the detector was a 200 μm thick selenium slab with no possibility to change the detector thickness or material. The limitations for generalization in the studies from Day and Tanquay [94] and Stierstorfer [96] was because they used experimental data to fit the charge cloud width, therefore, the simulation is limited to the detector type used in the experimental step.

3.2 Simulation of image acquisition

Most studies focused on simulating image acquisition are optimization studies, which focus mainly on reducing the dose while maintaining acceptable image quality, following the ALARA principle: As Low As Reasonable Achievable [11]. However, currently, there is an interest in simulating realistic images for VCT that are conducted entirely in a digital environment, without the need for physical patient contact or the collection of physical samples [39]. This section focuses on the review of optimization studies for chest radiography, studies on VCT, and studies comparing the impact of different detector technologies in image acquisition.

3.2.1 Optimization of exposure conditions

Recent optimization studies for chest radiography indicate that the X-ray spectrum, characterized by the tube potential and additional filtration, is one of the most important factors to consider since it affects both image quality and dose [98, 99]. The

Figure of Merit *(FOM)* has proven to be a useful quantity to compare the performance of X-ray spectra for optimization purposes since it balances dose and image quality [34, 98–102]. Eq. 3.1 shows a general *FOM* definition for chest radiography.

$$FOM_{IQ,Dose} = \frac{IQ^2}{Dose}, \tag{3.1}$$

where *IQ* represents an image quality index, and *Dose* represents an appropriate dosimetry quantity. This *FOM* definition is valid for detectors where the main noise component is a result of X-ray quanta fluctuations, *FOM* is independent of the X-ray beam intensity [98, 100]. If either the image quality increases or the dose decreases, the *FOM* value increases. Therefore, the optimum exposure conditions maximize the *FOM*.

Several works have studied the optimal X-ray spectrum in chest radiography via *FOM* [34, 36, 98, 99, 101–105]. The traditional quantities used to quantify the image quality in these studies are *SNR* [99] and contrast-to-noise ratio *CNR* [34, 36, 98, 101–104]. The dosimetry quantities used are entrance skin dose (*ESD*) [98, 103, 104], mean absorbed dose (*MAD*) [101], and effective dose (E) [34, 36, 98, 99, 102]. The use of different quantities in the *FOM* definition can affect the optimization process resulting in a variation of established optimal spectra among different studies. Mendes *et al.* [35] compared different *FOM* definitions via *MC* simulation and experimentally. The results show that the use of additional copper (Cu) filtration is indicated for all definitions, which agrees with other studies in the literature [34, 36, 98, 99, 101–104]. Moreover, the optimum tube potential is higher for *FOM* definitions using *SNR* as the image quality index. *CNR* was considered the most indicated image quality index since it evaluates the noise and the contrast. Definitions of *FOM* using *ESD* yielded higher optimum tube potentials and either *MAD* or E are more suitable dosimetric quantities for optimization.

DQE have been used for optimization purposes, usually combined with a dosimetry quantity [106, 107]. However, the main application of *DQE* is to evaluate the performance of the X-ray detector [2]. Lauders *et al.* [106] used the *DQE* and effective dose in an optimization study for thoracic radiography. The *DQE* at 0.25 cycles mm^{-1} was evaluated for different tube potentials without additional filtration. This specific spatial frequency was chosen because it represents the most clinically useful part of the spatial frequency spectrum. Salvagnini *et al.* [107] focused on selecting the optimal exposure parameters for a digital mammographic system using the effective detective quantum efficiency (*eDQE*), an extension of the *DQE* metric including more factors such as the scatter fraction. The *eDQE* was normalized to the mean glandular dose. Experiments were performed for different targets/filters commonly used in mammography.

In summary, image acquisition is a step in optimization studies that focuses on quantifying the image quality with most studies published focusing on varying the exposure conditions and fixing the detector material. Moreover, all the simulation studies cited do not include in the modeling of detection cited the complete conversion of X-ray conversion into an electrical signal resulting in an overestimation of image quality.

3.2.2 Detector technology effect

Regarding detector technologies, there are studies comparing the performance *CR* and *DR* detectors experimentally via metrics such as *MTF*, *NPS* and *DQE* [50, 108, 109]. However, these comparisons were made using standard beam qualities (i.e., specified by the tube potential and additional filtration) established by the report IEC 62220-1-1[110].

Most of the experimental and *MC* studies cited in Section 3.2.1 usually vary the exposure conditions and calculated the *FOM*, but only one type of detector was used in each case. However, few studies are focusing on comparing the effect of different detector technologies on optimization. Martin [105] analytically compared the *FOM* performance for detectors commonly used in CR and DR. While, Mendes *et al.* [35] compared the *FOM* obtained from MC simulations of sensor materials commonly used in CR and DR detectors. Both studies showed that detectors with larger atomic numbers result in better performance. However, these studies included only the photon interactions in the detector. The detailed processes of conversion of X-ray to the final signal, which are dependent on the detector technology, were not included.

3.2.3 Virtual Clinical Trails

There is a great interest in simulating radiography images for VCT since they offer a powerful tool for evaluating and optimizing new imaging techniques and protocols, and can provide valuable insights into the performance of imaging modalities for different applications. Several imaging modalities have been investigated via VCT, for example, breast imaging [40, 111, 112], chest radiography [113] and computed tomography (CT) [38, 39]. The U.S. Food and Drug Administration (FDA) has been exploring the use of VCT in mammography as a means of accelerating the approval process for new devices and imaging technologies [40]. The FDA uses the MCGPU for VCT and as stated in Section 3.1, this code includes a simplified version of *EHP* simulation. Abadi et al. [114] used VCT to investigate the effects of beam collimation and pitch on image quality in computed tomography under different respiratory and cardiac motion rates. Abadi et al. [113] performed VCT for imaging studies of coronavirus disease (COVID-19), enabling effective assessment and optimization of CT and radiography acquisitions and analysis tools for reliable imaging and management of COVID-19. Abadi et al. [115] to develop a VCT framework that simulates a new PCD CT system from Siemens. These studies show the existence of great interest in generating realistic images and simulating in detail the detection can reduce the distance between simulation and experimental results.

Chapter 4

Simulation of Semiconductor Detectors

The Monte Carlo simulation of radiation transport in semiconductor detectors developed in this thesis was divided into: (i) simulation of photons and fast electrons with the PENELOPE v. 2014 [37] with the extension *penEasy* v. 2015 [42] and (ii) simulation of creation, dispersion and trapping of *EHP* in semiconductors. The code developed in this work, which includes the simulation of *EHP* in the PENELOPE code was named THOR: Transport of electrons and HOles in semiconductoRs. Figure 4.1 shows a flowchart of the simulation process.

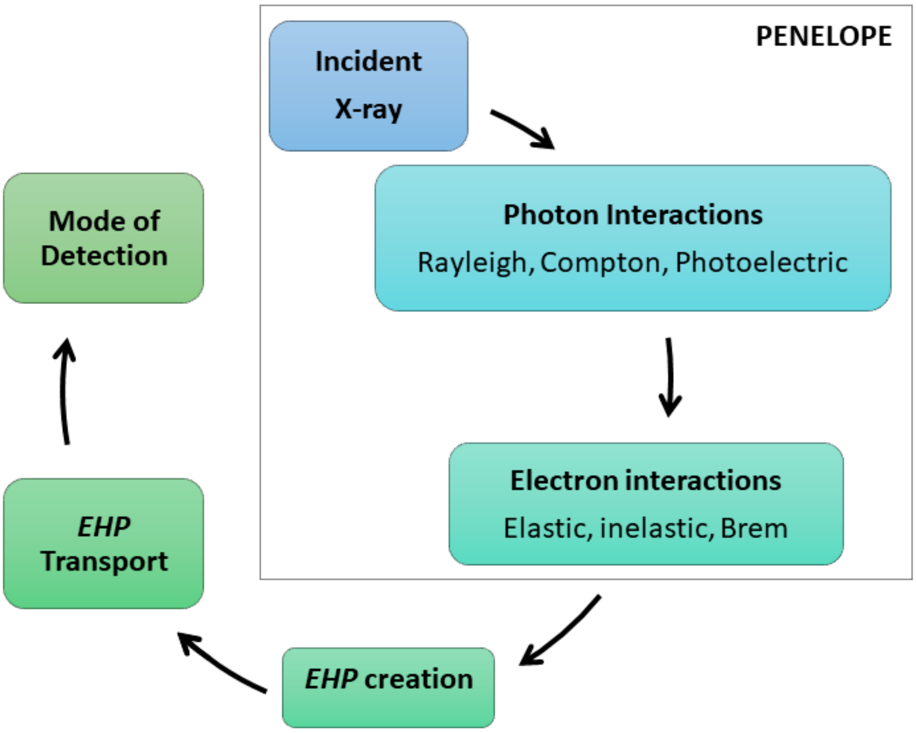

Figure 4.1: Detailed detector simulation flowchart, considering photon and electron interactions and electron-hole pairs creation and dispersion.

The following sections describe the PENELOPE MC code structure for simulating photons and fast electrons, the implementation of *EHP*s creation and transport in the PENELOPE, i.e., the THOR code.

4.1 Simulation with the PENELOPE code

The *MC* code PENELOPE v. 2014 [37] was chosen because it is freely distributed and open source, has a clear and well-documented structure, and is validated in the energy range of interest [37, 42, 116]. In addition, the research group has collaborative projects with one of the original code developers [43]. PENELOPE is an acronym for *PENetration and Energy LOss of Positrons and Electrons* (photon simulations were included after the code was created in 1996) [37].

The PENELOPE code is structured as:

- PENELOPE - consists of preparatory calculations, procedures for simulating interactions, numerical routines for simulating the interaction of radiation with matter;
- PENGEOM - controls the simulation geometry and performs the necessary geometric calculations automatically;
- PENVARED - subroutine that contains variance reduction techniques, used to optimize the simulation time;
- “Main” - responsible for reading input files, calling subroutines and creating output files, so that the desired quantities can be simulated and extracted.

The “Main” used in this work was the penEasy v. 2015 [42], and is divided into tallies, which consist of sub-blocks that are implemented to provide specific quantities and analysis. Each tally has an independent output file, such as energy deposited in the material [42].

The tally of interest for the simulation of radiographic images is the “Tally Pixelated Imaging Detector” (PID). This tally simulates the generation of pixelated images considering different detector types, the size and number of pixels and the detection mode. Energy integrating (EI), photon counting (PC) and energy spectrum are the detection modes present in this tally. In EI detectors, the signal is proportional to the energy deposited in the detector by all photons, information about each photon’s energy without specific information about each photon, such as its energy [27]. PC detectors count individual photons if the signal is above a threshold. The energy spectrum mode determines, for each pixel, the number of photons with a specific energy. The tally PID also allows the production of images using interaction filters considering: all photons, primary photons,

photons scattered by Rayleigh and Compton interactions, secondary photons and multi-scattered photons. Figure 4.2 shows the tally PID section on the penEasy initialization file.

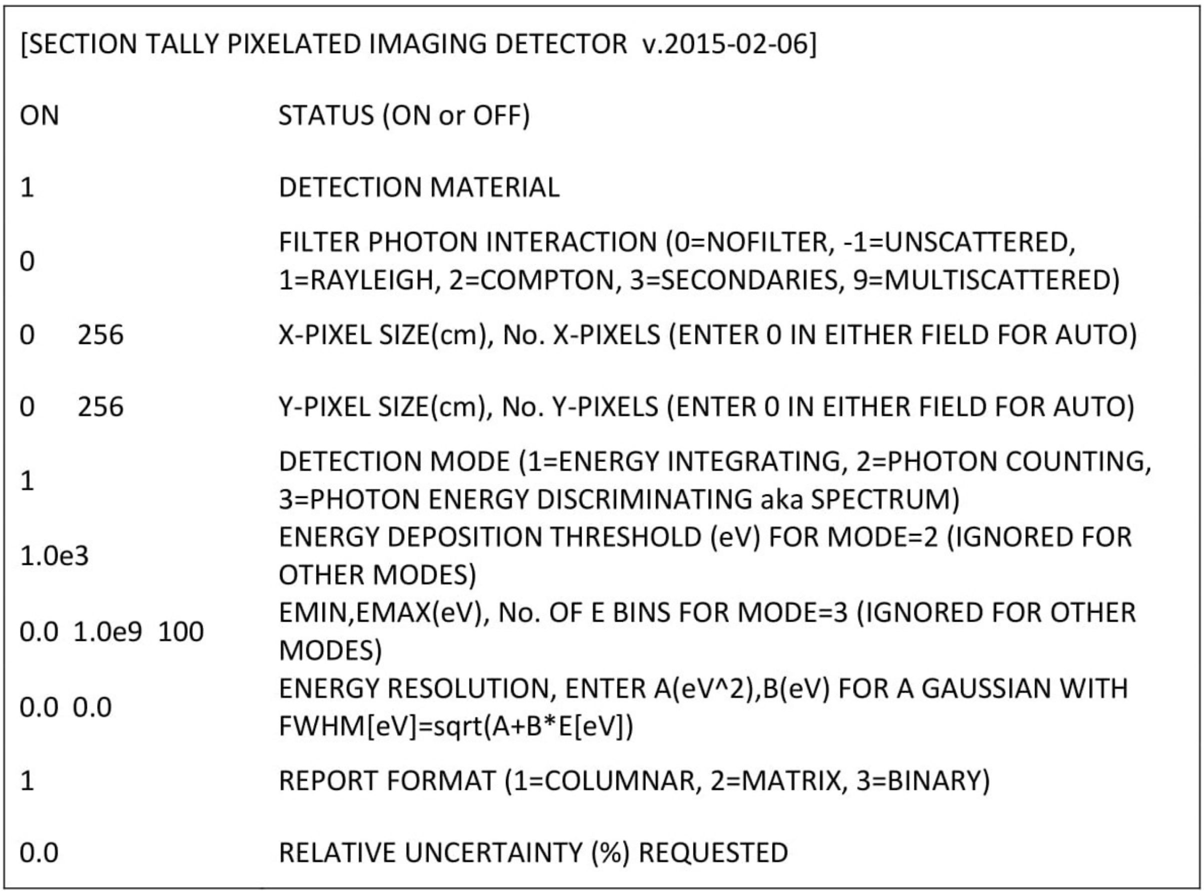

```
[SECTION TALLY PIXELATED IMAGING DETECTOR  v.2015-02-06]

ON                    STATUS (ON or OFF)

1                     DETECTION MATERIAL

                      FILTER PHOTON INTERACTION (0=NOFILTER, -1=UNSCATTERED,
0                     1=RAYLEIGH, 2=COMPTON, 3=SECONDARIES, 9=MULTISCATTERED)

0    256              X-PIXEL SIZE(cm), No. X-PIXELS (ENTER 0 IN EITHER FIELD FOR AUTO)

0    256              Y-PIXEL SIZE(cm), No. Y-PIXELS (ENTER 0 IN EITHER FIELD FOR AUTO)

                      DETECTION MODE (1=ENERGY INTEGRATING, 2=PHOTON COUNTING,
1                     3=PHOTON ENERGY DISCRIMINATING aka SPECTRUM)
                      ENERGY DEPOSITION THRESHOLD (eV) FOR MODE=2 (IGNORED FOR
1.0e3                 OTHER MODES)
                      EMIN,EMAX(eV), No. OF E BINS FOR MODE=3 (IGNORED FOR OTHER
0.0  1.0e9  100       MODES)
                      ENERGY RESOLUTION, ENTER A(eV^2),B(eV) FOR A GAUSSIAN WITH
0.0  0.0              FWHM[eV]=sqrt(A+B*E[eV])

1                     REPORT FORMAT (1=COLUMNAR, 2=MATRIX, 3=BINARY)

0.0                   RELATIVE UNCERTAINTY (%) REQUESTED
```

Figure 4.2: “Tally Pixel Image Detector” section in the input file

In the simulation, if the values of the variables A and B in the energy resolution line (Figure 4.2), are different from zero, after each interaction, a Gaussian dispersion is applied in the energy deposited in a pixel. For all simulations presented in this work, A and B are equal to zero.

The output file from this tally shows the energy deposited and the number of photons counted in each pixel for the EI and PC mode, respectively. For the energy spectrum mode, the output file separates an energy interval, that is defined by the user, into bins, and shows the number of photons counted for each energy bin in each pixel. In all cases, the results are normalized by the number of histories.

The “Tally Particle Track Structure” was also used in this work. This tally tracks each particle in the simulation and the output file shows, for each interaction, the following variables:

- *kpar*: particle type, with 1 and 2 being electrons and photons, respectively;

- *MODE*: interaction that occurred with this particle. The definitions of MODE values for each interaction type are shown in Table 4.1:

Table 4.1: *MODE* values for each type of interaction

MODE	electron (kpar = 1)	photon (kpar = 2)
-1	multiple soft colissions	Rayleigh scattering
-2	hard elastic collisions	Compton scattering
-3	hard inelastic collisions	photoelectric effect
-4	Bremsstrahlung emission	electron-positron pair creation
-5	inner-shell ionization	-

- E_{dep}: energy deposited in the interaction;
- *ilb(1)*: indicates the generation of the particle, incident particles have *ilb(1)* $= 0$;
- *ilb(2)*: indicates the mother particle, if *ilb(1)* $= 0$ then *ilb(2)* $= 0$;
- (x,y,z): interaction position.

At each photon and electron interaction, these variables are updated and it is possible to track the particles' transport through the matter.

The "Tally Particle Track Structure" was used mainly to understand the steps that the PENELOPE code uses to simulate photons and electrons a determinate how the THOR code would be implemented.

4.2 THOR Implementation in the PENELOPE

The simulation of creation, dispersion and trapping of *EHP* was implemented in this work by modifying the "Tally Pixelated Imaging Detector" present in the penEasy v. 2015 [42]. The THOR code was created because the PENELOPE code [37] does not simulate electric fields and the material's crystalline structure.

The simulation of charge dispersion in a semiconductor implemented in this work was based on *PenEasy Imaging* [42], developed by Andreu Badal for the simulation of imaging systems, mainly scintillator detectors [117]. This Tally was first modified by Debora P. Magalhães, a former student of the research group [86]. In this previous version of the semiconductor detector modeling, the *EHP* were generated only via photoelectric interaction. However, this work includes the entire description of photons and electrons interactions, as well as the charge trapping effects.

4.2.1 Electron-hole pair creation

The creation of *EHP*s was the first step for the implementation of the detector model. For each electron interaction, the E_{dep} was converted into *EHP*s, where the number of pairs created was sampled using a Poisson distribution modulated by the sensor's Fano factor and the average number of *EHP* created (Q_{total}):

$$Q_{total} = \frac{E_{dep}}{W_{\pm}}, \tag{4.1}$$

where $W_{\pm}$ is the energy required to produce an *EHP* in the detector.

The $W_{\pm}$ value is unique for each detector material and is usually independent of the electric field and beam energy [53, 54]. However, for amorphous selenium (a-Se), the photoconductor most used in medical imaging, studies show that there is a dependency of $W_{\pm}$ due to mainly recombination processes [53, 54, 118]. Therefore, the empirical equation obtained by Kabir et al. [54] for the a-Se was used to determinate the $W_{\pm}$ value as:

$$W_{\pm}(F, E) = \left(6 + \frac{300}{F^{0.9}}\right)\left(0.38 + \frac{4.8}{E^{0.5}}\right) eV, \tag{4.2}$$

where F is the applied electric field in V/μm, E is the photon incident energy in keV. This equation was obtained with E between 10-140 keV and F between 1-100 V/μm [54]. In this work, if E or F were outside these intervals $W_{\pm}$ was equal to the value normally used in the literature: 50 eV [119].

4.2.2 Charge dispersion

When F is 0 V/μm, the *EHP*s created follow a random thermal motion, diffusing away from their point of origin [52]. When an F is different from zero, the *EHP*s will undergo a net migration. The motion will be the combination of a random thermal velocity and a net drift velocity parallel to the direction of F [52].

Considering a detector with its width and length on the XY plane, height in the z direction, and a constant F in the z direction, if all electrons (or holes) were created in the same position, the charges distribution cross section can be approximated by the Gaussian function:

$$f(x, y) = Z \times exp\left(-\frac{(x - x_0) + (y - y_0)}{2\sigma^2}\right), \tag{4.3}$$

where:

- x_0 and y_0 are the coordinates on the detector, where an interaction occurred;

- Z is the interaction height (on the z direction).
- x and y is the charge final position, i.e., the position reaching the electrode;
- σ is the standard deviation (which is symmetric around the z axis).

σ quantifies the charge dispersion within a material as:

$$\sigma = \sqrt{2Dt}, \tag{4.4}$$

where D is the diffusion coefficient and t is the drift time. The D can be obtained from the Einstein equation [120]:

$$D = \frac{\mu_e k_B T}{e}, \tag{4.5}$$

where μ is the charge carrier mobility in the sensor material, k_B is the Boltzmann constant (1.380649×10^{-23} m^2 kg s^{-2} K^{-1}), T is the sensor temperature and e is the elementary charge (1.602×10^{-19}C). At low-to-moderate values of electric field (F) the drift velocity v is proportional to the applied field [87]:

$$v = \mu \times F. \tag{4.6}$$

For a specific F value the drift velocity is constant, therefore:

$$v = \frac{Z}{t}. \tag{4.7}$$

Combining the equations (4.4) - (4.7) σ is equal to:

$$\sigma = \sqrt{\frac{2k_B T Z}{eF}}. \tag{4.8}$$

Equation 4.8 was obtained with the assumption that the electric field was uniform throughout the sensor which is valid as the pixel size is smaller than the detector thickness.

As shown in Equation (4.8), the sampling performed in this section does not differentiate between electrons and holes, even though in reality they have different mobilities [57]. The only difference between an electron and a hole in this step is the distance that they traveled which also depends on the direction of the electric field applied (bias). Figure 4.3 shows the distance traveled by the electron and hole for (a) positive and (b) negative bias. For each case, the distance traveled by the charge carrier should replace the Z on Equation 4.8;

Figure 4.4 shows examples of Gaussian sampling with a mean equal to zero (representing the center of a pixel) and the standard deviation is given by Equation 4.8. Sampling was performed using the Box-Muller method [121]. Three different F values (0.1,

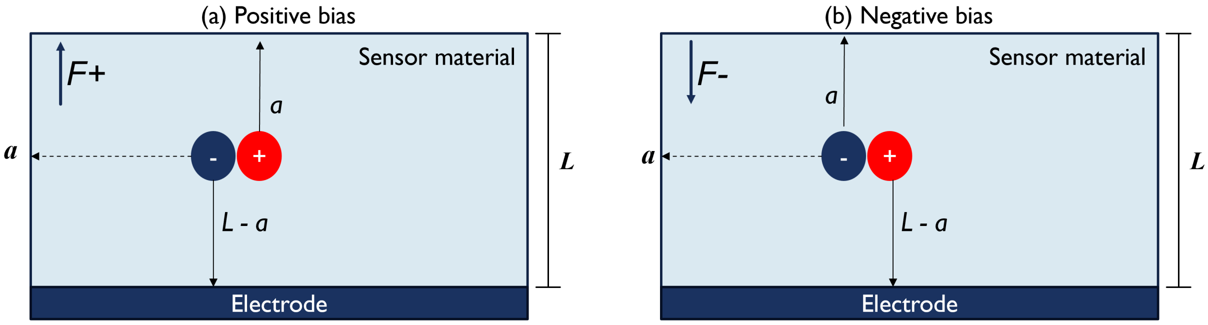

Figure 4.3: Distance traveled by an electron and a hole created at the position a in a sensor material with a thickness equal to L for the cases of a (a) positive and a (b) negative bias.

1 and 10 V/μm) were used and Z was equal to (a) 150 and (b) 500 μm, which are the detector thicknesses used in mammography [72] and chest radiography [25], respectively. In all cases, the temperature was 298 K. These cases represent the case of a positive bias and collecting holes.

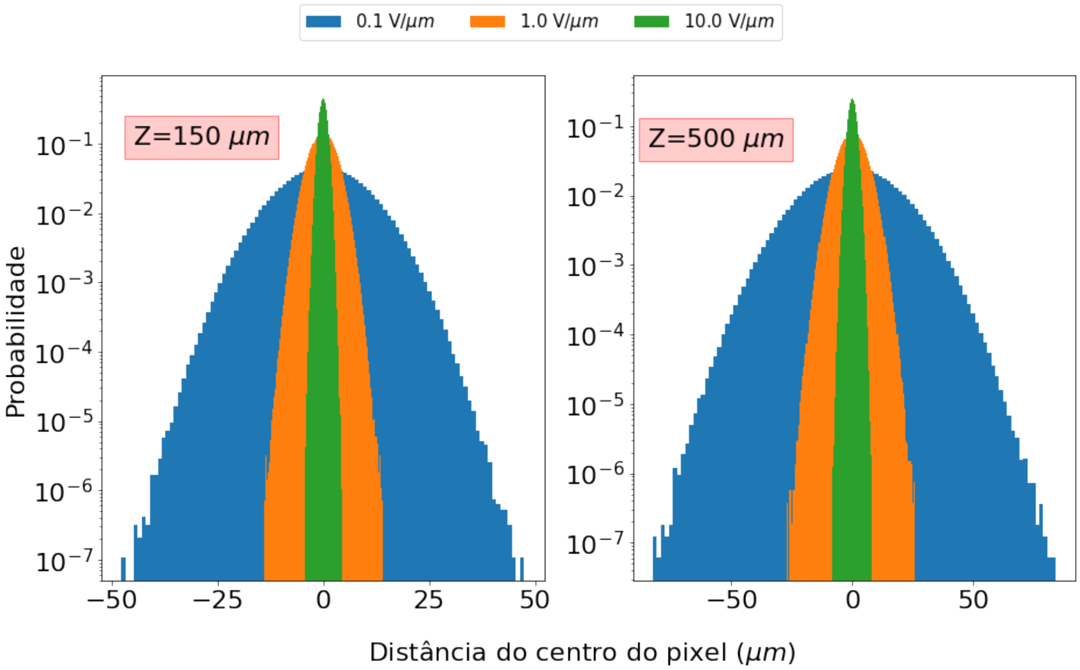

Figure 4.4: Example of Gaussian sampling for three different values of electric field and also when Z is equal to (a) 150 and (b) 500 μm.

The distribution becomes wider when increasing the value of Z and decreasing F, as shown in Figure 4.4. A typical pixel size of a-Se detectors used in chest radiography is 139 μm [49], in this case, figure 4.4 indicates that if the value of the field is 10 V/μm an *EHP* created at the center of the pixel has a higher probability to stay in the same pixel than the case where $F = 0.1$ V/μm.

4.2.3 Charge Trapping

Charge trapping was included using the Hetch equation [122], in which the collection efficiency (λ) is given by:

$$\lambda = \frac{\mu\tau E}{L}\left[1 - exp\left(\frac{-Z}{\mu\tau E}\right)\right]. \tag{4.9}$$

Because of the constants μ and τ, the charge trapping has different results by considering the transport of electrons or holes. Moreover, the electric field direction is also a factor, since the Z value changes depending if a positive or a negative bias was applied.

In the code, for each change carrier, a random number between 0 and 1 was sampled, if the number was larger than λ, the charge was considered trapped.

4.2.4 Modes of Detection

The code developed in this study simulates two types of detectors: energy integrating (EI) and photon counting (PC). For the EI mode, after the charge dispersion, each electron detected in a pixel was counted and converted into energy deposited by multiplying by $W_{\pm}$. In the PC mode, when the history ends, if the energy deposited in each pixel was higher than an energy threshold ($ethr$), determined by the user, then the photon was counted. Because of the PENELOPE structure when simulating particles, it was necessary to introduce a variable to discriminate the electrons created directly from the incident photon, from fluorescence, and Compton-scatted photons.

4.2.5 Input data for the model

To model the detector including the creation, transport and trapping, the tally *PID* section on the input file for the simulation was modified. New variables were included:

- the electric field applied value in V/cm (the value can be either positive or negative);
- which charge carrier will be collected: electron or hole;
- the Fano Factor;
- $W_{\pm}$ for sensor materials other than a-Se, in this case, Equation 4.2 is used;
- an integer to define whether charge trapping is considered or not;
- the electron mobility-lifetime ($\mu_e\tau_e$) in cm^2/V;

- the hole mobility-lifetime ($\mu_h \tau_h$) in cm^2/V;
- the number of pixels in the detector or the pixel size;
- an integer to define which detector mode to use;
- the *ethr* used specifically for the PC mode.

Figure 4.5 shows the modified Tally PID section in the penEasy configuration file.

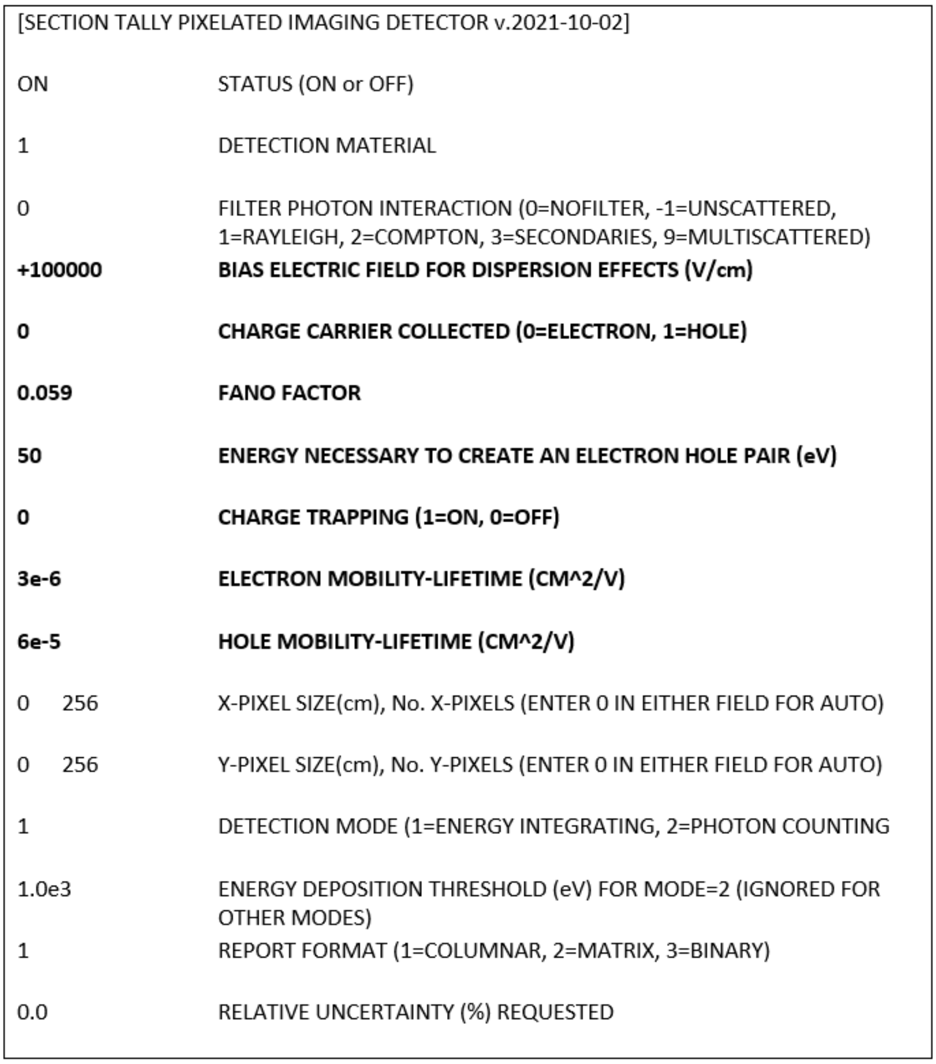

```
[SECTION TALLY PIXELATED IMAGING DETECTOR v.2021-10-02]

ON              STATUS (ON or OFF)

1               DETECTION MATERIAL

0               FILTER PHOTON INTERACTION (0=NOFILTER, -1=UNSCATTERED,
                1=RAYLEIGH, 2=COMPTON, 3=SECONDARIES, 9=MULTISCATTERED)
+100000         BIAS ELECTRIC FIELD FOR DISPERSION EFFECTS (V/cm)

0               CHARGE CARRIER COLLECTED (0=ELECTRON, 1=HOLE)

0.059           FANO FACTOR

50              ENERGY NECESSARY TO CREATE AN ELECTRON HOLE PAIR (eV)

0               CHARGE TRAPPING (1=ON, 0=OFF)

3e-6            ELECTRON MOBILITY-LIFETIME (CM^2/V)

6e-5            HOLE MOBILITY-LIFETIME (CM^2/V)

0   256         X-PIXEL SIZE(cm), No. X-PIXELS (ENTER 0 IN EITHER FIELD FOR AUTO)

0   256         Y-PIXEL SIZE(cm), No. Y-PIXELS (ENTER 0 IN EITHER FIELD FOR AUTO)

1               DETECTION MODE (1=ENERGY INTEGRATING, 2=PHOTON COUNTING

1.0e3           ENERGY DEPOSITION THRESHOLD (eV) FOR MODE=2 (IGNORED FOR
                OTHER MODES)
1               REPORT FORMAT (1=COLUMNAR, 2=MATRIX, 3=BINARY)

0.0             RELATIVE UNCERTAINTY (%) REQUESTED
```

Figure 4.5: Modified Tally Pixel Image Detector section in the input file, evidencing the changes made for the detailed detector simulation

The spectrum mode that was present on the original tally PID was not included in the THOR code. The variables to define the energy resolution were also excluded. These variables were included on penEasy to introduce a more realistic energy resolution. However, in the THOR code, this is done by the Fano Factor and $W_{\pm}$ in the creation of *EHP*s (Section 4.2.1).

Chapter 5

Characterization of detectors simulations

This chapter shows the THOR code validation using studies in the literature by evaluating the energy and spatial resolution, noise, and efficiency were evaluated. Also, the THOR code was used to explore the detector response varying electric fields, detector's thicknesses, pixel size and materials.

5.1 Methods

The PENELOPE code v. 2014 [37] with the penEasy v. 2015 [42] extension were used to simulate the photons and fast electrons. The THOR code, described in Chapter 4, adapts one of the penEasy tallies to simulate *EHP* creation and transport. Table 5.1 shows your main settings of the computers that were used to carry out the simulations of this work.

Table 5.1: Technical information for the computers used in the simulations

CPU	Core/Threads	RAM (GB)	OS
Intel Core® i5 8250U 1,8 GHz	4/8	8	Windows 10
AMD Ryzen® 2700 3.2 GHz	8/16	16	Ubuntu
Intel Xeon Silver® 4210R 2,4 GHz	10/20	64	Ubuntu

In the simulations, the cut-off energy for photons and electrons absorption was 50 eV, the parameters C_1 and C_2 were equal to zero, and WCC and WCR were equal to 100 eV.

5.1.1 Simulation Geometry

The simulation geometry consists of a detector with an area of 2.5×2.5 cm^2, its thickness varying from 150 to 1000 μm, the pixel size varied from 5 to 150 μm, the applied electric field (F) varied from 1 to 30 V/μm. The EI and PC detector modes were used. For the EI case, three different detector materials were explored: amorphous selenium (a-Se), mercuric iodine (HgI_2), and lead iodine (PbI_2). On the other hand, for the PC mode, the materials were explored: silicon (Si), cadmium telluride (CdTe) and gallium arsenide (GaAs). Table 5.2 shows the Fano Factor, $W_{\pm}$, $\mu_e \tau_e$ and density for the materials used in the simulations. The X-ray source was a monoenergetic pencil beam reaching the detector center with energies varying between 10 and 140 keV. For all cases, the number of stories was fixed at $1{\times}10^7$ to guarantee that uncertainties were below 3% (1σ). All simulations were performed with a negative F and collecting only electrons.

Table 5.2: Sensor characteristics used in the EI and PC modes simulations [60, 62, 63]

Mode	Detector Material	Fano Factor	$W_{\pm}$ (eV)	Density (g/cm³)
Energy Integrating (EI)	a-Se	0.059	Variable	4.5
	PbI_2	0.19	4.9	6.2
	HgI_2	0.18	4.2	6.4
Photon Counting (PC)	Si	0.115	3.62	2.33
	CdTe	0.15	4.53	5.85
	GaAs	0.12	4.2	5.32

5.1.2 Calculation of metrics for detector characterization

The Swank Factor (I) was used quantify the energy resolution, the *MTF* quantified the spatial resolution, the *NPS* quantified the noise, and the efficiency was quantified by η and *DQE*.

Swank Factor (I)

In each simulation history, the number of *EHP*s detected was saved in a file, the histogram of these values is the pulse-height spectrum (*PHS*). I was calculated as:

$$I = \frac{M_1^2}{M_0 M_2}, \tag{5.1}$$

where M_n is the nth moment of the *PHS*, that can be calculated as:

$$M_j = \int_0^{\infty} E^j \times PHS(E) dE. \tag{5.2}$$

MTF

The *PSF* was obtained directly from the simulations. In the EI mode, the *PSF* is the number of *EHP* detected in each pixel normalized by the number of histories. On the other hand, in the PC mode, the *PSF* is the number of photons detected in each pixel normalized by the number of histories. The *LSF* is calculated from the *PSF*. For a detector without damaged pixels, the *PSF(x,y)* is isotropic. Therefore, the integral can be calculated either in the x or y directions. The *MTF* is calculate as:

$$MTF(f) = \left| DFT\Big(LSF(x) \Big) \right|, \tag{5.3}$$

where *DFT* is the discrete Fourier transform and f is the spatial frequency.

NPS

The *NPS* was calculated using the Lubberts method [123, 124]. This calculation involves summing the *PSF* along a single dimension to obtain a *PSF* projection that is then Fourier transformed, squared, as:

$$NPS(f) = \left| DFT\Big(\sum_x PSF(x,y) \Big) \right|^2, \tag{5.4}$$

DQE and η

For a monoenergetic beam, η is equal to the ratio between the energy deposited in the detector and the photon initial energy. With the I and η is possible to calculate the *DQE* at zero spatial frequency as:

$$DQE(0) = \eta \times I \tag{5.5}$$

The *DQE* as a function of the spatial frequency was obtained using the Fujita-Lubberts-Swank method [124, 125]. This method takes into account all quantities describe in this section and *DQE(f)* was calculated as:

$$DQE(f) = DQE(0) \times NPS(0) \frac{MTF(f)^2}{NPS(f)} \tag{5.6}$$

5.2 Validations

The validations were performed using the ARTEMIS code developed by Fang et al 2012 [72]. This code was chosen because it is the most detailed code among the studies simulating *EHP* transport (Section 3.1). Moreover, it was validated using experimental data, and it uses the PENELOPE code to simulate photons and electrons. The major drawback for the ARTEMIS code is its low simulation speed, around 0.5 histories per second, while the THOR code is around 500 times faster. All the validations were performed using an a-Se detector.

Swank Factor

A study from Fang et al. [72] was used to validate the *I*. For this purpose, the detector was 150 μm thick and composed of a-Se with $F = 30$ V/μm. Figure 5.1 shows *I* for the THOR code developed in this project and the ARTEMIS code.

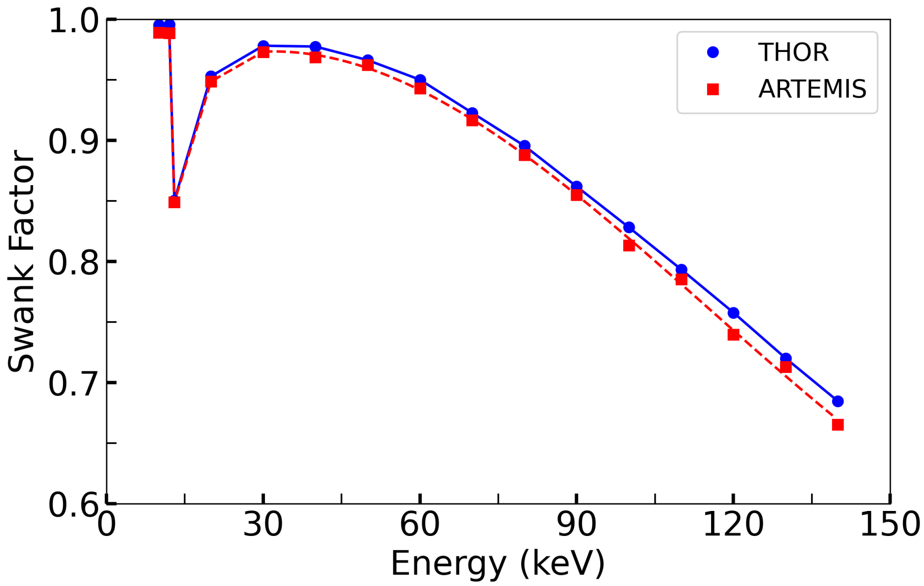

Figure 5.1: *I* for the THOR code developed in this project and the ARTEMIS code [72]. The results presented were for $F = 30$ V/μm.

The THOR code provides higher values of *I* for all photon energies. The average relative difference between the THOR and ARTEMIS codes was 1.0 ± 0.7%. Therefore, the results between the codes agree, given the established uncertainties.

MTF

To validate *MTF* there studies were used: Fang et al. [126], Fang and Badano [125] and Cheng et al. [127]. The studies used different energies, detector thickness, and pixel sizes, Table 5.3 shows the simulation parameters for each case. For all cases, the applied electric field was 10 V/μm and the number of stories was $1{\times}10^7$.

Table 5.3: Simulation parameters for the *MTF* validation

Study	Detector thickness (μm)	Pixel size (μm)
Fang et al. [126]	1000	5
Fang and Badano [125]	240	150
Cheng et al. [127]	200	5

Figure 5.2 shows the *PSF(x,y)* for (a) 10 keV, (b) 13 keV, (c) 30 keV and

(d) 100 keV with the 1000 μm thick a-Se detector and pixel size of 5 μm. Above and on the right of the *PSF* is the normalized *LSF* integrated over x and y, respectively.

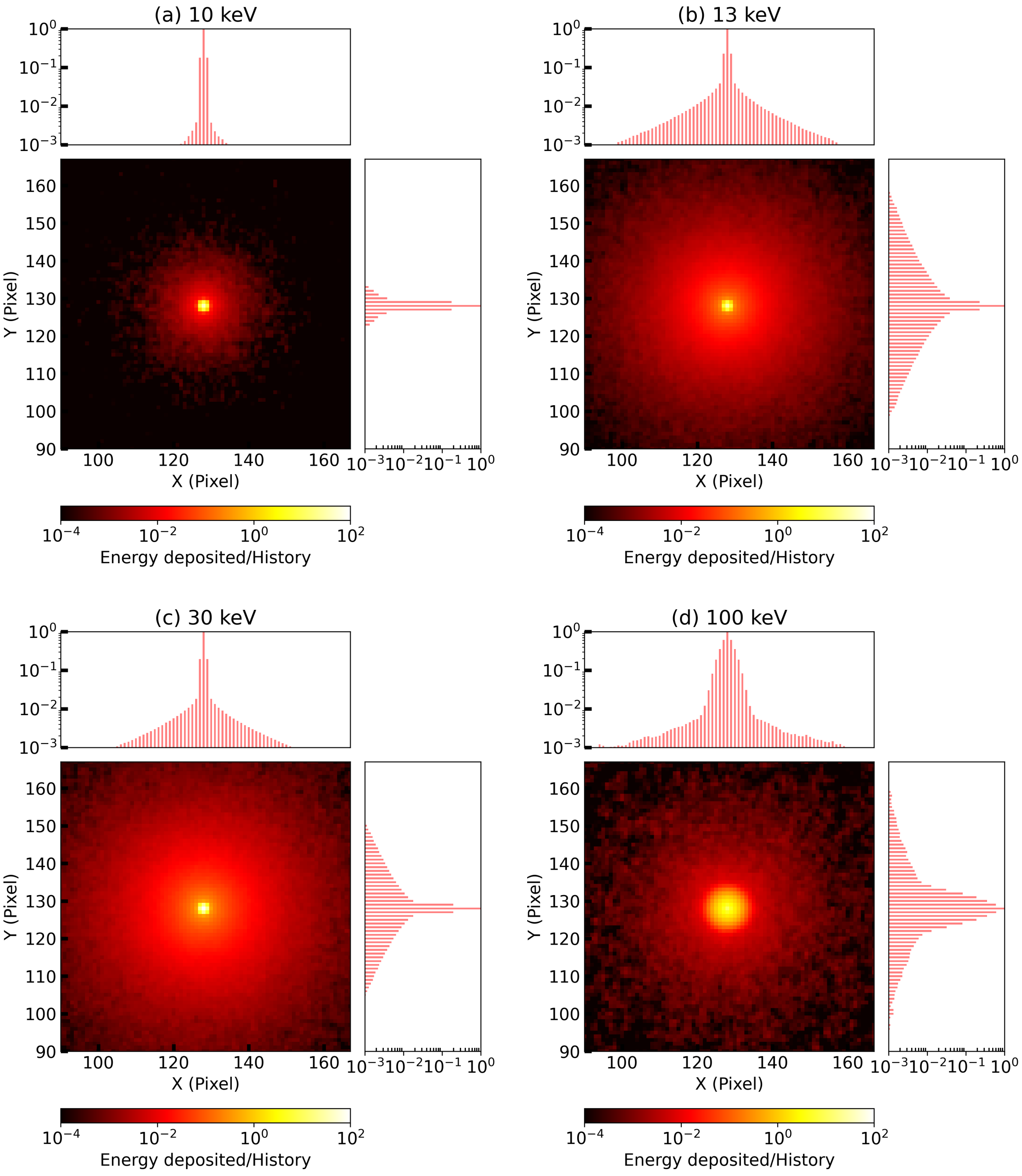

Figure 5.2: *PSF(x,y)* for (a) 10 keV, (b) 13 keV, (c) 30 keV and (d) 100 keV with the 1000 μm thick a-Se detector and 5 μm pixel size. Above and at the right of the *PSF* is the normalized *LSF* integrated over x and y, respectively.

The *PSF(x,y)* is isotropic for all cases of incident energy, as expected, this was better demonstrated on the *LSF* curves. For the 10 keV case, Figure 5.2 (a), the narrowest detector response was observed. Is expected that the detector response becomes wider with the energy, due to the increase in photon mean-free path and electron range.

However, the *PSF(x,y)* for 13 keV is wider than the case for 30 keV, since 13 keV is right above the selenium K-edge therefore, the generation and re-absorption of fluorescence x-rays are more influential than for the 30 keV case. The widest response is observed for the 100 keV case, Figure 5.2 (d), due to the higher probability of Compton scattering at this energy. This is especially apparent in the *LSF*s, where the curves are wider at the center.

The *MTF* comparison with the THOR code and the studies from (a) Fang et al. [126] and (b) Fang and Badano [125] and (c) Cheng et al. [127] are presented in Figure 5.3.

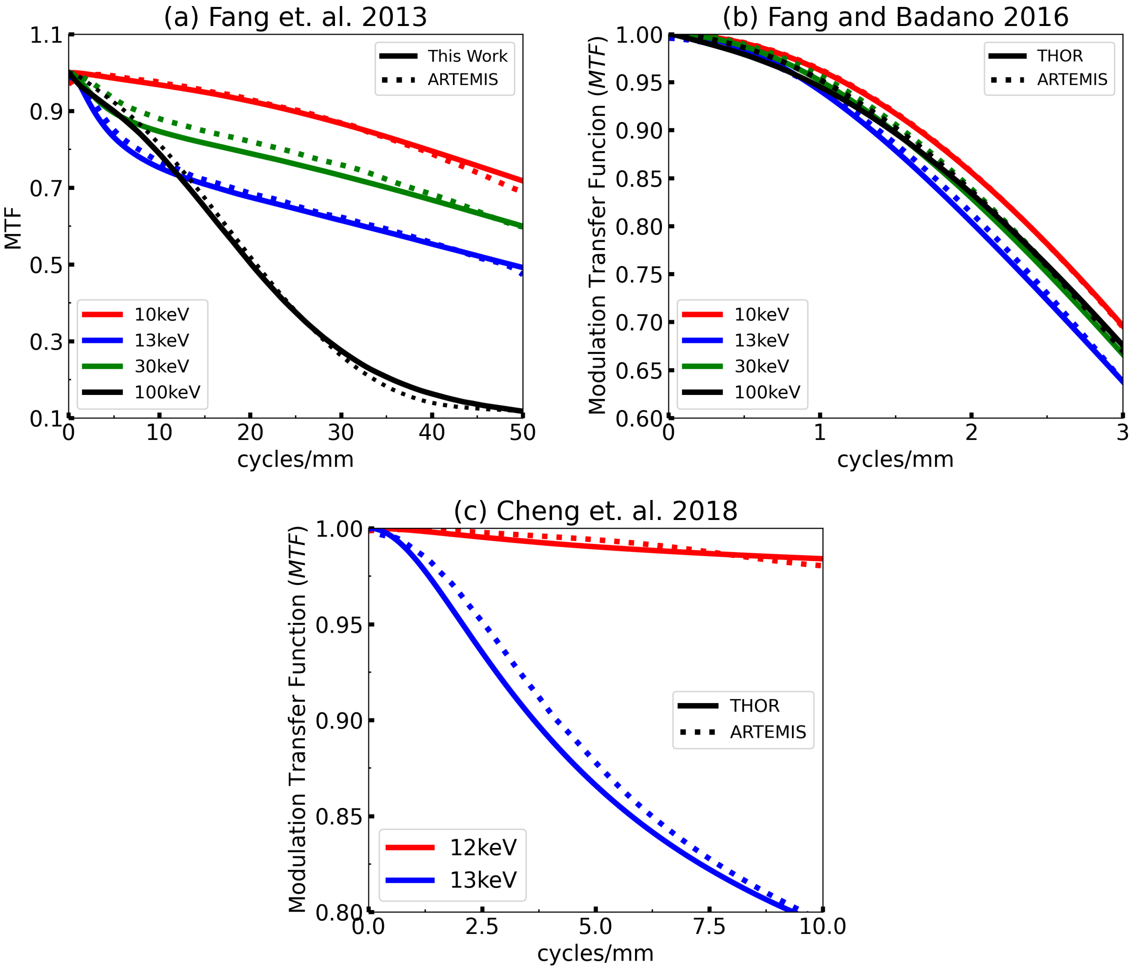

Figure 5.3: *MTF* comparison between the THOR code and the studies (a) Fang et al. 2013 [126] and (b) Fang and Badano 2016 [125] and (c) Cheng et al. 2018 [127].

Similarly, with the *PSF* and *LSF* graphs, the *MTF* curves showed that the spatial resolution decreases with the energy, except for the 13 keV curve that has lower values than the 30 keV case. Comparing the THOR and ARTEMIS codes for lower energies, the *MTF* curves are similar, with the average relative differences equal around 1% for energies between 10 and 13 keV. For 30 and 100 keV the average relative difference increases to 3 ± 2% and 4 ± 2%, respectively. Even though the differences are larger, the studies agree considering the uncertainties.

NPS

The *NPS* was validated using the study from Fang and Badano [125], in this case F was equal to 10 V/μm, the pixel size was 150 μm and the detector thickness was 240 μm. Figure 5.4 shows the *NPS* obtained with the THOR and ARTEMIS codes. The relative difference between the codes was 2 ± 4%.

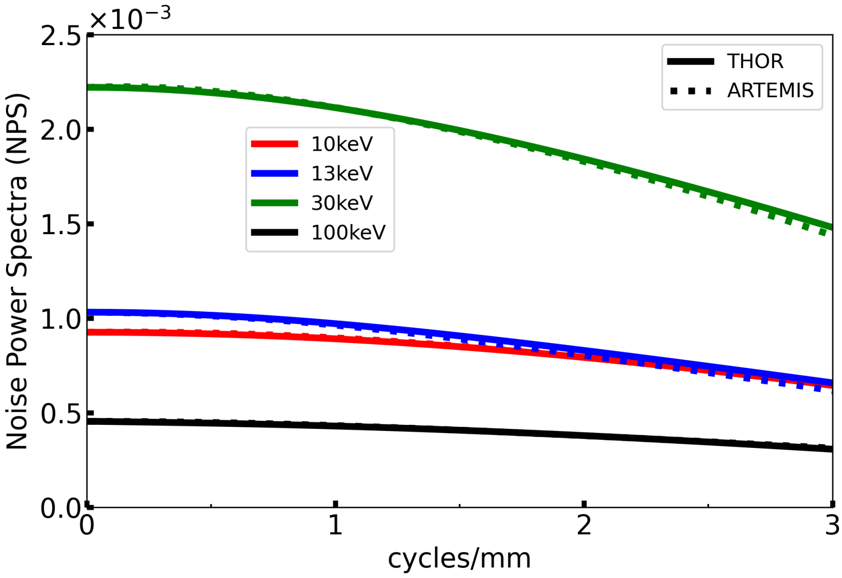

Figure 5.4: THOR and ARTEMIS codes results for *NPS(f)* for a 240μm thick a-Se detector, pixel size of 150 μm, F = 10 V/μm and 1×10^7 histories.

DQE and η

A study from Fang et al. [72] was used to validate the η and DQE at zero spatial frequency. In this study, the detector was an 150 μm thick a-Se detector and F = 30 V/μm. Figure 5.5 shows (a) η and (b) DQE at zero spatial frequency for the THOR ARTEMIS codes.

For both η and DQE, the THOR and ARTEMIS had similar results. The average relative difference between the THOR and ARTEMIS codes were 2 ± 1% and 3 ± 1% for η and $DQE(E)$, respectively, with this relative difference increasing with the beam energy. Therefore, the results between the codes agree, given the established uncertainties.

The *DQE(f)* was validated using the study from Fang and Badano [125], in this case, F was equal to 10 V/μm, the pixel size was 150 μm and the detector thickness was 240 μm. Figure 5.6 shows the *DQE(f)* obtained with the THOR and ARTEMIS codes.

The *DQE(f)* decreases with the photon energy and the largest differences between the codes occurred for the 13 keV case, similarly with the *MTF* and *NPS*. However, the average relative difference is only 3 ± 2%, which is low considering the established

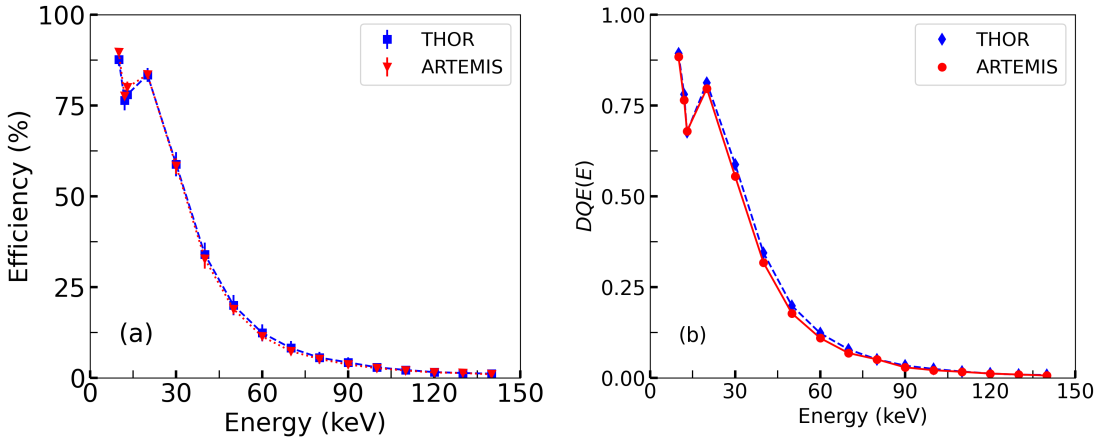

Figure 5.5: THOR and ARTEMIS codes results for (a) η and (b) DQE at zero spatial frequency for a 150 μm thick a-Se detector, and F = 30 V/μm.

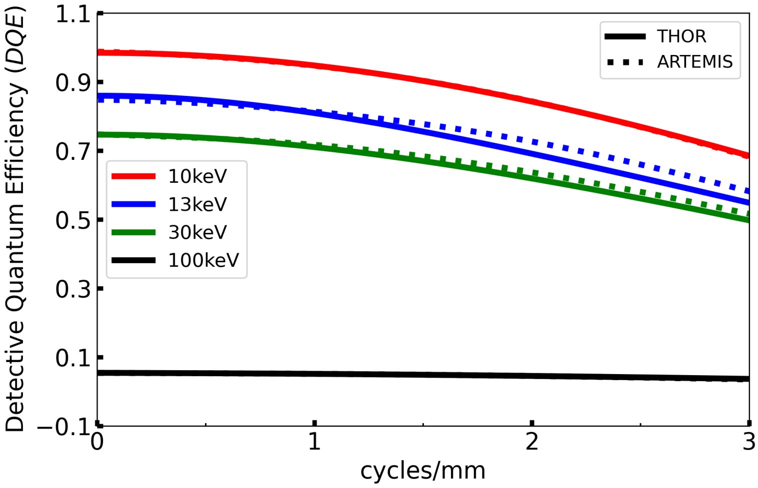

Figure 5.6: THOR and ARTEMIS codes results for $DQE(f)$ for a 240 μm thick a-Se detector, pixel size of 150 μm, F = 10 V/μm and $1{\times}10^7$ histories.

uncertainties.

5.3 Detector response simulations

In this section, the detector model described in Section 4.2 and validated in Section 5.2 is explored to investigate the detector response for different sensor material and thicknesses normally used in direct DR (EI mode) and PC detectors.

5.3.1 Energy Integrating

Comparison with the PENELOPE code

To quantify the effect of *EHP* creation and transport, simulations were performed with the PENELOPE and THOR codes. Figure 5.7 shows (a) the I, (b) η and (c) DQE at a spatial frequency equal to zero, for an a-Se detector with a thickness equal to 150 μm and $F = 30$ V/μm.

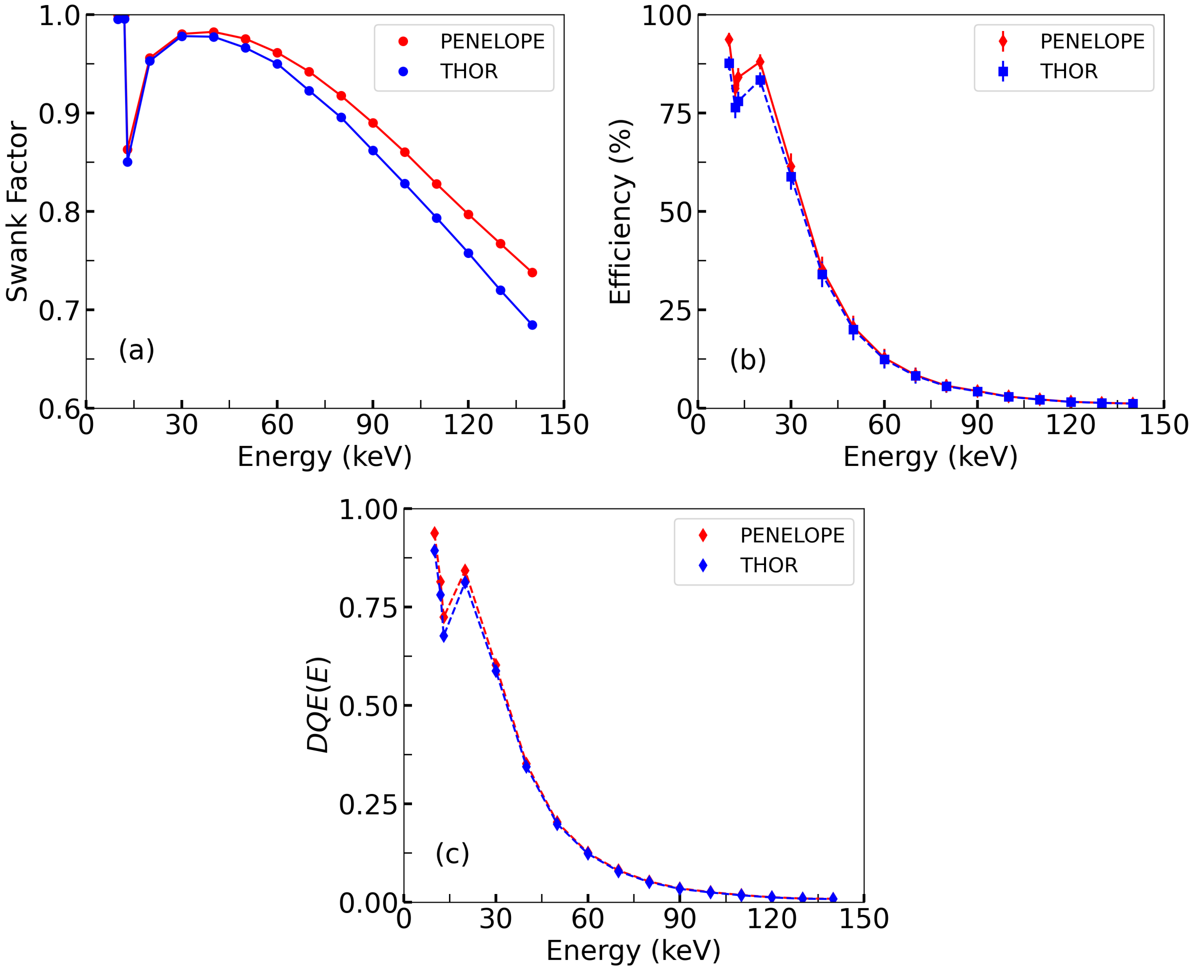

Figure 5.7: THOR and PENELOPE codes results for (a) I, (b) η and (c) DQE at zero spatial frequency for a 150 μm thick a-Se detector, and $F = 30$ V/μm.

For all quantities depicted in Figure 5.7, the PENELOPE code presents the highest values, indicating that the PENELOPE code overestimates the energy resolution and efficiency. The inclusion of the *EHP* transport decreases the I in $3 \pm 2\%$, η in $7 \pm 5\%$, and $DQE(E)$ in $4 \pm 2\%$.

The *EHP* simulation effect on the image resolution was also evaluated, Figure 5.8 shows the (a) *LSF* and (b) *MTF* comparing the cases with and without the charge dispersion (only PENELOPE). The values were obtained for photon energies of 100 keV and when the dispersion was included the bias was 1 V/μm.

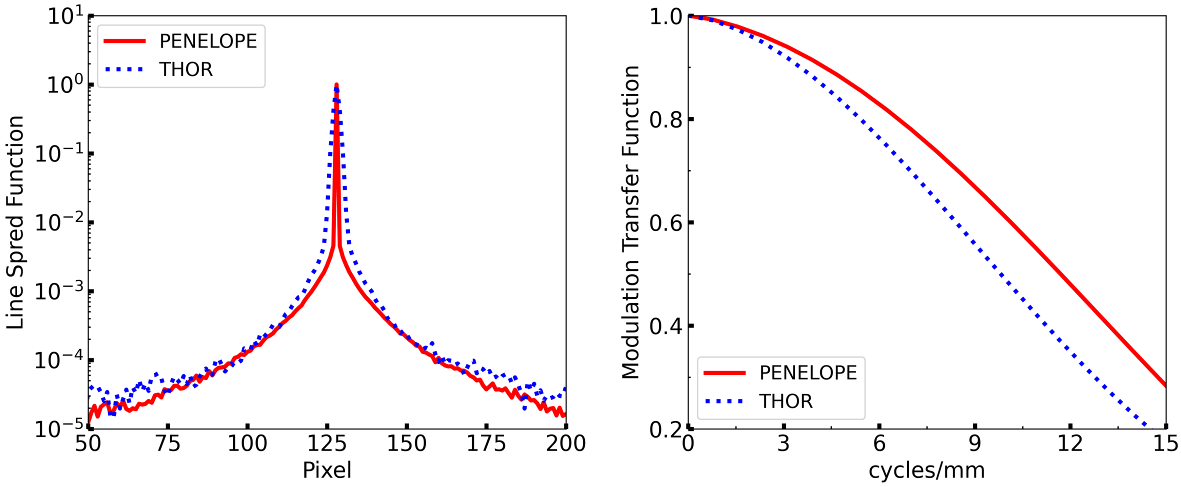

Figure 5.8: Simulated (a) *LSF* and (b) for a-Se detectors with 100 keV incident energy without (only PENELOPE code) and with the charge dispersion.

Simulating only with the PENELOPE code results in a narrow *LSF*, but with the THOR code a *LSF* wider spread can be observed. This occurs, because with the inclusion of the transport of *EHP* the spatial resolution. The relative difference between the central pixel and its adjacent is equal to 99.54% and 58.38% without and with dispersion. This result shows that the simulation without the charge dispersion results in a better spatial resolution. This is also observed for the *MTF* where its value at 0.5, a common quantity to determine the spatial resolution, is 11.67 and 10.89 cycles/mm.

Fixed or variable $W_{\pm}$

Figure 5.9 shows a comparison of the *EHP*s created with created with (a) $W_{\pm}$ = 50 eV and (b) varying $W_{\pm}$ using Equation 4.2 for an a-Se detector 500 μm thick, F = 4 V/μm and monoenergetic pencil beams of 20 and 60 keV.

Using the Equation 5.9 will result in a decrease on the number of pairs created with the electric field for both energies, this is a direct result from the $W_{\pm}$ increase when F decreases. For example, $W_{\pm}$ is approximately 92 eV when E = 50 keV and F = 4 V/μm. On the other hand, when F = 10 V/μm $W_{\pm}$ is approximately 46 eV.

Simulations were performed to compare the use of $W_{\pm}$ fixed at 50 eV and varying. The results showed less than 0.5% relative difference for the I, this result is expected because the Fano Factor was fixed at 0.059 in both cases. For η the average relative difference between $W_{\pm}$ fixed and variable was -6 ±4%, with this difference decreasing with the energy. This is direct result of the $W_{\pm}$ decrease as the energy increases.

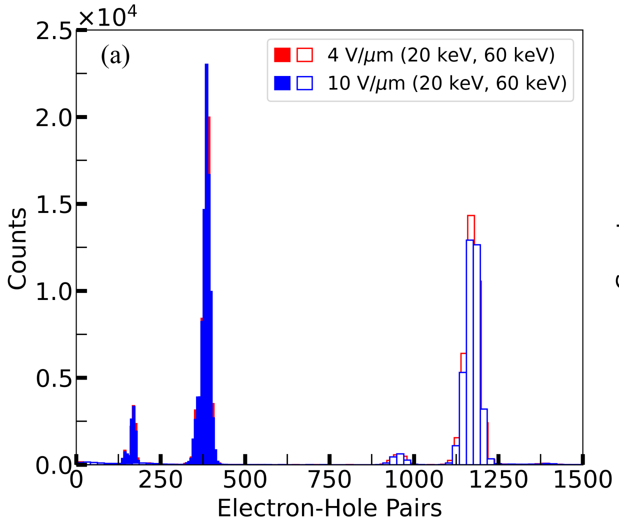

Figure 5.9: Number of *EHP* created with (a) $W_{\pm}$ = 50 eV and (b) varying $W_{\pm}$ using Equation 4.2. The simulations were performed for an a-Se detector 500 μm thick, monoenergetic pencil beams of 20 and 60 keV, F = 4 and 10 V/μm.

Pixel size

Aiming to determine the effect of pixel value on the image quality characteristics, Figure 5.10 shows the (a) *MTF* calculated varying the pixel size from 5 to 150 μm, F = 10 V/μm and 20 keV, (b) the frequency where the *MTF* is 50%.

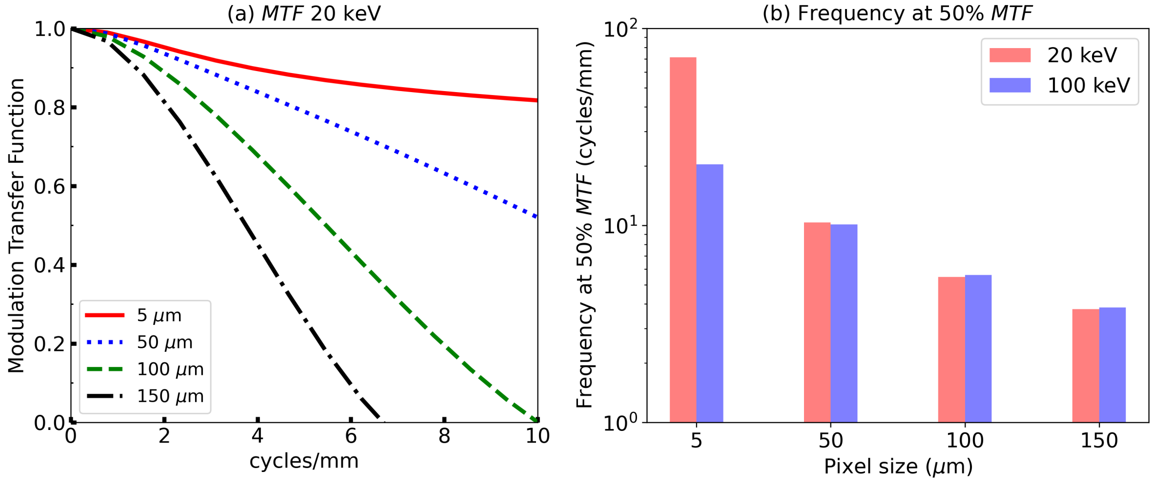

Figure 5.10: (a) *MTF* calculated varying the pixel size from 5 to 150 μm, F = 10 V/μm and 20 keV, (b) the frequency where the *MTF* is 50%.

As the pixel size increases, the *MTF* decreases, which is expected since the spatial resolution is directly related to the size of the pixel. Figure 5.10 (b) shows also that the spatial resolution decreases with the energy, for instance, the frequency where the *MTF* is 50% for a 5 μm pixel is 71.4 and 20.5 cycles/mm, for 20 and 100 keV, respectively. However, this difference decreases as the pixel size increases.

Figure 5.11 shows the *NPS* calculated varying the pixel size from 5 to 150 μm, F = 10 V/μm and two energies (a) 20 keV and (b) 60 keV.

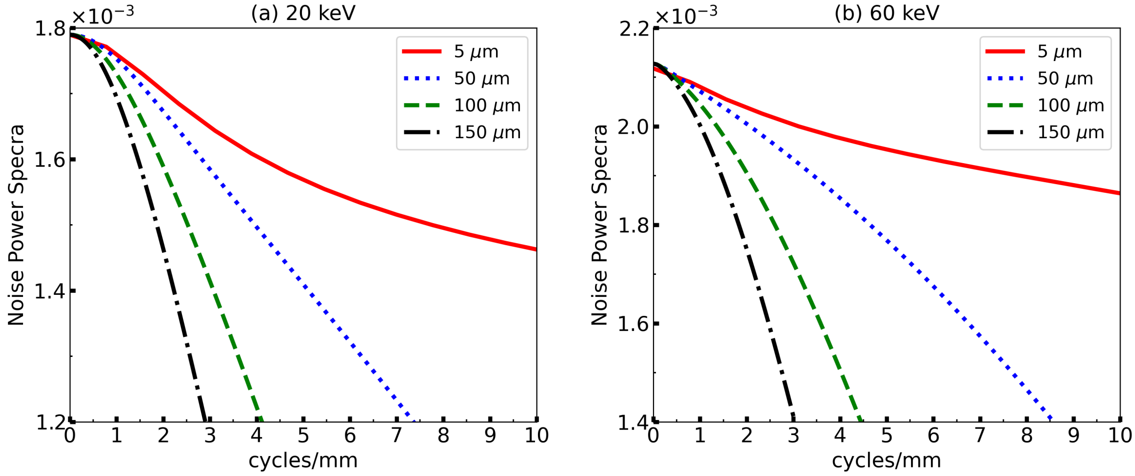

Figure 5.11: *NPS* calculated varying the pixel size from 5 to 150 μm, F = 10 V/μm and two energies (a) 20 keV and (b) 60 keV.

Figure 5.11 shows the *NPS* calculated varying the pixel size from 5 to 150 μm, F = 10 V/μm and two energies (a) 20 keV and (b) 60 keV.

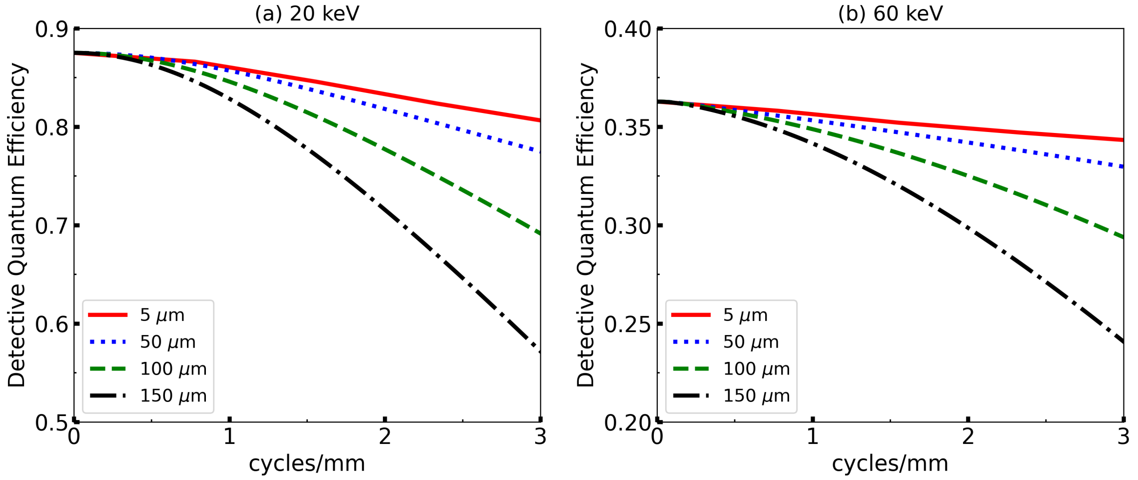

Figure 5.12: *DQE* calculated varying the pixel size from 5 to 150 μm, F = 10 V/μm and two energies (a) 20 keV and (b) 60 keV.

The *NPS* and *DQE* decreases with the pixel size. For the *NPS* this means that the noise increases with the pixel size. This is expected since a larger pixel area results in an increased probability of interaction. For the *DQE*, the lower values for 60 keV is a result of lower efficiency and Swank Factor as the energy increases.

Detector thickness

To quantify the influence of the detector thickness varies, simulations were performed with an a-Se detector with a pixel size of 50 μm and two thicknesses of 150 and 500 μm, the first being usually used in mammography and the second on chest radiography [2]. Figure 5.13 shows the (a) η and (b) Swank factor as a function of energy.

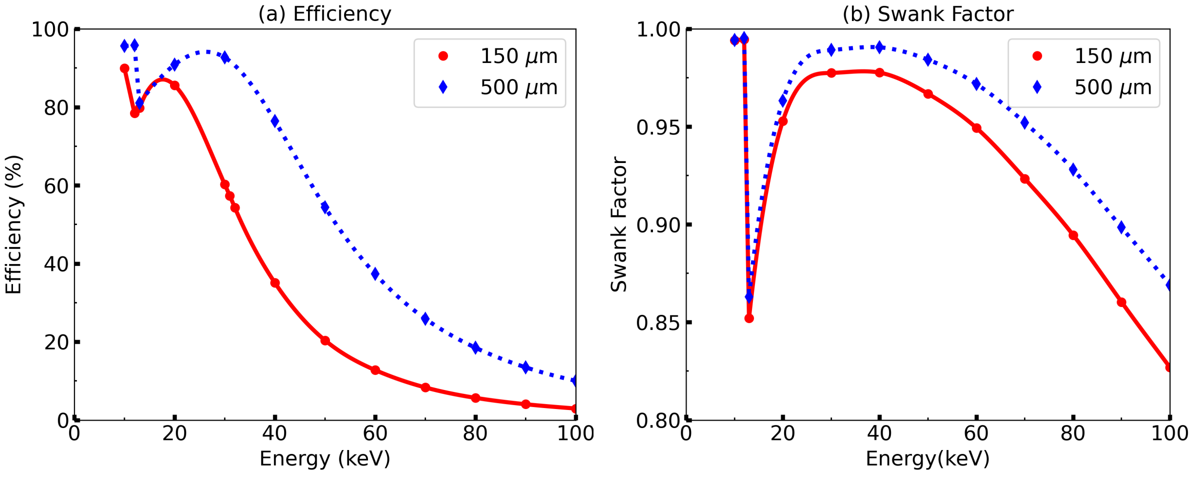

Figure 5.13: (a) η and (b) Swank Factor for a-Se detectors with 150 and 500 μm thicknesses, F = 10 V/μm.

For both cases, the values are larger for the 500 μm thick detector. This increase is more observed for the η, up to 70.7% increase between the thicknesses, for the Swank Factor the difference is only up to 6.3%. The probability of interaction increases with the thickness, resulting in an increase on η, and with more interactions, the energy resolution also increases resulting in larger values for the Swank Factor.

Figure 5.14 shows the (a) MTF and (b) DQE for a-Se detectors with 150 and 500 μm thickness, F = 10 V/μm and two energies : 20 and 60 keV.

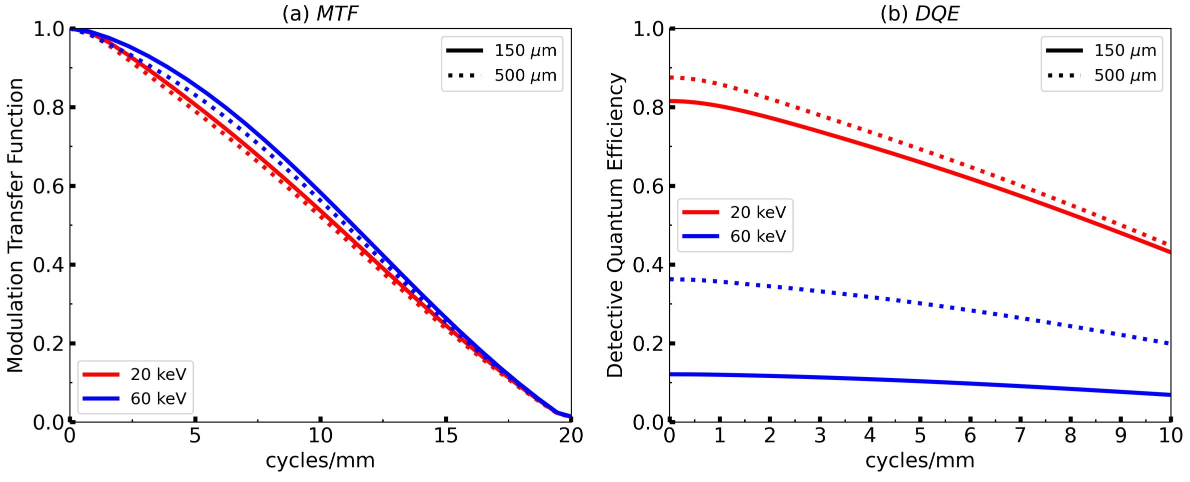

Figure 5.14: (a) MTF and (b) DQE for a-Se detectors with 150 and 500 μm thickness, F = 10 V/μm and two energies : 20 and 60 keV.

The MTF decreased with the detector thickness, showing that the spatial resolution is larger for thinner detectors. A thicker detector results in an increased possibility of lateral spread of particles, therefore, decreasing the spatial resolution. On the other hand, the *DQE* (Figure 5.14 (b)) is larger for the thicker detector due to the increase of η and Swank Factor with the detector thickness.

Applied electric field

The η and Swank Factor for different values of F are present in Figure 5.15 (a) and (b) respectively. a-Se detectors with 500 μm thickness and 50μm pixel values were used for these results.

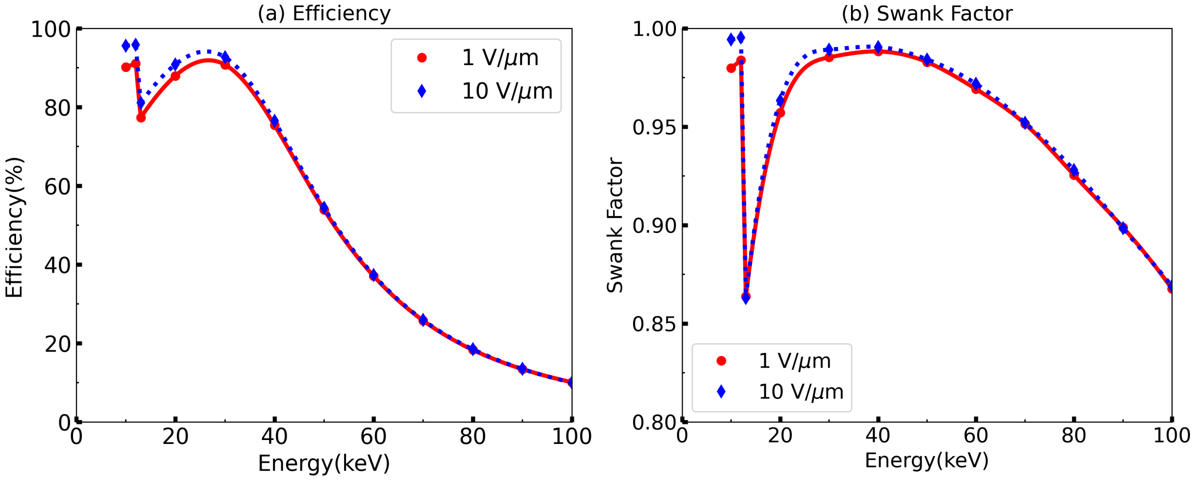

Figure 5.15: (a) Efficiency and (b) Swank Factor for a-Se detectors with 500 μm thickness, $F = 1$ and 10 V/μm.

Differently of the detector thickness, altering the value of F from 1 to 10 V/μm has little effect on η and Swank factor, with relative differences up to 6% and 1.5% respectively. A larger difference was observed for η because of the $W_{\pm}$ decreasing with F (equation 4.2). Therefore, increasing the number of *EHP* created in each interaction.

Figure 5.16 shows the (a) *LSF* and (b) *MTF* obtained varying F, a-Se detectors with 500 μm thickness and 50 μm pixel.

The spatial resolution increases with F which is expected since the bias yields in the *EHP* moving more linearly. For F = 0.1 V/μm, the random thermal movement is more relevant than the case for F = 1 and 10 V/μm.

Figure 5.17 shows the (a) *NPS* and (b) *DQE* obtained varying F, a-Se detectors with 500 μm thickness and 50 μm pixel.

The *NPS* decreases with F, this is because of the variable value of $W_{\pm}$, similar to η. Even though the *MTF* decreases with F, the *DQE* increases because of the η and *NPS*.

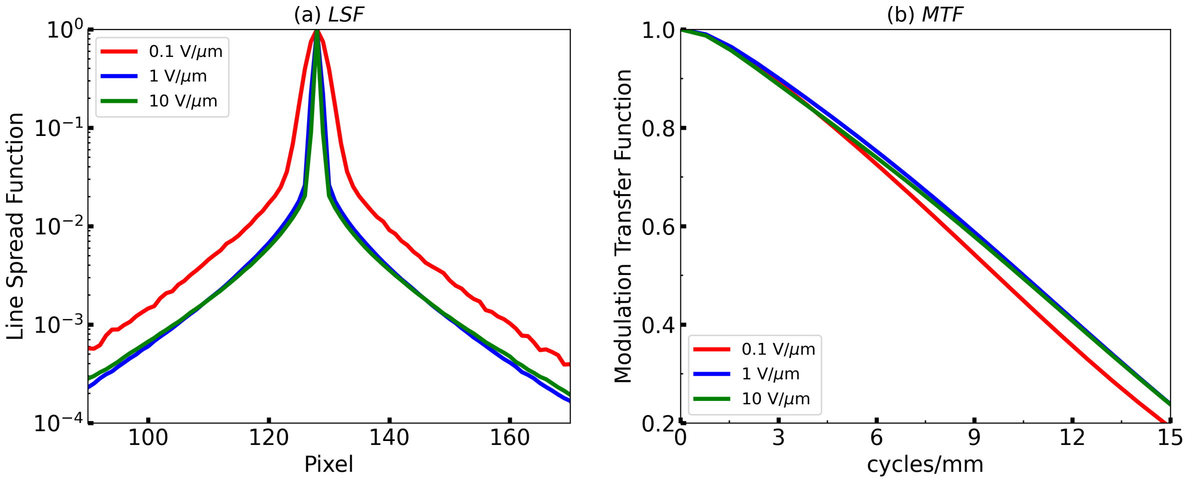

Figure 5.16: (a) *LSF* and (b) *MTF* for a-Se detectors with 500 μm thickness, 50 μm pixel and varying F.

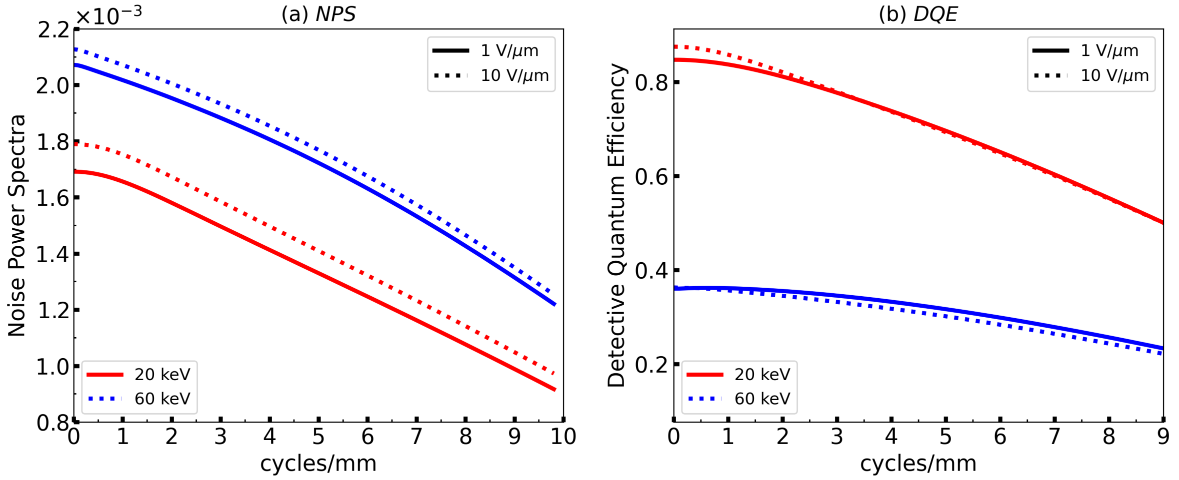

Figure 5.17: (a) *NPS* and (b) *DQE* for a-Se detectors with 500 μm thickness, 50 μm pixel and varying F.

Detector materials

In order to quantify the differences by changing the detector material simulations were performed with a-Se, HgI_2 and PbI_2. Figure 5.18 shows η for (a) a-Se, (b) HgI_2, (c) PbI_2 varying the initial energy between 10-140 keV and the detector thickness between 200 and 1000 μm.

The contour plots show that the detector efficiency increases with the thickness and decreases with the beam energy. Moreover, the a-Se detector presents the lowest efficiency values compared to HgI_2 and PbI_2. This is because Se has a low atomic number compared to I, Hg and Pb. The efficiency presents discontinuity regions for the energies right above the K-edge of the detector materials, which are 12.658, 33.169, 83.102, 88 keV for Se, I, Hg and Pb, respectively [70]. Since the average energy of the X-ray spectra used in thorax radiology is around 40-70 keV, the increase in efficiency right above 40 keV

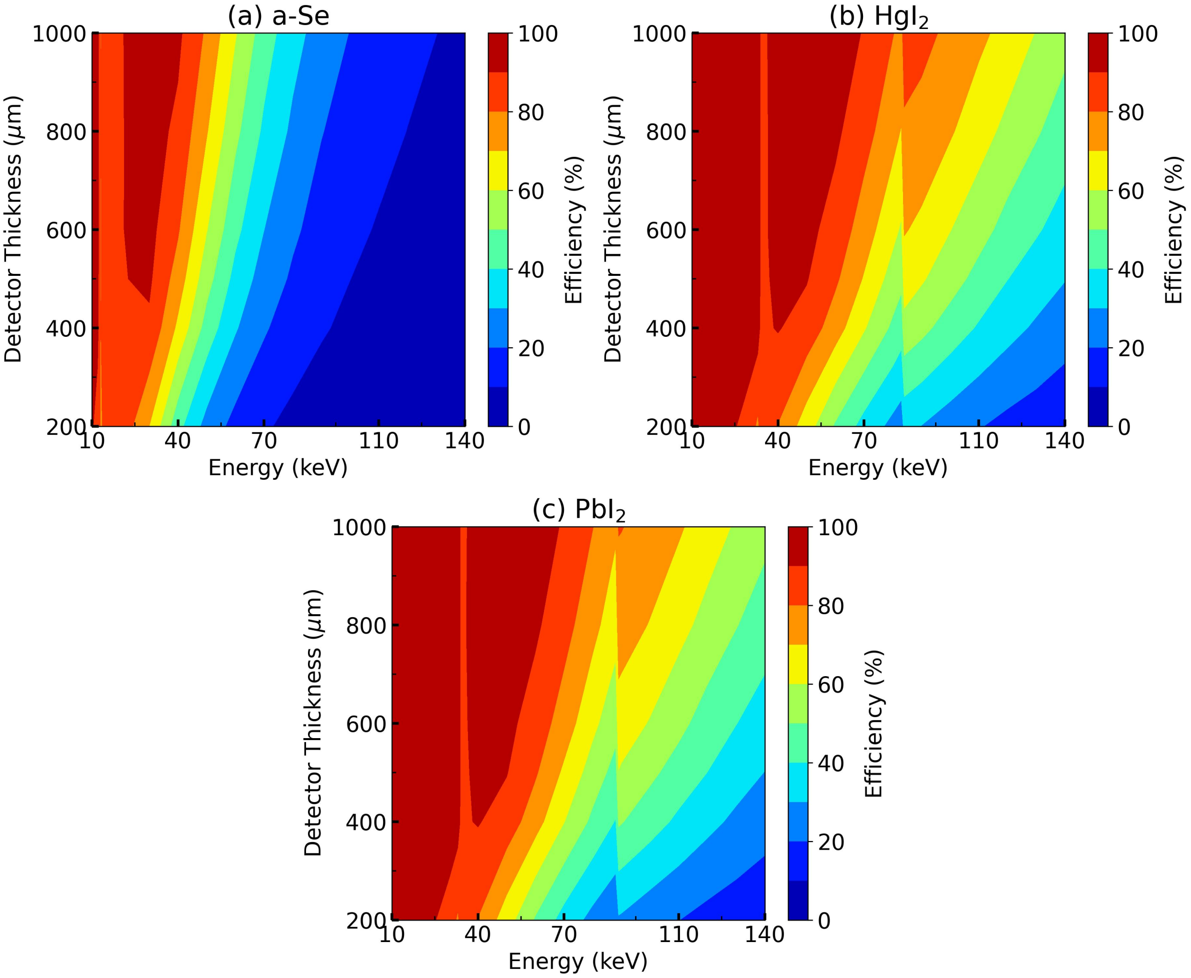

Figure 5.18: Efficiency contour plot simulated for (a) a-Se, (b) HgI$_2$ and (c) PbI$_2$ varying the initial energy between 10-140 keV and the detector thickness between 200 and 1000 μm.

for HgI$_2$ and PbI$_2$ shows a good advantage for these materials. On the other hand, the increase in efficiency right above 20 keV and a great decrease after shows why a-Se is indicated only in mammography.

Figure 5.19 shows the Swank Factor for a-Se, HgI$_2$ and PbI$_2$ varying the initial energy between 10-140 keV and the detector thickness equal to (a) 200 and (b) 500 μm.

The Swank Factor increases with the detector thickness, as shown in Figure 5.13 (b). Moreover, each material has a higher value for the Swank Factor in different energy values, but no material has an overall superior response.

Figure 5.20 shows the MTF calculated for the a-Se, HgI$_2$ and PbI$_2$ detectors for (a) 20, (b) 60 and (c) 100 keV. In all cases, the applied electric field was 0.5 V/μm. The *sinc* function was included for comparison with an ideal case of the function:

$$sinc(f\pi a_{dec}) = \frac{sin(f\pi a_{dec})}{f\pi a_{dec}}, \tag{5.7}$$

were f is the spatial frequency and a_{dec} is the pixel size, which is 100 μm.

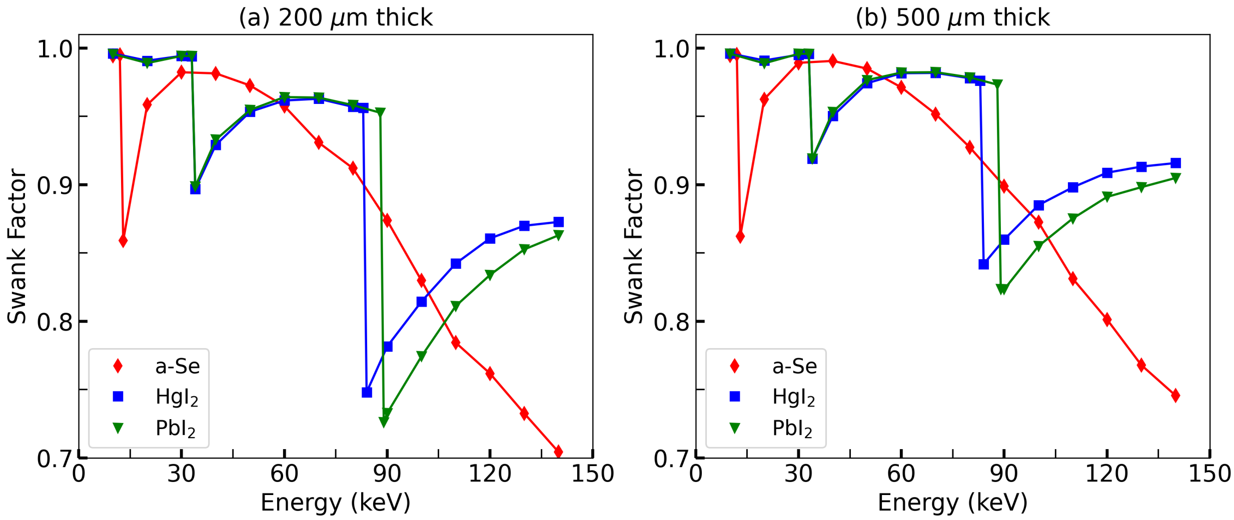

Figure 5.19: Swank Factor for the detector materials a-Se, HgI_2 and PbI_2 varying the initial energy between 10-140 keV and the detector thickness equal to (a) 200 and (b) 500 μm.

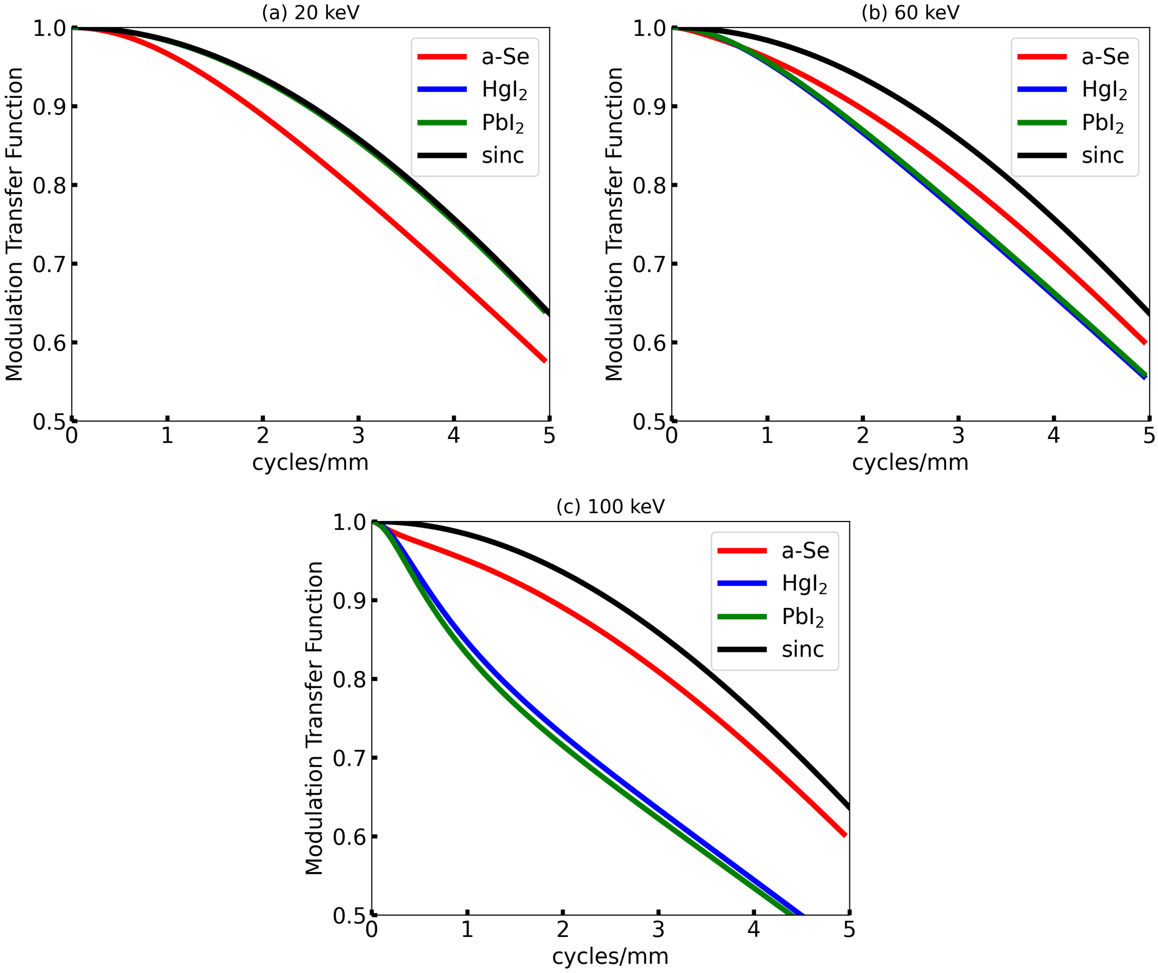

Figure 5.20: *MTF* calculated for the a-Se, HgI_2, and PbI_2 detectors for (a) 20, (b) 60, and (c) 100 keV. In all cases the applied electric field was 0.5 V/μm.

For 20 keV, the a-Se has the lowest spatial resolution, on the other hand, for 60 and 100 keV it has the highest compared to PbI_2 and HgI2. This is because 60 keV is close to the K-edge I and 100 keV is close to the K-edge for Hg and Pb. As shown in 5.3 the spatial resolution decreases for energies close to the K-edge because of the fluorescence.

5.3.2 Photon Counting

Figure 5.21 shows the *PSF* for (a) Si, (b) CdTe, and (c) GaAs detectors with 60 keV incident energy, *ethr* equal to 1 keV and detector thickness equal to 1000 μm.

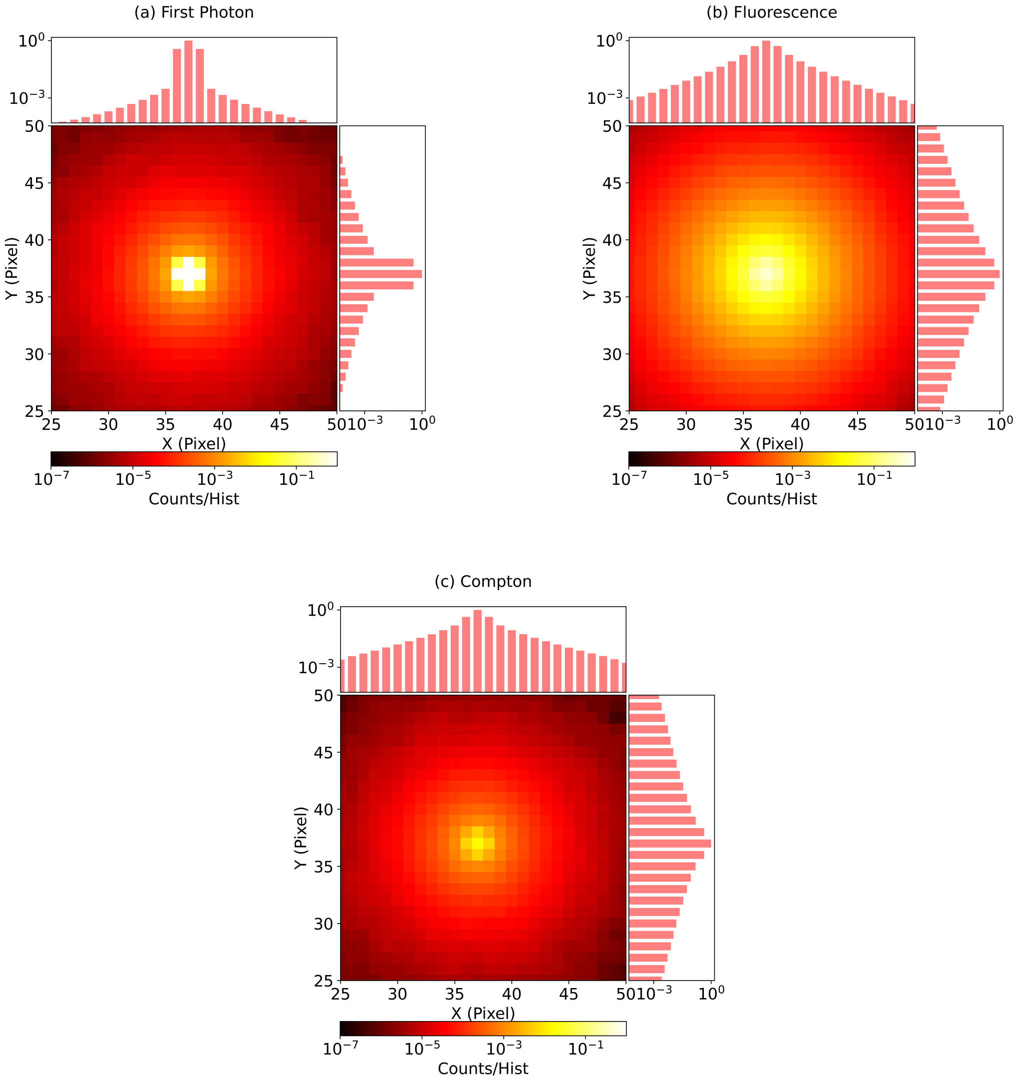

Figure 5.21: Simulated *PSF* for CdTe detector considering the contribution of (a) only the primary photon, (b) fluorescence photons, and (c) photons after Compton scattering. The applied bias was 0.1 V/μm, for all cases a pencil beam of 60 keV was used and the energy threshold (*ethr*) equals 1 keV and detector thickness was 1000 μm.

Similarly, with the EI detector, there is an increase in the spread as the photon energy increases. For all energies, Compton scattering has the lowest percentage of the total number of photons counted. However, its influence increases with the energy because of the interaction probability increase. The 32 keV energy is just above the tellurium K-edge, and consequently, the fluorescence is the most relevant among the cases studied. In the 10 keV case, the fluorescence is present due to the Lα and Lβ emissions [70]. For 32 and 100 keV, the fluorescence *PSF* is wider, even for the latter, where the first photon had the highest photon count. Therefore, the presence of fluorescence results in two problems for photon counting detectors: the possibility of double count and the detector spatial resolution decrease.

Figure 5.22 shows the *LSF* for (a) Si, (b) CdTe, and (c) GaAs detectors with 60 keV incident energy, *ethr* equal to 1 keV and detector thickness equal to 1000 μm.

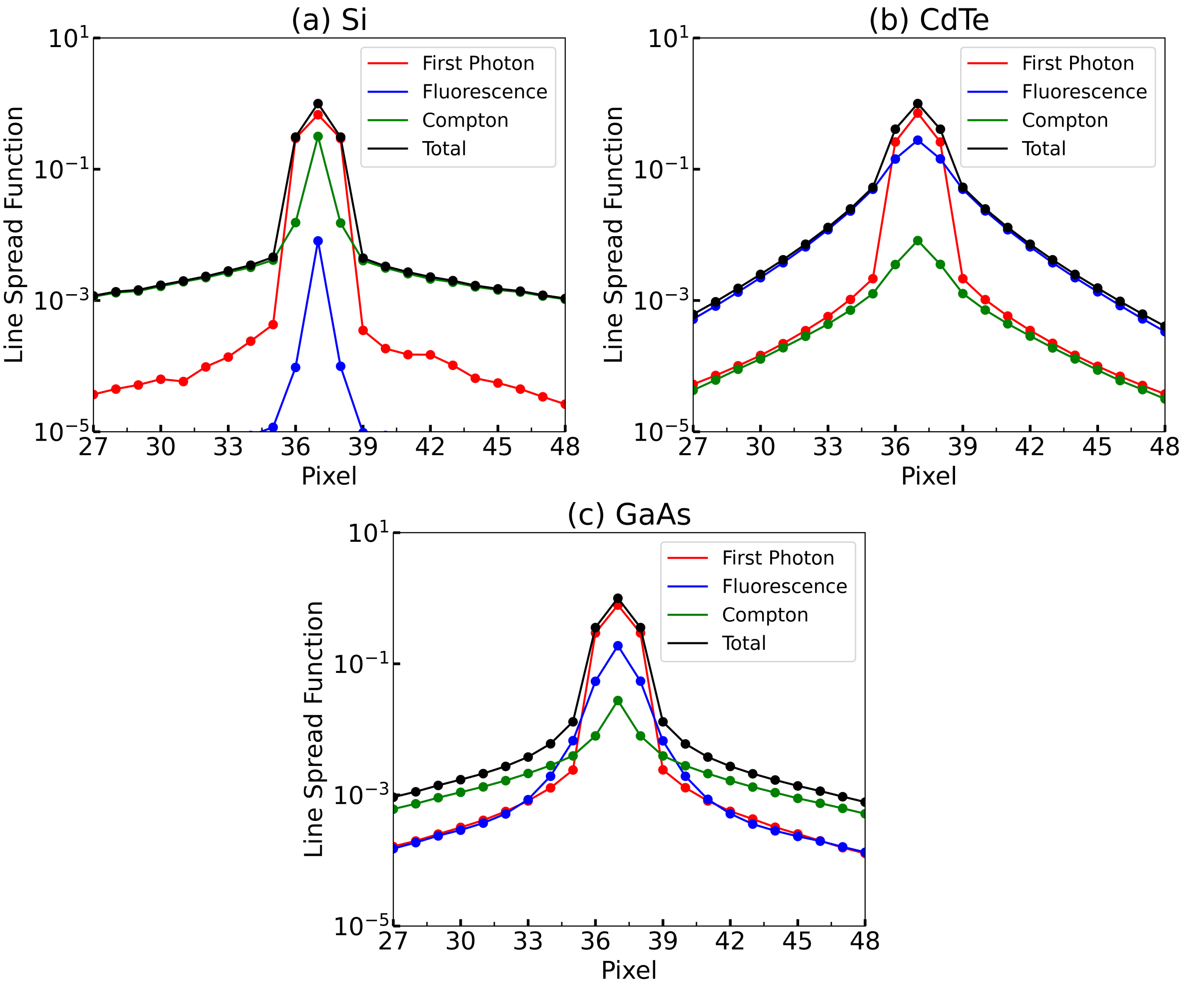

Figure 5.22: Simulated line spread function (*LSF*) for (a) Si, (b) CdTe, and (c) GaAs detector with 60 keV incident energy, *ethr* equal to 1 keV and detector thickness equal to 1000 μm.

For all cases, the primary photon has the greatest influence in the overall *LSF*, followed by the Compton scattering for Si, and florescence for CdTe and GaAs. The K-edge for Cd, Te, Ga and As are one order of magnitude larger than the K-edge for Si resulting in the fluorescence being more influent for these materials. Moreover, the Compton scattering has a relatively higher cross section for lower atomic number materials.

To analyze the impact of the *ethr* values on the detector response, Figure 5.23 shows the *LSF* for 100 keV with *ethr* equal to 1, 10, 32, and 50 keV. The bias was 0.1 V/μm and the detector thickness was 1000 μm.

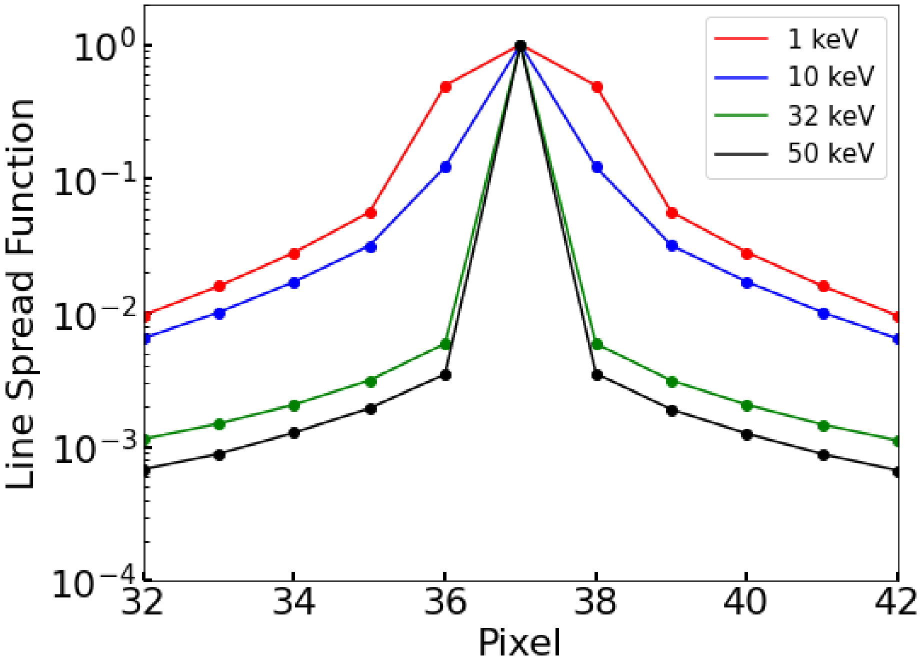

Figure 5.23: Photon counting detector's *LSF* for 100 keV and *ethr* varying from 1 to 50 keV. The applied bias was 0.1 V/μm, and the detector thickness was 1000 μm.

The *LSF* is narrower as the *ethr* increases, especially after the energy of 32 keV, which guarantees that no fluorescence photons are present, and as shown in Figure 5.23, the fluorescence photons have the widest detector response. This result shows that an increase in *ethr* results in a resolution increase. However, the number of photons counted decreases. When *ethr* = 1 keV the central pixel, value (sigma), is 0.8593(0.0003) photons counts per history, while the value decreases to 0.331(0.007) for *ethr* = 50 keV. The increase in the uncertainty also shows that the noise increases with the *ethr*.

Chapter 6

Impact of detailed detector simulation on optimization

This chapter focuses on the impact of detailed detector simulation on image acquisition and optimization via Figure of Merit (*FOM*). This metric balances dose and image quality, therefore this chapter's first section contains the simulation geometry and acquisition parameters. Moreover, it includes the methodology to quantify dose and image quality. The quantity evaluated and how the detailed detector simulation affects the *FOM*.

6.1 Simulation methods

The simulation is divided into two steps: (i) simulation of X-ray interaction with the phantom simulating a chest and (ii) the interaction with the detector, including the creation and transport of *EHP*. The MC code PENELOPE v. 2014 [37] with the penEasy v. 2015 [42] were used in the first step, and the THOR code described in Chapter 4 was used in the second step.

6.1.1 Simulation geometry

Figure 6.1 (a) shows an illustration of the simulation geometry, which consists of an X-ray source with a punctual focal spot located 100 cm above the detector and aligned with the center of the phantom. The field area was 20×20 cm^2 at the phantom surface. The phantom represents a newborn chest and consists of a homogeneous box composed of soft tissue with an area of 20×20 cm^2 and 10 cm thick [6, 13]. Steps with area 3×3 cm^2 were included inside the phantom as contrasting details, and their composition (thickness) were aluminum (0.5 cm), calcium (0.5 cm), and Teflon (2 cm). The aluminum represents bone and calcium was included to represent calcification on lungs (a common marker for pneumonia), Teflon was included to represent low contrast structures. All contrasting structures were positioned close to the detector side, 1 cm from the phantom base. Additionally, a $2.5 \times 3.8 \times 2.5$ cm^3 air volume, representing an ionization chamber, was included immediately above the phantom surface. The phantom rested on a 3 cm thick carbon fiber table. Two types of detectors with an area of 20×20 cm^2 were evaluated: EI and PC detectors. The THOR code was used to simulate the process of detection in semiconductors (more details in Chapter 4). The EI detector was composed of a-Se and was 500 μm thick. The $W_{\pm}$ was calculated using Equation 4.2 present in the Section 4.2.1, the Fano Factor was equal to 0.059, and $F = 10$ V/μm [62]. The PC detector was composed of CdTe, with 1000 μm thick. In this case, $W_{\pm} = 4.43$ eV, Fano Factor $= 0.15$, $F = 0.1$ V/μm [62]. All simulations were performed with a negative F and collecting only electrons. Six 3×3 cm^2 regions of interest (*ROIs*) were defined to quantify the image quality. *ROIs* 1 to 3 represent the contrasting objects, while *ROIs* 4 to 6 represent the background. Figure 6.1 (b) illustrates the detector x-y view in Gview 2D software (built-in PENELOPE 2014 [37]), showing the regions of interest in the detector.

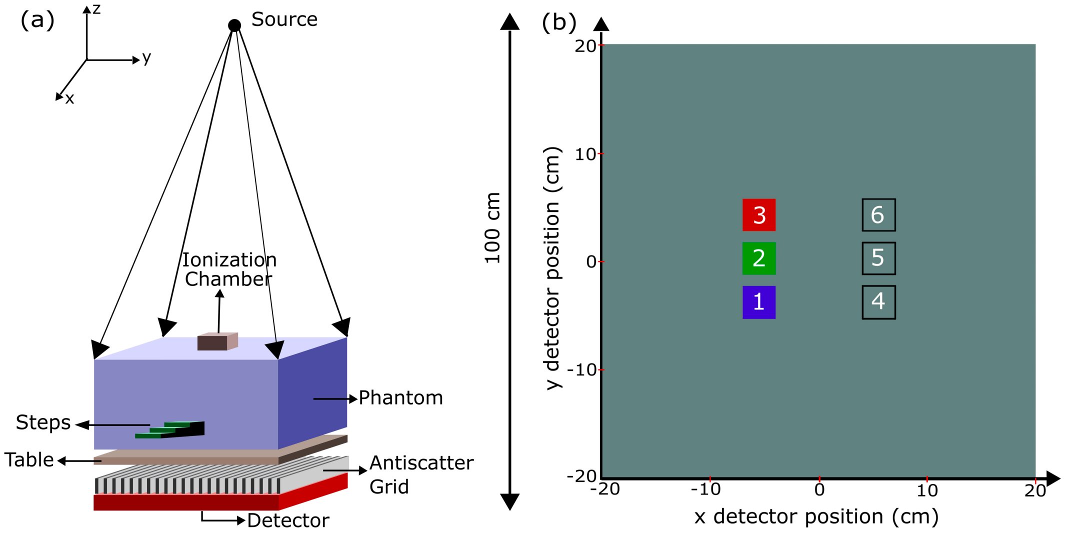

Figure 6.1: (a) Geometry of the chest radiography simulation including the radiation source, ionization chamber, phantom, table, and detector. (b) Detector illustration showing the regions of interest (*ROI*s). *ROI*s 1 to 3 represent the 1.5, 1.0, and 0.5 cm Al steps, respectively, and *ROI*s 4 to 6 were used to calculate the corresponding background signal. .

The X-ray polyenergetic beams were generated using the SpekCalc software [128], considering a tungsten target with a 15° tilt angle, tube potentials varying from 40 to 120 kV, and an intrinsic Al filtration of 3mm plus 0.8 mm beryllium.

6.1.2 Dosimetry

The dosimetric quantities used in this work were the incident air kerma (K_{ar}) and the mean absorbed dose (MAD), which were obtained using the "Tally Energy Deposition" present on penEasy v. 2015. This tally computes the energy deposited per history in each material. To simulate MAD and K_{ar} simultaneously a new Tally was created based on the ”Tally Energy Deposition”, being named “Tally Energy deposited by primary particle”. The uncertainty of the dosimetric quantities was always less than 1%, requiring a number of histories in the order of 10^8.

Air kerma (K_{ar}) - units of Gy/History - is determined from indirect simulation results. The K_{air} was calculated as the ratio between the energy deposited by primary particles (E^p_{air}) in the ionization chamber, obtained using “Tally Energy deposited by the primary particle”, and the mass of the ionization chamber (m_{ar}):

$$K_{ar} = \frac{E^p_{ar}}{m_{ar}}. \tag{6.1}$$

Mean Absorbed Dose in the phantom (MAD) - units of Gy/History - was determined indirectly with simulation results. MAD is the dose deposited in the entire phantom and was calculated as the ratio between the energy absorbed in the phantom (E_o), obtained using “Tally Energy Deposition”, and the mass of the phantom (m_o), calculated from geometric data:

$$MAD = \frac{E_o}{m_o}. \tag{6.2}$$

Dose-Kerma ratio (k-MAD) - was defined as the ration between MAD and K_{ar}. This quantity is usually expressed in the unit Gy/Gy.

Validations were performed for the dosimetric quantities. The MAD was compared against the data presented in the AAPM Report 195, Case 2: Radiography and Body Tomosynthesis [116] (see Appendix B). The tally “Energy deposited by the primary particle” included in the penEasy code was validated by performing simulations with and without the phantom and calculating the K_{ar} (see Appendix C).

6.1.3 Image quality

The simulated images consist of 2D matrices with 1000 rows and columns where in the EI mode each element of the matrix (e) corresponds to the energy deposited in a pixel, on the other hand, in the PC mode, e is the number of photons detected. For both cases are normalized by the number of histories.

Before quantifying the image quality, the flat field processing was performed which cancels the effects of image artifacts caused by variations in the pixel-to-pixel sensitivity of the detector and by distortions in the X-ray path. For instance, because of the field divergence and scattering, the number of X-rays reaching the detector center is larger than the edges. Therefore, a correction is needed to normalize the signal in the detector. This process consists of simulating images without the contrasting details and obtaining a matrix where each term is calculated as:

$$a_{ij} = e_{ij}/e_{max}, \tag{6.3}$$

where i and j represents the row and column of the matrix and m_{max} is the maximum value in the matrix simulated. This flat field matrix is multiplied by the matrix representing the radiographic.

The contrast (C), signal-to-noise ratio (*SNR*) and contrast-to-noise ratio (*CNR*) was used to quantify image quality. In this work, the contrast was calculated as:

$$C = \frac{S_N - S_O}{S_N}, \tag{6.4}$$

where S_N and S_O represent the signal referring to a background region and an object, respectively. For the EI detector, the signal is the mean energy deposited in the pixels inside the *ROI*s in Figure 6.1. On the other hand, for the PC detector, the signal is the mean number of photons counted in pixels inside the *ROIs*.

SNR quantifies the noise present in the image, based on the ratio between the average signal of a structure (S) and its respective standard deviation (σ), as defined by:

$$SNR = \frac{S}{\sigma}. \tag{6.5}$$

The *SNR* is a quantity that compares the desired signal level with the background noise level, the higher the *SNR*, the smaller the effect that the noise has on the image visualization [2].

The *CNR* evaluates the relationship between image contrast and relative noise, and it can be considered a quantity that optimizes image quality. *CNR* is defined as:

$$CNR = \frac{S_N - S_O}{\sigma}. \tag{6.6}$$

CNR is not affected by image processing, thus being a more relevant quantity to describe the visualization of different structures in a digital image [2]. The *SNR* and *CNR* obtained by the equations 6.5 and 6.6 depends on the number of initial photons, as the uncertainty in Monte Carlo simulations decreases with the histories. To be independent of the beam intensity SNR and CNR were normalized by K_{ar}:

$$SNR_n = \frac{SNR}{\sqrt{K_{ar}}} \tag{6.7}$$

$$CNR_n = \frac{CNR}{\sqrt{K_{ar}}} \tag{6.8}$$

6.1.4 Figure of merit

FOM was used to determine the optimal tube potential and additional filtration for each phantom thickness as:

$$FOM = \frac{CNR^2}{MAD}. \tag{6.9}$$

The optimal exposure conditions were determined as those that produce the highest FOM values, which are associated with the best performance in terms of dose reduction and/or image quality improvement. The tube potential interval in which the FOM is maximum, with variations less than 5%, was defined as the interval optimum tube potential [35].

The FOM ratio between two spectra (r $= FOM_{comp}/FOM_{ref}$) was used to compare different exposure parameters. Since, if r $<$ 1, the compared spectrum ($comp$) has a worse performance than the reference spectrum (ref). If r $>$ 1, there is a gain in image quality by a factor of $\sqrt{r}$ for constant dose or a decrease in dose by a factor of r^{-1} for constant image quality. In this study, the *ref* spectrum was 60 kV with no added filtration, i.e., the indicated by the American College of Radiology for newborns [129].

6.2 Results

6.2.1 Impact on image formation

Figure 6.2 (a) shows the flat field matrix, (b) and (c) show, respectively, the 40 kV image in the EI mode before and after the correction using the flat field.

Before the correction, the edges were in darker shades of gray than the steps, showing that the geometry simulation introduces a contrast that is as influential as the contrast between the background and the steps. With the flat field correction, the steps are more evident, resulting in a larger contrast. In fact, the contrast between the middle step and the background increases from 9 to 15% after the flat field.

To evaluate the detailed detector simulation impact on the image noise, a *ROI* was delimited on Figure 6.2 in the region where the aluminum steps are not present. The ROI has an area of 8×8 cm^2, Figure 6.3 shows a histogram of the pixel value for the a-Se 40 kV with and without the flat field. The pixel value was standardized into the interval

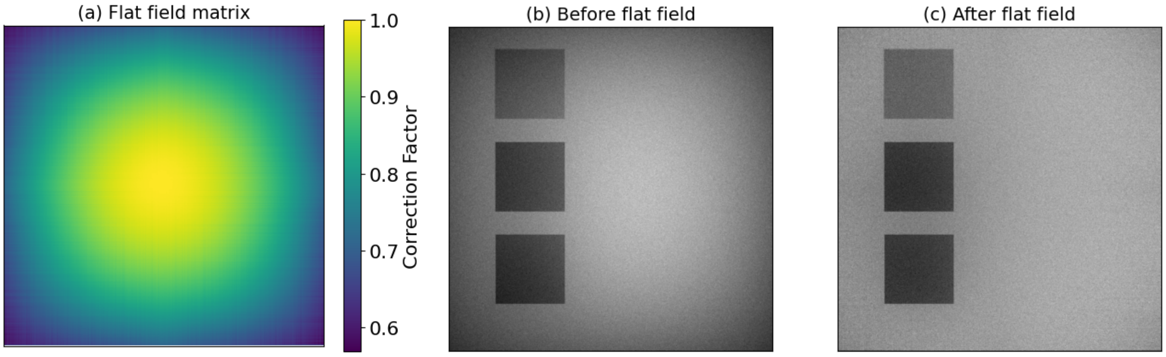

Figure 6.2: (a) Flat field matrix, 40 kV image in the EI mode (b) before and (c) after the correction using the flat field.

between 0 and 4096 to represent a 12-bit image.

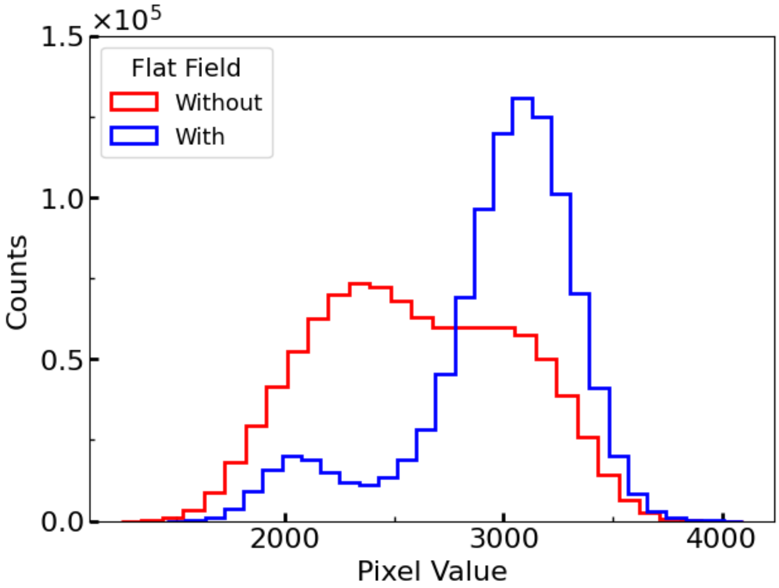

Figure 6.3: Histogram of the pixel value for the a-Se 40 kV case with and without the flat field.

The shape of the histogram changes after the flat field correction. Before, the histogram had a lower height and larger distribution, while after the correction two peaks are present, one with more counts and thinner and a second smaller. The peak with more counts is corespondent to the background regions and the lower peak is correspondent to the steps. Consequently, the flat field correction enhanced the differences between the steps and the background.

To compare the images with (THOR) and without (PENELOPE) the charge dispersion, Figure 6.4 shows the simulated image for 40 kV and a-Se detector (a) only using the PENELOPE code, (b) with the *EHP* creation and transport (THOR code) and the (c) logarithmic difference between them.

Visually there is little difference between the PENELOPE and THOR codes.

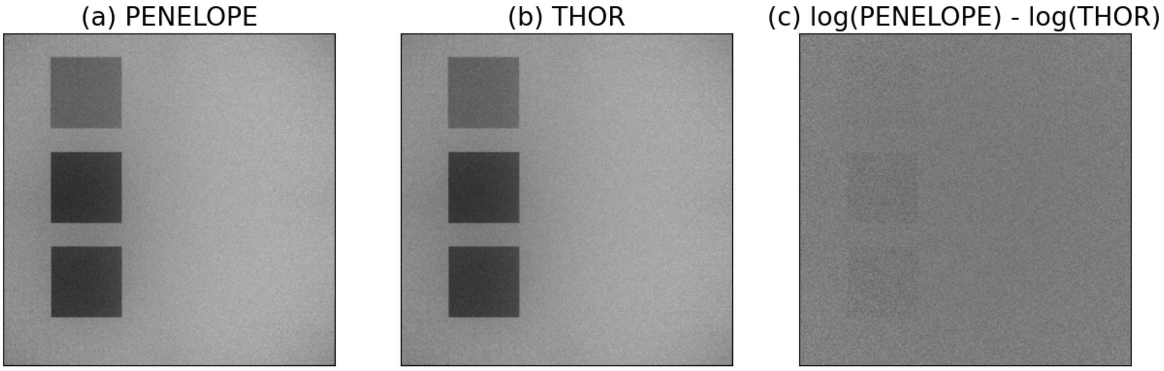

Figure 6.4: Simulated image for 40 kV and a-Se detector (a) only using the PENELOPE code, (b) with the *EHP* creation and transport (THOR code) and the (c) logarithmic difference between them.

However, the log difference depicted in Figure 6.4 (c) evidences the larger differences in the steps region. To show the impact of *EHP* transport on the histogram, Figure 6.5 shows the histogram for (a) the a-Se and (b) the CdTe detectors obtained with the PENELOPE and THOR codes, both cases are for 40 kV.

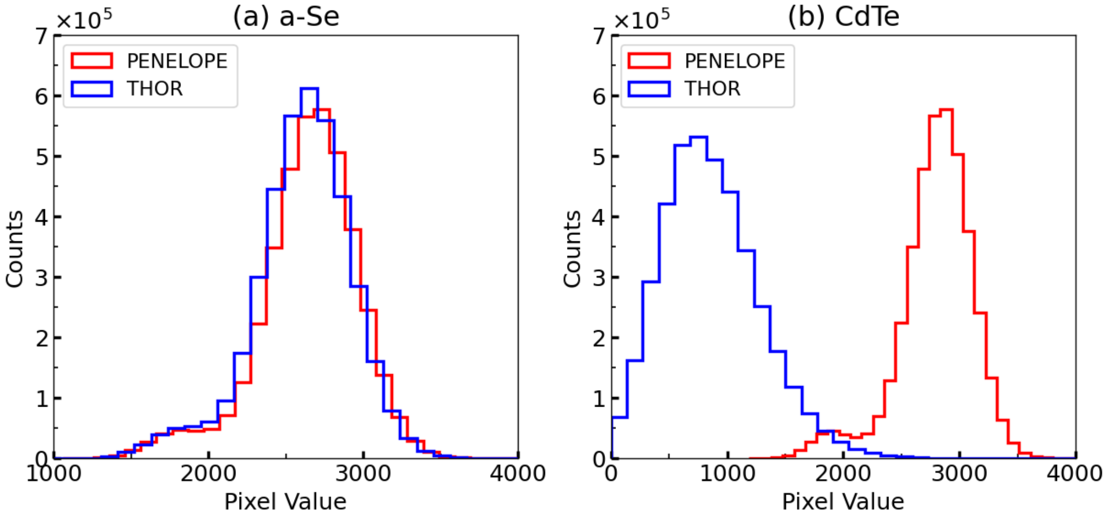

Figure 6.5: Histogram of the pixel value for (a) the a-Se and (b) the CdTe detectors with and without the charge dispersion, both cases are for 40 kV.

For the a-Se detector, the THOR code has slightly lower pixel values, but the histogram shape is similar. On the other hand, for the CdTe case, the histograms are completely different, with the THOR code having lower pixel values. The reason for the greater difference in the codes was the separation between primary, Compton, and fluorescence photons in the THOR code. This is a great limitation of the PENELOPE code, since the charge sharing between pixels, caused especially by fluorescence photons, is a major factor in limiting the spatial and energy resolution in PC detectors [31]. Therefore, there is an overestimation of these quantities by using the PENELOPE code only.

Figure 6.6 shows the plot profile in the steps region for the 40 kV image in an a-Se detector with and without the charge dispersion. In this case, to better visualize the differences, no normalization was performed. The case without dispersion has a lower signal (counts/history) which is expected, since the detailed simulation of *EHP* results in loss of signal. Moreover, the regions between the steps are smothered with the dispersion, showing a decrease in spatial resolution.

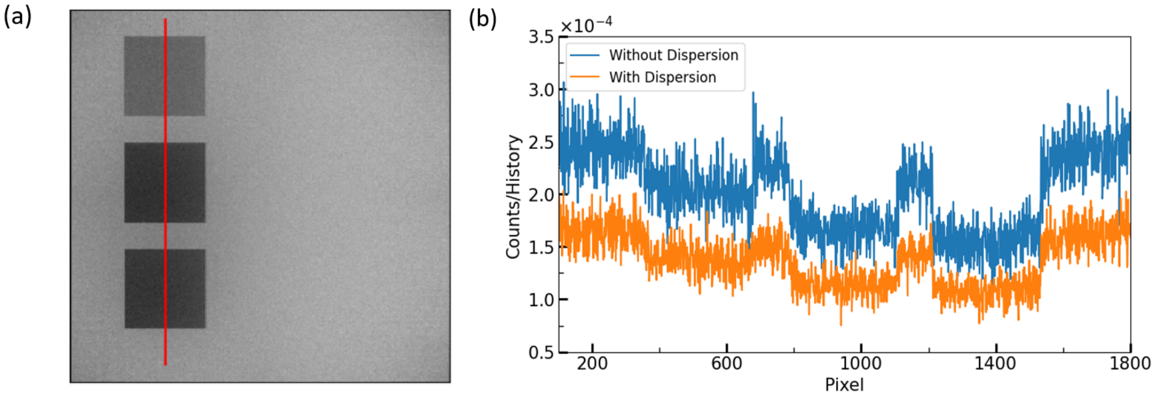

Figure 6.6: (a) Radiographic image produced with 40 kV tube potential without the charge dispersion. (b) Plot profile of the radiographic image in the steps region (red line on (a)) with and without the charge dispersion.

Figure 6.7 (a) shows the contrast as a function of the tube potential for the a-Se and CdTe detectors, with and without the charge dispersion. The relative difference between the contrast without (PENELOPE code) and with (THOR code) the charge dispersion models are shown in Figure 6.7 (b). The energy threshold for the PC detector was 1 keV.

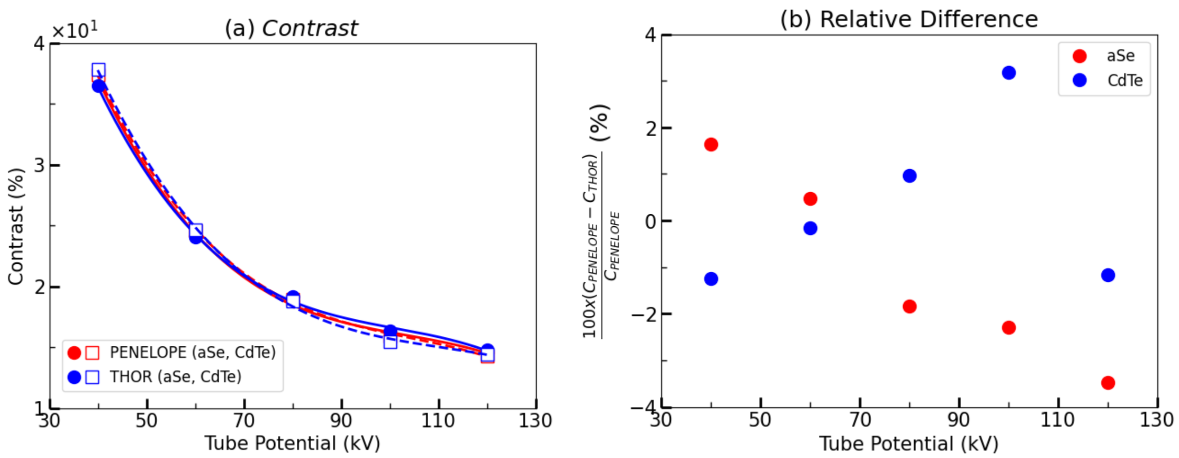

Figure 6.7: (a) Contrast as a function of the tube potential for the a-Se and CdTe detectors, with and without the charge dispersion. (b) The relative difference between the contrast without (PENELOPE) and with (THOR code) the charge dispersion model. The energy threshold for the PC detector was 1 keV.

The PC (CdTe) detectors have higher contrast values than EI (a-Se) detectors.

This is expected since the idea of counting photons is that all photons have the same weight. On the other hand, in EI detectors, high energy photons, i.e., the ones that result in the lowest contrast, have more weight [30]. The relative difference, Figure 6.7 (b), for the EI detector decreases with the tube potential. On the other hand, for the PC detector, the relative difference increases with the tube potential reaching its maximum value at 100 kV and then decreasing as the tube potential increases. The effective energy for the 40 and 100 kV spectra are approximately 26.3 and 33.5 keV, respectively. In addition, the k-edge for the Cd and Te are 26.711 and 31.814 keV [70]. Therefore, the fluorescence is responsible for this increase in contrast to the THOR code, since in the charge dispersion model fluorescence and Compton scattered photons are counted separately from the incident photon, differently from the Tally PID on penEasy [42]. Such separation results in double counts, a problem largely faced in photon counting detectors [30]. This result shows that a detailed simulation for photon counting is fundamental for PC detectors.

Figure 6.8 shows the (a) *nSNR* and (b) *nCNR* for tube potentials between 40 and 120 keV, for the a-Se and CdTe detectors with (THOR code) and without (PENELOPE) the charge dispersion model. The energy threshold for the PC detector was 1 keV.

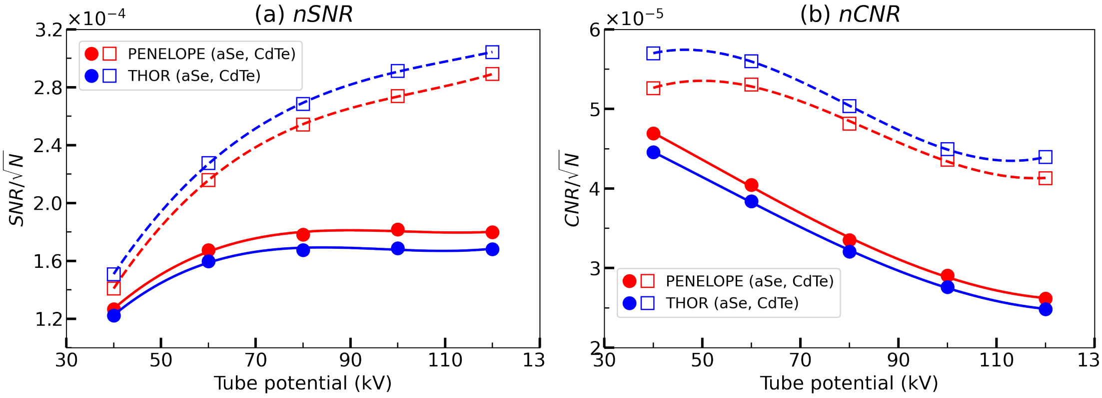

Figure 6.8: (a) *nSNR* and (b) *nCNR* as a function of the tube potential for the a-Se and CdTe detectors, with and without the charge dispersion.

Figure 6.8 (a) and (b) showed that the *nSNR* and *nCNR* have a similar tube potential dependency, and the main difference introduced between the charge dispersion models is the amplitude of these quantities. For the a-Se detector, when charge dispersion is included a decrease in *nSNR* and *nCNR* was observed. The charge dispersion decreases the detector efficiency due to the charge sharing effect observed due to *EHP* dispersion to neighbor pixels, moreover, charge trapping is also a factor. For the CdTe detectors, the results are the opposite, the charge dispersion increases the *nSNR* and *nCNR*. This is because the fluorescence and Compton scattered photons double counts previously cited.

Histogram windowing

Histogram windowing was performed to evaluate the impact of the *EHP* transport in imaging processing techniques commonly used in radiography. Histogram windowing is used to increase contrast, this technique consists of introducing a lower and upper limit in pixel value on the histogram, where all pixel values outside this interval become equal to zero. Figure 6.9 shows an example of histogram windowing for the case of a tube potential of 40 kV obtained with the PENELOPE code. The lower and upper limits were 2000 and 3500, respectively. Figure 6.9 (a) shows the radiographic image before the windowing, (b) after the windowing and (c) shows the histogram of pixel values with the gray area being the interval between the lower and upper pixel value limits.

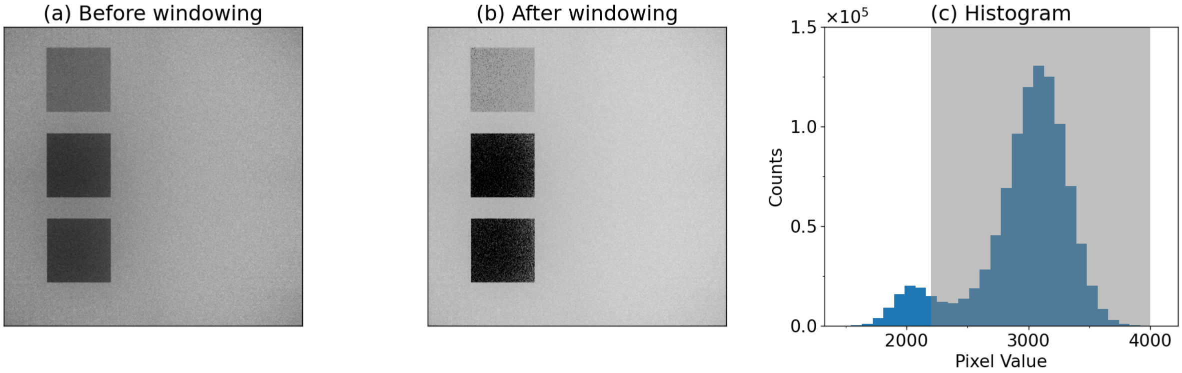

Figure 6.9: (Radiographic image for a tube potential of 40 kV, obtained with the PENELOPE code (a) before and (b) after the histogram windowing. Figure (c) shows the histogram with the gray area representing the interval between the lower (2200) and upper (4000).

Comparing the cases with and without the windowing shown respectively in Figure 6.9 (a) and (b), is possible to qualitatively observe that the contrast increased. Numerically the contrast increased from 19% to 23%. However, there is an increase in the image noise, where the *SNR* decreased from 12.5 to 6.9 after the image processing.

To investigate the impact of window size and position on the image quality, Figure 6.10 shows (a) the contrast, (b) the *SNR* and (c) the *CNR* as the pixel value upper and lower limits vary between 1500-2200 and 3100-3900, respectively. These intervals were chosen because values outside of them resulted in negative contrast, i.e., the pixel value at the steps *ROI* was higher than in the background *ROI*.

Figure 6.10 shows that as the contrast increases, the *SNR* decreases, which was also observed in Figure 6.9. Moreover, a tendency can be observed, where the lower and upper limits are more influential in varying the contrast and *SNR*, respectively. On the other hand, differently of the contrast and *SNR*, the *CNR* is highly dependent on both the lower and upper limits with its highest value occurring at (lower,upper) = (2240,4096) with *CNR* = 5.06, contrast = 52% and *SNR* = 9.7. Maximizing the *CNR* results in the optimal upper and lower limits since the *CNR* evaluates the relation of contrast with noise

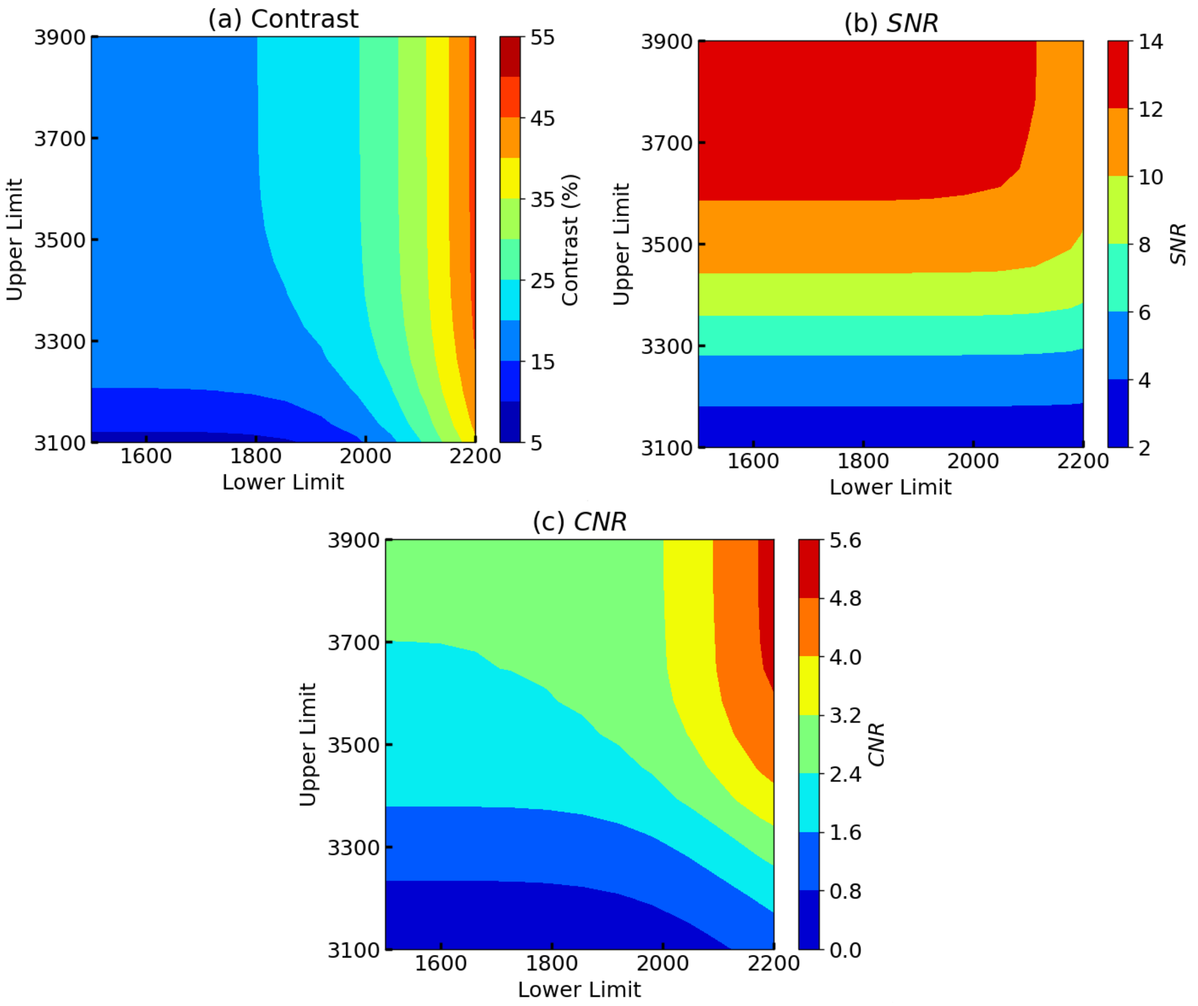

Figure 6.10: Countour plots of the (a) contrast, (b) *SNR* and (c) *CNR* as the pixel value upper and lower limits vary between 1500-2200 and 3100-3900, respectively.

as a metric of optimization of image quality without considering dose. Table 6.1 shows the optimum lower limit for pixel value and the correspondent contrast, *nSNR* and *nCNR* for two tube potentials (40 and 120 kV), the two detector types (a-Se and CdTe) with and without the charge dispersion. For all cases, the optimum upper limit was 4096.

For the a-Se detector, all cases with the THOR code resulted in higher contrast than the PENELOPE code, but the *nSNR* is lower. This is a direct result of a higher noise when the charge dispersion is implemented. On the other hand, for the CdTe, the contrast is always larger with the PENELOPE code. For the CdTe, these differences in results show how the detailed modeling can reduce the image quality.

Optimization

Figure 6.11 shows the normalized FOM/FOM_r as a function of the tube potential for the 10 cm phantom composed of soft tissue, a-Se, and CdTe detectors, with and without (only PENELOPE) the charge dispersion.

Table 6.1: Optimum lower limit for pixel value and the correspondent contrast, *nSNR* and *nCNR* for two tube potentials (40 and 120 kV), the two detector types (a-Se and CdTe) with and without the charge dispersion

kV	Detector	Code	Lower Limit	Contrast (%)	*nSNR*	*nCNR*
40	a-Se	PENELOPE	2240	52.4	6.8×10^{-5}	3.6×10^{-5}
		THOR	2240	56.5	6.0×10^{-5}	3.4×10^{-5}
	CdTe	PENELOPE	2432	63.5	7.6×10^{-5}	4.8×10^{-5}
		THOR	512	25.7	8.7×10^{-4}	2.2×10^{-4}
120	a-Se	PENELOPE	2688	18.9	9.3×10^{-5}	1.8×10^{-5}
		THOR	2560	20.6	7.8×10^{-5}	1.6×10^{-5}
	CdTe	PENELOPE	3072	38.3	1.2×10^{-4}	4.7×10^{-5}
		THOR	768	19.3	2.7×10^{-4}	2.5×10^{-5}

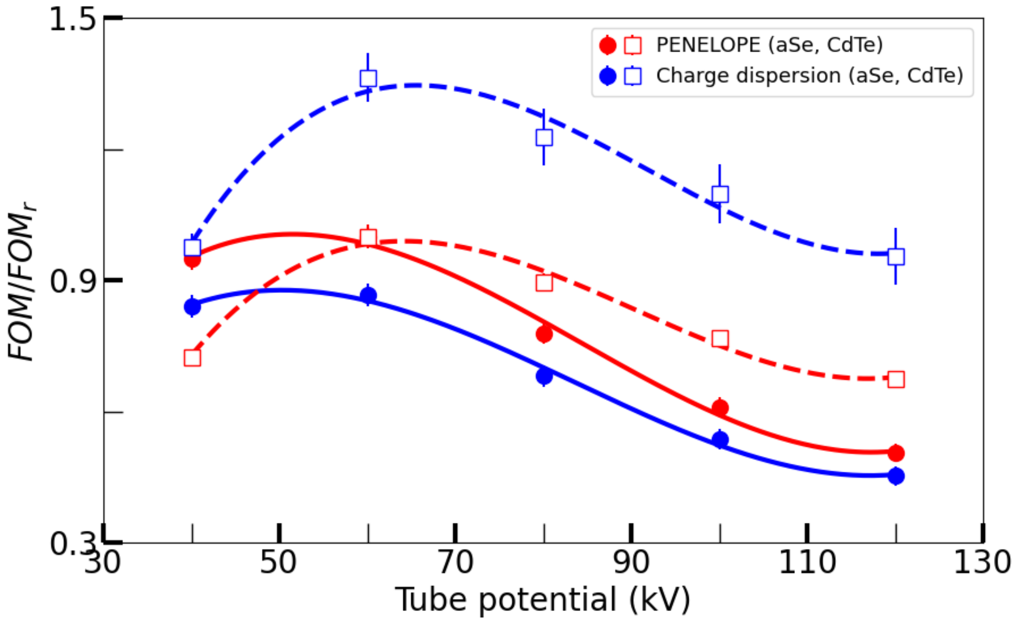

Figure 6.11: FOM/FOM_r as a function of the tube potential for the 10 cm phantom composed of soft tissue, a-Se, and CdTe detectors, with and without the charge dispersion.

The results show that the FOM/FOM_r dependency with the tube potential is similar for the cases with and without the charge dispersion. The optimum tube potential has a difference of up to 5 kV with the charge dispersion. The intersection between the optimum tube potential range with and without the charge dispersion is 40-65 kV and 55-75 kV for the aSe and CdTe detectors, respectively. Using only the PENELOPE code the simulation time is up to 50% less than with the detailed detector modeling.

6.3 Summary

The results from this section show that the detailed simulation of the detection process has an impact on image quality. With the THOR code, it was possible to compare visually radiographic images obtained without and with the charge dispersion. Moreover, quantify the image quality with the contrast, *SNR* and *CNR*, and evaluate the effect of the charge dispersion on the histogram form.

Among the two modes of detection studied, the PC mode using the CdTe as the sensor material showed the largest differences between the PENELOPE and THOR codes. The separation in counting primary, fluorescence and Compton-created photons implemented on the THOR code was the main reason between the codes. Moreover, this separation occurs in real detectors with studies pointing out that the charge sharing between pixels, which in the case of CdTe is caused especially by fluorescence photons, is one the major disadvantages in PC detectors [30, 31]. Therefore, for the PC mode, a more detailed detection simulation is necessary. For the EI mode, the differences between the PENELOPE and THOR codes were more subtle, especially in the histograms. However, for the *SNR* and *CNR* larger differences were observed because of the charge trapping, which is responsible for increasing the image noise.

Finally, for optimization purposes, a detailed detector modeling is not necessary for the cases studied, as the *FOM* dependency with the tube potential remained unchanged when the charge dispersion was implemented for optimization purposes.

Chapter 7

Conclusions

This work focused on the detailed modeling of semiconductor detectors. The code THOR implemented in this work was validated using studies in the literature and the difference between them was lower than the simulation uncertainties showing that the results obtained with the code can be trusted. With the detector characterization in terms of energy and spatial resolution, noise, and efficiency via the quantities Swank Factor, *MTF*, *NPS* and *DQE* it was possible to evaluate the detector's response varying the incident energy, the applied electric field, the sensor's thickness, pixel size and composition. Also, the modes of detection (EI and PC) were explored.

The impact of the detailed simulation of the detection process was the main objective of this work. With the THOR code, it was possible to compare visually radiographic images obtained without and with the charge dispersion. Moreover, quantify the image quality with the contrast, *SNR* and *CNR*, and evaluate the effect of the charge dispersion on the histogram form. The two semiconductors detectors most used in radiology were simulated: a-Se and CdTe [25, 65], and the detector geometry: pixel size, thickness, and applied electric field chosen is the standard for these detectors [29, 30, 60]. The charge dispersion affects the image quality both qualitatively and quantitatively. The a-Se detector presented fewer differences between the PENELEPE and THOR codes, with the image histogram almost identical and differences in contrast, *CNR* and *SNR* below 5%. This is most likely because the a-Se detector has a large electric field 10 V/μm, which limits the charge dispersion. However, it is important to point out, that the inclusion of charge dispersion increases the noise, which occurred because of the increase in losses during the detection process modeled in the THOR code, mainly charge trapping. On the other hand, the CdTe presented large differences between the codes, with a histogram of pixel value concentrated on lower values in the THOR code and at higher values in the PENELOPE code. The contrast also decreased with the inclusion of dispersion of charges, but the *CNR* and *SNR* increased. This is a direct result of THOR code counting separately primary photons and photons originating from Compton scattering and fluorescence. Another factor analyzed in this work was the impact of charge dispersion on the imaging processing techniques usually used: flat field and histogram windowing. The second showed that the THOR code results in lower contrast improvement compared to the PENELOPE code.

For optimization purposes, when the charge dispersion was implemented the *FOM* dependency with the tube potential did not change, and in terms of optimization, the optimum interval is what matters. Therefore, for the cases studied a detailed detector modeling is not necessary, gaining up to 50% in terms of simulation velocity.

Future studies can be focused on other detector materials' impact on image acquisition, use anthropomorphic phantoms to obtain images closer to patient anatomy, implement different energy thresholds for the PCDs, and subtract images with different thresholds resulting in multi-spectral images. Moreover, the THOR code gives insight into the image formation process and has a great possibility of being applied outside of the scope of this work. For instance, to investigate and characterize new detector materials and configurations, used in mammography studies, since is also validated for this energy and the detection process in mammography is identical to the detection process in chest radiography, with little geometry adjustments the THOR code can be also used in computed tomography studies, where the PCD are now commercially available.

Bibliography

---

1. Frankel, R. I. Centennial of Röntgen's discovery of x-rays. *Western journal of medicine* **164,** 497. https://doi.org/10.1007/BF00745596 (1996).
2. Bushberg, J. T. & Boone, J. M. *The essential physics of medical imaging* (Lippincott Williams & Wilkins, 2011).
3. Hessenbruch, A. A brief history of x-rays. *Endeavour* **26,** 137–141. https://doi.org/10.1016/S0160-9327(02)01465-5 (2002).
4. Rowlands, J. A. Current advances and future trends in X-ray digital detectors for medical applications. *IEEE Transactions on Instrumentation and Measurement* **47,** 1415–1418. https://doi.org/10.1109/19.746705 (1998).
5. De Souza, R. M., Baldisserotto, M., Piva, J. P. & Icaza, E. E. S. Uso da radiografia de tórax na unidade de tratamento intensivo pediátrico. *Scientia Medica* **23** (2013).
6. Alves, A. F. F., de Arruda Miranda, J. R., Neto, F. A. B., Duarte, S. B. & de Pina, D. R. Construction of pediatric homogeneous phantoms for optimization of chest and skull radiographs. *European journal of radiology* **84,** 1579–1585. https://doi.org/10.1016/j.ejrad.2015.05.015 (2015).
7. Bosso, P. A. R. *et al.* Human respiratory syncytial virus detection in children admitted at a community hospital in Botucatu, SP, Brazil. *Brazilian Journal of Microbiology* **35,** 348–351. https://doi.org/10.1590/S1517-83822004000300015 (2004).
8. Chibane, S. *et al.* Accuracy of Patient Age Estimation from Frontal Chest Radiographs of Adult Patients. *Open Journal of Radiology* **12,** 37–48. https://doi.org/10.4236/ojrad.2022.122005 (2022).
9. DATASUS: Departamento de Informática do SUS. *Ministério da Saúde.* http://tabnet.datasus.gov.br/ (2022).
10. Luz, E. *et al.* Towards an effective and efficient deep learning model for COVID-19 patterns detection in X-ray images. *Research on Biomedical Engineering.* ISSN: 2446-4732. https://link.springer.com/10.1007/s42600-021-00151-6 (Apr. 2021).

11. Willis, C. E. Optimizing digital radiography of children. *European journal of radiology* **72,** 266–273. https://doi.org/10.1016/j.ejrad.2009.03.003 (2009).
12. Hall, E. J. Lessons we have learned from our children: cancer risks from diagnostic radiology. *Pediatric radiology* **32,** 700–706. https://doi.org/10.1007/s00247-002-0774-8 (2002).
13. International Atomic Energy Agency. *Dosimetry in Diagnostic Radiology for Paediatric Patients IAEA Human Health Series* **24.** http://www-pub.iaea.org/books/IAEABooks/8965/Dosimetry-in-Diagnostic-Radiology-for-Paediatric-Patients (International Atomic Energy Agency, Vienna, 2014).
14. Roebuck, D. Risk and benefit in paediatric radiology. *Pediatric Radiology* **29,** 637–640. https://doi.org/10.1007/s002470050666 (1999).
15. Ibiapina, C. d. C., Alvim, C. G., Rocha, F. G., Costa, G. A. & Silva, P. C. Pneumonias comunitárias na infância: etiologia, diagnóstico e tratamento. *Rev Med Minas Gerais* **14,** S19–S25 (2004).
16. Wardlaw, T. M., Johansson, E. W. & Hodge, M. J. *Pneumonia: the forgotten killer of children* (Unicef, 2006).
17. Don, S. *et al.* Image gently campaign back to basics initiative: ten steps to help manage radiation dose in pediatric digital radiography. *American Journal of Roentgenology* **200,** W431–W436 (2013).
18. Doi, K. Diagnostic imaging over the last 50 years: research and development in medical imaging science and technology. *Physics in Medicine and Biology* **51,** R5. https://doi.org/10.1088/0031-9155/51/13/R02 (2006).
19. Dougherty, G. *Digital image processing for medical applications* (Cambridge University Press, 2009).
20. Alexander, S. Image acquisition and quality in digital radiography. *Radiologic Technology* **88,** 53–66 (2016).
21. Dovganich, A., Khvostikov, A., Krylov, A. & Parolina, L. Automatic quality control in lung X-ray imaging with deep learning. *Computational Mathematics and Modeling* **32,** 276–285. https://doi.org/10.1007/s10598-021-09539-6 (2021).
22. Haygood, T. M. *et al.* Why does it take longer to read digital than film-screen screening mammograms? A partial explanation. *Journal of digital imaging* **23,** 170–180. https://doi.org/10.1007/s10278-009-9177-9 (2010).
23. Chistyakov, A., Soto, M. T., Martí, E. & Carrabina, J. An HTML tool for production of interactive stereoscopic compositions. *Journal of medical systems* **40,** 1–9. https://doi.org/10.1007/s10916-016-0616-0 (2016).
24. Bick, U. & Diekmann, F. *Digital mammography* (Springer, 2010).

25. Cowen, A., Kengyelics, S. & Davies, A. Solid-state, flat-panel, digital radiography detectors and their physical imaging characteristics. *Clin Radiol* **63,** 487–498. https://doi.org/10.1016/j.crad.2007.10.014 (2008).
26. Yaffe, M. & Rowlands, J. X-ray detectors for digital radiography. *Physics in Medicine & Biology* **42,** 1. https://doi.org/10.1088/0031-9155/42/1/001 (1997).
27. Zhou, W. *et al.* Comparison of a Photon-Counting-Detector CT with an Energy-Integrating-Detector CT for Temporal Bone Imaging: A Cadaveric Study. *Am. J. Neuroradiol.* **39,** 1733–1738. ISSN: 0195-6108. http://doi.org/10.3174/ajnr.A5768 (9 Sept. 2018).
28. Rowlands, J. A. The physics of computed radiography. *Phys Med Biol* **47,** R123. stacks.iop.org/PMB/47/R123 (23 2002).
29. Kabir, M. Z. & Kasap, S. *Photoconductors for X-Ray Image Detectors* 1125–1145. http://doi.org/10.1007/978-3-319-48933-9_45 (2017).
30. Danielsson, M., Persson, M. & Sjölin, M. Photon-counting x-ray detectors for CT. *Phys Med Biol* **66,** 03TR01. ISSN: 0031-9155. http://doi.org/10.1088/1361-6560/abc5a5 (3 Feb. 2021).
31. Russo, P. *Handbook of X-ray imaging: physics and technology* (CRC press, 2017).
32. Andreo, P. Monte Carlo techniques in medical radiation physics. *Physics in Medicine and Biology* **36,** 861. http://doi.org/10.1088/0031-9155/36/7/001 (1991).
33. Harrison, R. L. *Introduction to Monte Carlo simulation* in *AIP Conference Proceedings* **1204** (2010), 17–21. https://doi.org/10.1063/1.3295638.
34. Lee, S. C., Wang, J. N., Liu, S. C. & Jiang, S. H. Evaluation of dose–image-quality optimization in digital chest radiography. *Nucl. Instrum. Methods. Phys. Res. B* **580,** 544–547. http://doi.org/https://doi.org/10.1016/j.nima.2007.05.226 (1 2007).
35. Mendes, H. R., Silva, J. C., Marcondes, M. & Tomal, A. Optimization of image quality and dose in adult and pediatric chest radiography via Monte Carlo simulation and experimental methods. *Radiation Physics and Chemistry* **201,** 110396. ISSN: 0969806X. http://doi.org/10.1016/j.radphyschem.2022.110396 (Nov. 2022).
36. Ullman, G., Sandborg, M., Dance, D. R., Hunt, R. A. & Carlsson, G. A. Towards optimization in digital chest radiography using Monte Carlo modelling. *Phys Med Biol* **51,** 2729. http://doi.org/10.1088/0031-9155/51/11/003 (11 2006).
37. Salvat, F., Fernández-Varea, J. M. & Sempau, J. *PENELOPE-2014: A code system for Monte Carlo simulation of electron and photon transport* in *the Workshop Proceedings, June* (2014).

38. Barufaldi, B. *et al.* Virtual clinical trials in medical imaging system evaluation and optimisation. *Radiation Protection Dosimetry* **195,** 363–371. https://doi.org/10.1093/rpd/ncab080 (2021).

39. Abadi, E. *et al.* Virtual clinical trials in medical imaging: a review. *Journal of Medical Imaging* **7,** 042805–042805. https://doi.org/10.1117/1.JMI.7.4.042805 (2020).

40. Badal, A., Sharma, D., Graff, C. G., Zeng, R. & Badano, A. Mammography and breast tomosynthesis simulator for virtual clinical trials. *Computer Physics Communications* **261,** 107779. ISSN: 00104655. http://doi.org/10.1016/j.cpc.2020.107779 (Apr. 2021).

41. Esquivel, A. *et al.* Photon-Counting Detector CT: Key Points Radiologists Should Know. *Korean Journal of Radiology* **23,** 854–865. https://doi.org/10.3348%2Fkjr.2022.0377 (2022).

42. Badal Soler, A. *Development of advanced geometric models and acceleration techniques for Monte Carlo simulation in Medical Physics* PhD thesis (Universitat Politècnica de Catalunya, Barcelona, Spain, 2008).

43. Massera, R. T., Fernández-Varea, J. M. & Tomal, A. Impact of photoelectric cross section data on systematic uncertainties for Monte Carlo breast dosimetry in mammography. *Physics in Medicine & Biology* **66,** 115015. https://doi.org/10.1088/1361-6560/abf859 (2021).

44. Chan, H.-P. & Doi, K. The validity of Monte Carlo simulation in studies of scattered radiation in diagnostic radiology. *Physics in Medicine and Biology* **28,** 109. https://doi.org/10.1088/0031-9155/28/2/001 (1983).

45. Attix, F. H. *Introduction to radiological physics and radiation dosimetry* (John Wiley and Sons, 2008).

46. Yoshimura, E. M. Física das Radiações: interação da radiação com a matéria. *Revista Brasileira de Física Médica* **3,** 57–67. http://doi.org/https://doi.org/10.29384/rbfm.2009.v3.n1.p57-67 (1 2009).

47. Jackson, D. F. & Hawkes, D. J. X-ray attenuation coefficients of elements and mixtures. *Physics Reports* **70,** 169–233. https://doi.org/10.1016/0370-1573(81)90014-4 (1981).

48. Noel, A. & Thibault, F. Digital detectors for mammography: the technical challenges. *European Radiology* **14,** 1990–1998. ISSN: 0938-7994. http://doi.org/10.1007/s00330-004-2446-6 (11 Nov. 2004).

49. Samei, E. & Flynn, M. J. An experimental comparison of detector performance for direct and indirect digital radiography systems. *Med Phys* **30,** 608–622. https://doi.org/10.1118/1.1561285 (2003).

50. Bertolini, M. *et al.* A comparison of digital radiography systems in terms of effective detective quantum efficiency. *Med Phys* **39,** 2617–2627. http://doi.org/10.1118/1.4704500 (5 2012).

51. Kasap, S. O. & Rowlands, J. A. Direct-conversion flat-panel X-ray image sensors for digital radiography. *Proceedings of the IEEE* **90,** 591–604. ISSN: 00189219. http://doi.org/10.1109/JPROC.2002.1002529 (4 2002).

52. Knoll, G. F. *Radiation detection and measurement* (John Wiley & Sons, 2010).

53. Que, W & Rowlands, J. X-ray photogeneration in amorphous selenium: Geminate versus columnar recombination. *Physical Review B* **51,** 10500. https://doi.org/10.1103/PhysRevB.51.10500 (1995).

54. Kabir, M., Arnab, S. M. & Hijazi, N. Electron–hole pair creation energy in amorphous selenium: geminate versus columnar recombination. *Journal of Materials Science: Materials in Electronics* **30,** 21059–21063. https://doi.org/10.1007/s10854-019-02475-7 (2019).

55. Bubon, O., Jandieri, K., Baranovskii, S. D., Kasap, S. O. & Reznik, A. Columnar recombination for X-ray generated electron-holes in amorphous selenium and its significance in a-Se x-ray detectors. *Journal of Applied Physics* **119.** ISSN: 10897550. http://doi.org/10.1063/1.4944880 (12 2016).

56. Street, R. A. *et al.* Comparison of PbI2 and HgI2 for direct detection active matrix x-ray image sensors. *Journal of Applied Physics* **91,** 3345–3355. ISSN: 0021-8979. http://doi.org/10.1063/1.1436298 (5 Mar. 2002).

57. Huang, H. & Abbaszadeh, S. Recent Developments of Amorphous Selenium-Based X-Ray Detectors: A Review. *IEEE Sensors Journal* **20,** 1694–1704. ISSN: 1530-437X. http://doi.org/10.1109/JSEN.2019.2950319 (4 Feb. 2020).

58. Zhao, W., Ji, W. G., Debrie, A. & Rowlands, J. A. Imaging performance of amorphous selenium based flat-panel detectors for digital mammography: Characterization of a small area prototype detector. *Med Phys* **30,** 254–263. ISSN: 00942405. http://doi.org/10.1118/1.1538233 (2 Jan. 2003).

59. Marshall, N. W. Detective quantum efficiency measured as a function of energy for two full-field digital mammography systems. *Phys Med Biol* **54,** 2845–2861. ISSN: 0031-9155. http://doi.org/10.1088/0031-9155/54/9/017 (9 May 2009).

60. Yunus, M. *Monte Carlo modeling of the sensitivity of x-ray photoconductors* PhD thesis (2005).

61. Kasap, S., Kabir, M. Z. & Rowlands, J. Recent advances in X-ray photoconductors for direct conversion X-ray image detectors. *Current Applied Physics* **6,** 288–292. ISSN: 15671739. http://doi.org/10.1016/j.cap.2005.11.001 (3 June 2006).

62. Owens, A. & Peacock, A. Compound semiconductor radiation detectors. *Nuclear Instruments and Methods in Physics Research Section A: Accelerators, Spectrometers, Detectors and Associated Equipment* **531,** 18–37. ISSN: 01689002. http://doi.org/10.1016/j.nima.2004.05.071 (1-2 Sept. 2004).

63. Fang, Y. *Monte Carlo Transport Methods for Semiconductor X-ray Imaging Detectors* PhD thesis (2013).

64. Willemink, M. J., Persson, M., Pourmorteza, A., Pelc, N. J. & Fleischmann, D. Photon-counting CT: technical principles and clinical prospects. *Radiology* **289,** 293–312. https://doi.org/10.1148/radiol.2018172656 (2018).

65. Persson, M., Wang, A. & Pelc, N. J. Detective quantum efficiency of photon-counting CdTe and Si detectors for computed tomography: a simulation study. *Journal of Medical Imaging* **7,** 1. ISSN: 2329-4302. http://doi.org/10.1117/1.JMI.7.4.043501 (2020).

66. Hamann, E. *et al.* Performance of a Medipix3RX spectroscopic pixel detector with a high resistivity gallium arsenide sensor. *IEEE transactions on medical imaging* **34,** 707–715. http://doi.org/10.1109/TMI.2014.2317314 (2014).

67. Koenig, T. *et al.* Imaging properties of small-pixel spectroscopic x-ray detectors based on cadmium telluride sensors. *Physics in Medicine & Biology* **57,** 6743. https://doi.org/10.1088/0031-9155/57/21/6743 (2012).

68. Pennicard, D *et al.* *The LAMBDA photon-counting pixel detector* in *Journal of Physics: Conference Series* **425** (2013), 062010. https://doi.org/10.1088/1742-6596/425/6/062010.

69. Berger, M. J. XCOM: Photon cross section database. *NIST.* http://physics.nist.gov/xcom (1999).

70. *X-Ray Data Booklet* (2009).

71. Gravel, P., Beaudoin, G. & Guise, J. A. D. A method for modeling noise in medical images. *IEEE Transactions on medical imaging* **23,** 1221–1232. http://doi.org/10.1109/TMI.2004.832656 (10 2004).

72. Fang, Y., Badal, A., Allec, N., Karim, K. S. & Badano, A. Spatiotemporal Monte Carlo transport methods in x-ray semiconductor detectors: Application to pulse-height spectroscopy in a-Se. *Medical Physics* **39,** 308–319. https://doi.org/10.1118/1.3669486 (2012).

73. Fang, Y., Karim, K. S. & Badano, A. Effect of burst and recombination models for Monte Carlo transport of interacting carriers in a-Se x-ray detectors on Swank noise. *Med Phys* **41,** 011904. ISSN: 00942405. http://doi.org/10.1118/1.4842435 (1 Dec. 2013).

74. Gutierrez, B., Badano, A. & Samuelson, F. Analytic variance estimates of Swank and Fano factors. *Med Phys* **41,** 072102. ISSN: 00942405. http://doi.org/10.1118/1.4881328 (7 June 2014).

75. Chan, H.-P. & Doi, K. Studies of x-ray energy absorption and quantum noise properties of x-ray screens by use of Monte Carlo simulation. *Med Phys* **11,** 37–46. ISSN: 00942405. http://doi.org/10.1118/1.595474 (1 Jan. 1984).

76. Swank, R. K. Absorption and noise in x-ray phosphors. *Journal of Applied Physics* **44,** 4199–4203. https://doi.org/10.1063/1.1662918 (9 1973).

77. Khodajou-Chokami, H., Hosseini, S. A., Ghorbanzadeh, M. & Mohammadi, M. *QCT: A Measuring Tool Dedicated to the Estimation of Image Parameters for Quality Assurance/Quality Control Programs of CT Scanners* in (IEEE, June 2020), 1–6. ISBN: 978-1-7281-5386-5. http://doi.org/10.1109/MeMeA49120.2020.9137199.

78. Whitman, G. J. & Haygood, T. M. *Digital mammography: a practical approach* (Cambridge University Press, 2012).

79. Yao, M., Duvauchelle, P., Kaftandjian, V., Petersol-Parmentier, A. & Schumm, A. *Simulating radiographic inspections with imaging plates* in (2016), 110005. http://doi.org/10.1063/1.4940576.

80. Fasbender, R., Li, H. & Winnacker, A. Monte Carlo modeling of storage phosphor plate readouts. *Nuclear Instruments and Methods in Physics Research Section A: Accelerators, Spectrometers, Detectors and Associated Equipment* **512,** 610–618. ISSN: 01689002. http://doi.org/10.1016/S0168-9002(03)02012-6 (3 Oct. 2003).

81. Badano, A. & Sempau, J. MANTIS: combined x-ray, electron and optical Monte Carlo simulations of indirect radiation imaging systems. *Phys Med Biol* **51,** 1545–1561. ISSN: 0031-9155. http://doi.org/10.1088/0031-9155/51/6/013 (6 Mar. 2006).

82. Sharma, D., Badal, A. & Badano, A. hybridMANTIS: a CPU–GPU Monte Carlo method for modeling indirect x-ray detectors with columnar scintillators. *Phys Med Biol* **57,** 2357–2372. ISSN: 0031-9155. http://doi.org/10.1088/0031-9155/57/8/2357 (8 Apr. 2012).

83. Badal, A. & Badano, A. Accelerating Monte Carlo simulations of photon transport in a voxelized geometry using a massively parallel graphics processing unit. *Med Phys* **36,** 4878–4880. ISSN: 00942405. http://doi.org/10.1118/1.3231824 (11 Oct. 2009).

84. Salvat, F., Fernández-Varea, J. M. & Sempau, J. *PENELOPE-2006: A code system for Monte Carlo simulation of electron and photon transport* in *Workshop proceedings* **4** (2006), 7.

85. Sundberg, C., Persson, M., Wikner, J. J. & Danielsson, M. 1-μm spatial resolution in silicon photon-counting CT detectors. *Journal of Medical Imaging* **8.** ISSN: 2329-4302. http://doi.org/10.1117/1.JMI.8.6.063501 (2021).

86. Magalhaes, D. & Tomal, A. Monte Carlo simulation of hybrid pixel detectors. *Radiation Physics and Chemistry* **167,** 108296. https://doi.org/10.1016/j.radphyschem.2019.04.046 (2020).

87. Nilsson, H.-E, Dubarić, E, Hjelm, M & Bertilsson, K. Simulation of photon and charge transport in X-ray imaging semiconductor sensors. *Nuclear Instruments and Methods in Physics Research Section A: Accelerators, Spectrometers, Detectors and Associated Equipment* **487,** 151–162. ISSN: 01689002. http://doi.org/10.1016/S0168-9002(02)00959-2 (1-2 July 2002).

88. Alsager, A. & Spyrou, N. Evaluation of image performance of CZT detector for digital mammography: Monte Carlo simulation. *Nuclear Instruments and Methods in Physics Research Section A: Accelerators, Spectrometers, Detectors and Associated Equipment* **580,** 462–465. ISSN: 01689002. http://doi.org/10.1016/j.nima.2007.05.128 (1 Sept. 2007).

89. Werner, C. J. *et al. MCNP version 6.2 release notes* (Los Alamos National Lab.(LANL), Los Alamos, NM (United States), 2018).

90. Korn, A., Giersch, J. & Hoheisel, M. *Simulation of internal backscatter effects on MTF and SNR of pixelated photon-counting detectors* in (ed Flynn, M. J.) (Apr. 2005), 292. http://doi.org/10.1117/12.595219.

91. Hoheisel, M., Giersch, J., Mitschke, M. & Bernhardt, P. *Absorbers for medical x-ray detectors with optimum spatial resolution: a simulation study* in (eds Yaffe, M. J. & Flynn, M. J.) (May 2004), 386. https://doi.org/10.1117/12.535305.

92. Giersch, J., Weidemann, A. & Anton, G. ROSI—an object-oriented and parallel-computing Monte Carlo simulation for X-ray imaging. *Nuclear Instruments and Methods in Physics Research Section A: Accelerators, Spectrometers, Detectors and Associated Equipment* **509,** 151–156. ISSN: 01689002. http://doi.org/10.1016/S0168-9002(03)01564-X (1-3 Aug. 2003).

93. Saleem, T., Iguaz, F. & Orsini, F. Allpix squared simulations of multi-element germanium detectors for synchrotron applications. *Journal of Instrumentation* **17,** P02013. https://doi.org/10.1088/1748-0221/17/02/P02013 (2022).

94. Day, J. A. & Tanguay, J. The detective quantum efficiency of cadmium telluride photon-counting x-ray detectors in breast imaging applications. *Med Phys* **49,** 1481–1494. ISSN: 0094-2405. http://doi.org/10.1002/mp.15411 (3 Mar. 2022).

95. Agostinelli, S. *et al.* Geant4—a simulation toolkit. *Nuclear Instruments and Methods in Physics Research Section A: Accelerators, Spectrometers, Detectors and Associated Equipment* **506,** 250–303. ISSN: 01689002. http://doi.org/10.1016/S0168-9002(03)01368-8 (3 July 2003).

96. Stierstorfer, K. Modeling the frequency-dependent detective quantum efficiency of photon-counting x-ray detectors. *Med Phys* **45,** 156–166. ISSN: 00942405. http://doi.org/10.1002/mp.12667 (1 Jan. 2018).

97. Hjelm, M & Nilsson, H.-E. Full Band Monte Carlo Simulation of Cubic and Hexagonal Silicon Carbide Polytypes and Devices. *Physica Scripta* **T114,** 61–65. ISSN: 0031-8949. http://doi.org/10.1088/0031-8949/2004/T114/014 (Jan. 2004).

98. Gislason, A. J., Davies, A. G. & Cowen, A. R. Dose optimization in pediatric cardiac X-ray imaging. *Medical Physics* **37,** 5258–5269. https://doi.org/10.1118/1.3488911 (2010).

99. Gould, M. R. The UK Radiological Congress-Medical Imaging 2014 - Potential dose optimisation in paediatric digital radiography (2014).

100. Boone, J. M. & Seibert, J. A. A figure of merit comparison between bremsstrahlung and monoenergetic X-ray sources for angiography. *Journal of X-ray Science and Technology* **4,** 334–345. https://doi.org/10.1016/S0895-3996(05)80050-3 (1994).

101. Penchev, P, Klingmüller, V, Alzen, G & Fiebich, M. *Optimization of image quality and patient dose in paediatric radiology using Monte Carlo modeling* in *4th European Conference of the International Federation for Medical and Biological Engineering* (2009), 2528–2531.

102. Doyle, P, Martin, C. J. & Gentle, D. Application of contrast-to-noise ratio in optimizing beam quality for digital chest radiography: comparison of experimental measurements and theoretical simulations. *Phys Med Biol* **51,** 2953–2970. ISSN: 0031-9155. http://doi.org/10.1088/0031-9155/51/11/018 (11 June 2006).

103. Apriliastri, N. N. *et al.* Optimization of simulated cranial, thorax, and abdominal examination in paediatric digital radiography. *Journal of Physics: Conference Series* **1248,** 012023. ISSN: 1742-6588. http://doi.org/10.1088/1742-6596/1248/1/012023 (June 2019).

104. Freitas, M. B. *et al.* Patient dose optimization for computed radiography using physical and observer-based measurements as image quality metrics. *Radiation Physics and Chemistry* **172,** 108768. ISSN: 0969806X. http://doi.org/10.1016/j.radphyschem.2020.108768 (July 2020).

105. Martin, C. The importance of radiation quality for optimisation in radiology. *Biomedical Imaging and Intervention Journal* **3.** ISSN: 1823-5530. http://doi.org/10.2349/biij.3.2.e38 (2 Apr. 2007).

106. Launders, J. H., Cowen, A. R., Bury, R. F. & Hawkridge, P. Towards image quality, beam energy and effective dose optimisation in digital thoracic radiography. *European Radiology* **11,** 870–875. ISSN: 0938-7994. http://doi.org/10.1007/s003300000525 (5 Apr. 2001).

107. Salvagnini, E., Bosmans, H., Struelens, L. & Marshall, N. W. *Effective detective quantum efficiency (eDQE) and effective noise equivalent quanta (eNEQ) for system optimization purposes in digital mammography* in (eds Pelc, N. J., Nishikawa, R. M. & Whiting, B. R.) (Feb. 2012), 83130H. http://doi.org/10.1117/12.911193.

108. Rivetti, S. *et al.* Comparison of different computed radiography systems: Physical characterization and contrast detail analysis. *Med Phys* **37,** 440–448. ISSN: 00942405. http://doi.org/10.1118/1.3284539 (2 Jan. 2010).

109. Samei, E. *et al.* Effective DQE (eDQE) and speed of digital radiographic systems: An experimental methodology. *Med Phys* **36,** 3806–3817. ISSN: 00942405. http://doi.org/10.1118/1.3171690 (8 July 2009).

110. IEC. *IEC 62220-1-1 - Medical Electrical Equipment-Characteristics of Digital X-Ray Imaging Devices - Part 1-1: Determination of the Detective Quantum Efficiency-Detectors used in radiographic imaging* (International Electrotechnical Commission, Geneva, Switzerland, 2015).

111. di Franco, F. *et al.* GEANT4 Monte Carlo simulations for virtual clinical trials in breast X-ray imaging: Proof of concept. *Physica Medica* **74,** 133–142. ISSN: 1120-1797. https://doi.org/10.1016/j.ejmp.2020.05.007 (2020).

112. Sarno, A & Tucciariello, R. Simulated sensor characterization for virtual clinical trials in mammography and digital breast tomosynthesis. *Journal of Instrumentation* **17,** C01041. https://doi.org/10.1088/1748-0221/17/01/C01041 (2022).

113. Abadi, E., Segars, W. P., Chalian, H. & Samei, E. Virtual imaging trials for coronavirus disease (COVID-19). *AJR. American journal of roentgenology* **216,** 362. https://doi.org/10.2214%2FAJR.20.23429 (2021).

114. Abadi, E. *et al.* Virtual clinical trial for quantifying the effects of beam collimation and pitch on image quality in computed tomography. *Journal of Medical Imaging* **7,** 042806–042806. `https://doi.org/10.1117/1.JMI.7.4.042806` (2020).

115. Abadi, E. *et al. Development and clinical applications of a virtual imaging framework for optimizing photon-counting CT* in *Medical Imaging 2022: Physics of Medical Imaging* **12031** (2022), 426–432. `https://doi.org/10.1117/12.2612079`.

116. Sechopoulos, I. *et al.* Monte Carlo reference data sets for imaging research: Executive summary of the report of AAPM Research Committee Task Group 195. *Med Phys* **42,** 5679–5691. ISSN: 00942405. `http://doi.org/10.1118/1.4928676` (10 2015).

117. Kyprianou, I. S., Brackman, G., Myers, K. J., Badal, A. & Badano, A. *An efficient depth-and energy-dependent Monte Carlo model for columnar CsI detectors* in *Medical Imaging 2008: Physics of Medical Imaging* **6913** (2008), 69130O. `https://doi.org/10.1117/12.772878`.

118. Hijazi, N., Panneerselvam, D. & Kabir, M. Electron–hole pair creation energy in amorphous selenium for high energy photon excitation. *Journal of Materials Science: Materials in Electronics* **29,** 486–490. `https://doi.org/10.1007/s10854-017-7937-8` (2018).

119. Lachaine, M & Fallone, B. Monte Carlo simulations of x-ray induced recombination in amorphous selenium. *Journal of Physics D: Applied Physics* **33,** 1417. `https://doi.org/10.1088/0022-3727/33/11/323` (2000).

120. Hobbie, R. K. & Roth, B. J. *Intermediate physics for medicine and biology* (Springer Science & Business Media, 2007).

121. Box, G. E. P. & Muller, M. E. A Note on the Generation of Random Normal Deviates. *The Annals of Mathematical Statistics* **29,** 610–611. ISSN: 0003-4851. `http://doi.org/10.1214/aoms/1177706645` (2 June 1958).

122. Cross, B., Bale, G., Lowe, B. & Sareen, R. Monte-Carlo modeling of silicon X-ray detectors. *Adv. X-Ray Anal.* **49,** 274–279 (2005).

123. Lubberts, G. Random noise produced by x-ray fluorescent screens. *JOSA* **58,** 1475–1483. `https://doi.org/10.1364/JOSA.58.001475` (1968).

124. Fang, Y. *et al.* Detective quantum efficiency simulation of a-Se imaging detectors using ARTEMIS. *Medical Physics* **44,** 4035–4039. `https://doi.org/10.1002/mp.12389` (2017).

125. Fang, Y. & Badano, A. *DQE simulation of a-Se x-ray detectors using ARTEMIS* in *Medical Imaging 2016: Physics of Medical Imaging* **9783** (2016), 277–282. `https://doi.org/10.1117/12.2214805`.

126. Fang, Y., Badal, A., Badano, A. & Karim, K. S. *Spatial resolution characteristics of a-Se imaging detectors using Monte Carlo methods with detailed spatiotemporal transport of x-rays, electrons, and electron-hole pairs under applied bias* in. **8668** (2013), 86683R. https://doi.org/10.1117/12.2007436.

127. Cheng, Y.-H., Wang, Y.-W., Lin, J.-A. & Fang, Y. *MTF simulation of a-Se x-ray detector using ARTEMIS for breast imaging applications* in (IEEE, Nov. 2018), 1–5. ISBN: 978-1-5386-8494-8. http://doi.org/10.1109/NSSMIC.2018.8824670.

128. Poludniowski, G, Landry, G, DeBlois, F, Evans, P. & Verhaegen, F. SpekCalc: a program to calculate photon spectra from tungsten anode X-ray tubes. *Physics in medicine and biology* **54,** N433. https://doi.org/10.1088/0031-9155/54/19/N01 (2009).

129. Of Radiology, A. C. *ACR–SPR–STR Practice parameter for the performance of chest radiography* 2018.

Appendix A

Publications

This chapter presents the work developed during the doctorate. Articles published in journals, articles accepted for publication and published in conference proceedings.

Articles published in journals

- Mendes, H.R.; Silva, J.C. ; Marcondes, M.; Tomal, A. *Optimization of image quality and dose in adult and pediatric chest radiography via Monte Carlo simulation and experimental methods.* Radiation Physics and Chemistry, v. 201, p. 110396, 2022. https://doi.org/10.1016/j.radphyschem.2022.110396

- Mendes, H.R.; Massera, R.T.; Tomal, A. *pyPEN: uma interface gráfica user-friendly para simulação Monte Carlo em física médica.* Revista Brasileira de Ensino de Física, v. 44, p. e20220006-1, 2022. https://doi.org/10.1590/1806-9126-RBEF-2022-0006.

- Mendes, H.R.; Silva, J.C.; Tomal, A. *Simulação Monte Carlo em radiografia de tórax: estudos de dose e qualidade da imagem.* Revista Brasileira de Física Médica, v. 13, p. 145-153, 2019. http://dx.doi.org/10.29384/rbfm.2019.v13.n1.p145-153.

Full articles in conference proceedings

- Mendes, H.R.; Tomal, A. *Detailed Monte Carlo simulation of energy integrating and photon counting semiconductor detectors.* Physics of Medical Imaging, 2022, San Diego. Medical Imaging 2022: Physics of Medical Imaging, 2022. p. 149. http://dx.doi.org/10.1117/12.2607891.

Extended abstracts published in conference proceeding

- Mendes, H.R.; Tomal, A. *Estudo da qualidade da imagem em objetos simuladores homogêneos e antropomórficos via simulação Monte Carlo.* XXVI Congresso Brasileiro de Física Médica, 2022, Fortaleza - CE.

- Mendes, H.R.; Tomal, A. *Impact of detailed semiconductor detector Monte Carlo modeling in chest radiography optimization.* International Conference on Monte Carlo Techniques for Medical Applications, 2022, Antwerp.

- Tomal, A.; Mendes, H.R.; COSTA, P.R. P*aediatric radiology: optimized X-ray spectra versus clinical data and the impact on dose reduction.* International Conference on Radiation Safety: Improving Radiation Protection in Practice, 2020, p. 195-196.

- Mendes, H.R.; Tomal, A. *Caracterização dos detectores de radiografia computadorizada utilizados no Hospital da Mulher - CAISM/Unicamp.* Anais XXIV Congresso Brasileiro de Física Médica, 2019.

- Mendes, H.R.; Tomal, A. *Estudo da performance de grade antiespalhamento para pacientes pediátricos e adultos via simulação Monte Carlo.* Anais XXIV Congresso Brasileiro de Física Médica, 2019.

- Marcondes, M.; Mendes, H.R.; Tomal, A. *Otimização da Qualidade da Imagem e a Dose de Radiação em Exames de Radiografia Computadorizada de Tórax.* Anais XXIV Congresso Brasileiro de Física Médica, 2019.

- Silva, J.C; Mendes, H.R.; Tomal, A. *Otimização dos Parâmetros de Exposição em Radiologia Digital de Tórax Utilizando Simulação Monte Carlo.* Anais XXIV Congresso Brasileiro de Física Médica, 2019.

- Mendes, H.R.; Massera, R.T.; Tomal, A. *Evaluation of antiscatter grid performance in pediatric patients via Monte Carlo Simulation.* Annals International Conference on Monte Carlo Techniques for Medical Applications, 2019.

- Mendes, H.R.; Tomal, A. *Simulação Monte Carlo do Fator de Retroespalhamento para Radiologia Pediátrica usando Objetos Simuladores Homogêneos e Antropomórficos.* Anais XXIII Congresso Brasileiro de Física Médica, 2018.

- Mendes, H.R.; Tomal, A. *Otimização dos Parâmetros de Exposição em Radiologia Pediátrica por meio de Simulação Monte Carlo e Estudos Experimentais.* Anais XXIII Congresso Brasileiro de Física Médica, 2018.

Abstracts published in conference proceedings

- Mendes, H.R.; Tomal, A. *Inclusion of Electron-Hole Creation and Transport in Photon Counting Semiconductor Detectors in the Penelope Monte Carlo Code: Effects on the Radiographic Image Formation.* AAPM 65th Annual Meeting & Exhibition, 2023. Medical Physics, 2023.

- Mendes, H.R.; Tomal, A. *Inclusão da simulação da criação e transporte de pares elétron-buraco em detectores semicondutores no código Monte Carlo PENELOPE: impacto na formação da imagem radiográfica.* Anais XXVII Congresso Brasileiro de Física Médica, 2023

- Mendes, H.R.; Massera, R.T.; Tomal, A. *pyPEN: a graphical user-friendly interface for Monte Carlo simulation in medical physics.* Encontro de Outono da SBF 2022, São Paulo.

- Mendes, H.R.; Benevides, R.; Ferreira, C. P.; Franco, D. O.; Nunes, M.; Pasquini, P. S.; Principe, D.; Santos, F. G. S.; Sato, E. A. *Fisicast: Physics outreach through Podcast.* Encontro de Outono da SBF 2022, São Paulo.

- Mendes, H.R.; Tomal, A. *Estudo de deposição de dose em objetos simuladores antropomórficos pediátrico voxilizados.* Anais XXV Congresso Brasileiro de Física Médica, 2021.

- Mendes, H.R.; Tomal, A. *Phantom Geometry: Impact in the optimization for pediatric radiography.* Anais Encontro de Outono da Sociedade Brasileira de Física, 2021.

- Mendes, H.R.; Tomal, A. *Implementation of Detailed Monte Carlo Simulation for Semiconductor Detectors Using the PENELOPE Code.* AAPM 63rd Annual Meeting & Exhibition, 2021. Medical Physics, 2021. v. 48. p. e117-e635.

- Sato, E.A.; Pasquini, P.S.; Nunes M.; Ferreira, C.P.; Mendes, H.R.; Zavanin, E.; Principe, D.; Benevides, R.; Santos, F.G.S.; Franco, D.O. *Fisicast: Divulgação de Física através de podcasts.* I Encontro sobre Divulgação e Ensino de Física de Partículas, 2020.

Appendix B

PENELOPE Monte Carlo code validation

The Monte Carlo code used in this project was the PENELOPE 2014. A code validation was performed so that the simulation results could be reliable. The validation was performed using the AAPM Report 195 Case 2: Radiography and Body Tomosynthesis [116]. This report compares the results obtained from different Monte Carlo codes for simple geometries. The most recent PENELOPE code, version 2018, was also validated. The version 2018 was not used in this project, however, has been validated for future uses.

Figure B.1 shows the simulation geometry used in the validation. The phantom dimensions were 390 × 390 × 200 cm^2 and is composed of soft tissue, the rest of the geometry is filled with air. A scoring plane with 390 mm sides was located 50 mm past the phantom. The x-ray source was placed 155 cm from the phantom surface. Simulations were performed for a 56.4 keV monoenergetic beam and for a spectrum produced with a tube potential of 120 kV, tungsten target (W) and an aluminum (Al) additional filter of 2.861 mm.

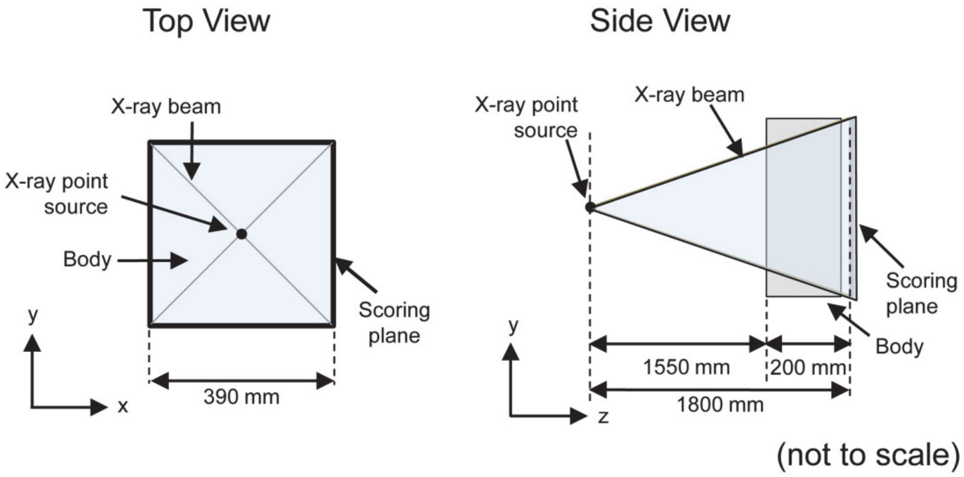

Figure B.1: Simulation geometry used in the validation. Image obtained from the AAPM Report 195 [116].

Nine volumes of interest (*VOI*) were placed in the phantom and seven regions of interest (*ROI*) were placed in the scoring plane. Figures B.2 and B.3 show the positions of the *VOIs* and *ROIs*, respectively.

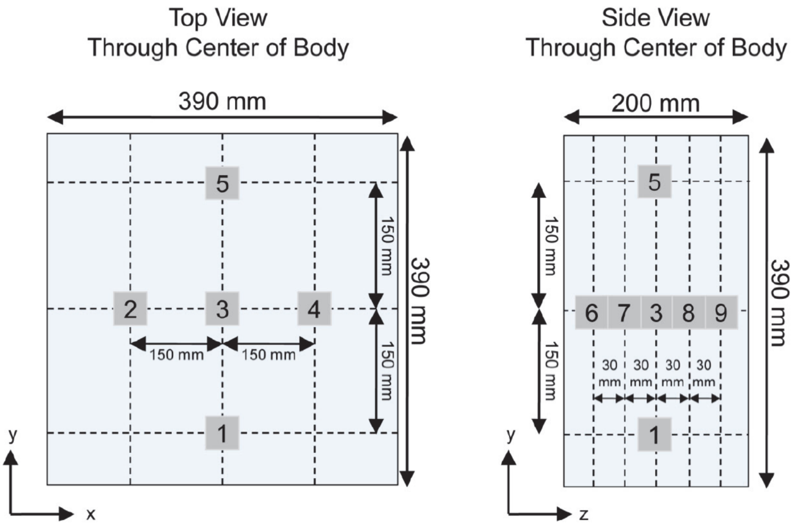

Figure B.2: Positions of the volumes of Interest *VOI* placed in the phantom and. Image obtained from the AAPM Report 195 [116].

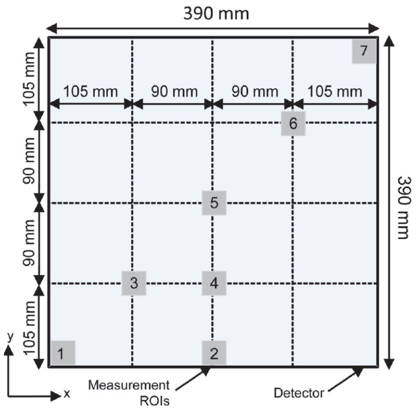

Figure B.3: Positions of the regions of interest *ROI* placed in the scoring plane. Image obtained from the AAPM Report 195 [116].

Figure B.4 (a) shows the total energy deposited on the phantom for the mono and polyenergetic beams. Figure B.4 (b) shows the energy deposited in each volume of interest for the monoenergetic beam. In these cases the whole phantom was irradiated.

The relative difference for the energy deposited in the whole body between the AAPM Report 195 and the PENELOPE 2014 was 0.1% and 0.05% for the mono and polyenergetic beams, respectively. The relative differences between the AAPM Report 195 and the PENELOPE 2018 were 0.13% and 0.12%. For the *VOIs*, the PENELOPE 2014 showed a average relative difference of 1.2±0.8% and 1.1±0.9% for the mono and polyenergetic beams, respectively. For the PENELOPE 2018 case, the values were 1.3±0.7% and 1.2±0.7%.

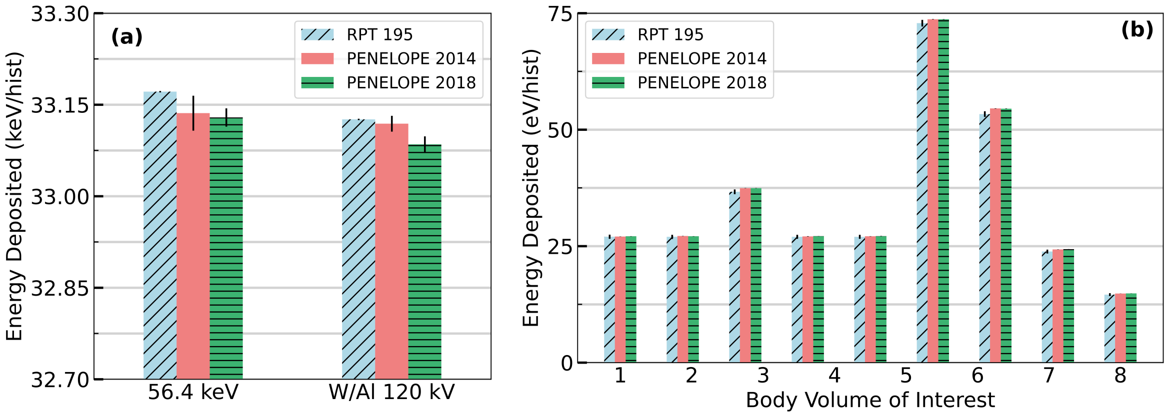

Figure B.4: (a) Total energy deposited on the phantom for the mono and polyenergetic beams. (b) Energy deposited in each volume of interest for the monoenergetic beam.

To evaluate scattering, a pencil beam at the phantom center was used. Figure B.5 (a) shows the energy deposited only from primary photons in the central ROI (ROI 5 on Figure B.3 (b)) for the mono and polyenergetic beams. B.5 (b) shows the energy deposited only by scattered photons in each ROI for the monoenergetic beam.

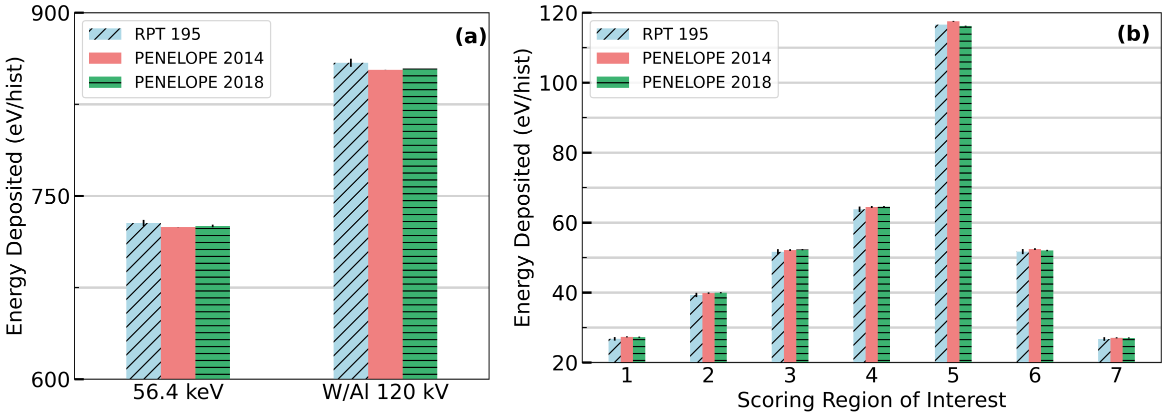

Figure B.5: (a) Energy deposited only by primary photons in the central *ROI* (5 on Figure B.3 (b)) for the mono and polyenergetic beams. (b) Energy deposited only by scattered photons in each ROI for the monoenergetic beam.

The relative difference between the AAPM Report 195 and the PENELOPE 2014 for the energy deposited by primary photons in the center *ROI* was 0.47% and 0.67% for the mono and polyenergetic beams, respectively. The relative differences between the AAPM Report 195 and the PENELOPE 2018 were 0.34% and 0.55%. The energy deposited only by scattered photons showed an average relative difference between the AAPM Report 195 and the PENELOPE 2014 code of 1.3±0.4% and 0.5±0.2% for the mono and polyenergetic beams, respectively. For the PENELOPE 2018 the values were 1.1±0.5% and 0.6±0.3%.

Appendix C

Validation of the "Tally Energy Deposited by Primary Particle"

The "Tally Energy Deposited by Primary Particle" (EDP_p) only considers the primary photons in order to calculate the energy deposited in a material. The tally was created based on the "Tally Energy Deposition" already present in the penEasy v. 2015 code [42]. The reason develop this tally was to reduce the number of simulations, since without it for each exposure condition is necessary to perform two simulations: one to determine the air kerma K_{ar} and the other to calculate the mean absorbed dose in the phantom (MAD). This is necessary because the K_{ar} is calculated only using the incident photons, if the phantom is present, photons that interact with the phantom can be scattered and reach the ionization chamber, and, therefore, increasing the energy deposited in the chamber.

The tally EDP_p was included in the penEasy code and validated by performing simulations with two geometries: (i) only a ionization chamber, represented in the simulations by an 2.5×3.8×2.5 cm^3 air volume, and (ii) is with the chamber and a phantom of soft tissue with 20×20 cm^2 of area and 10 cm thick. Figure C.1 shows the K_{ar} calculated in the situation (i) and (ii), for monoenergetic beam with energies between 10 to 200 keV, the field was divergent field with an area of 20×20 cm^2 at the phantom surface, the distance between the focus and the phantom surface was 100 cm.

Figure C.1 shows that the K_{ar} curve for both cases are almost identical with the relative difference between both cases less than 1.5%.

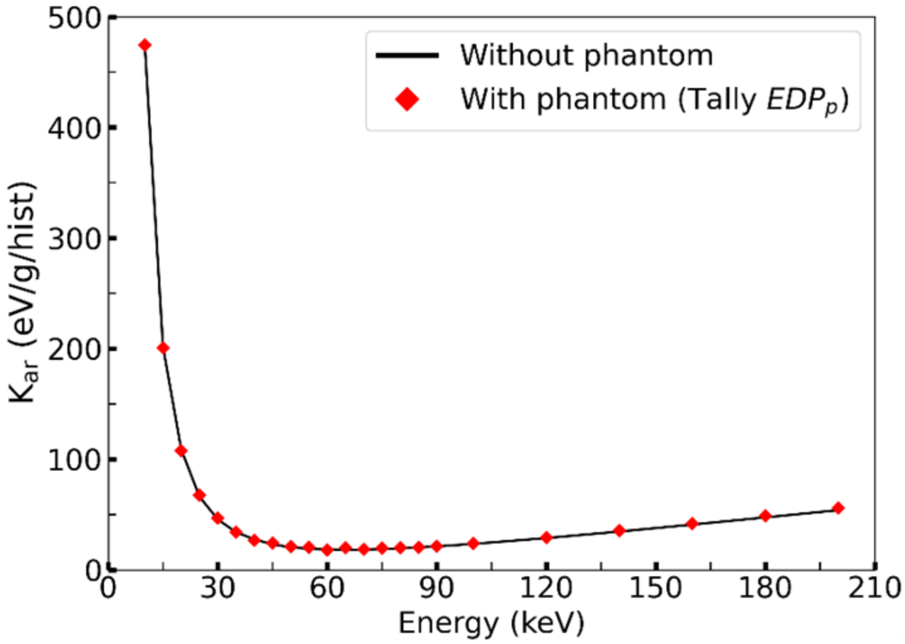

Figure C.1: K_{ar} calculated in the situation (i) only the ionization chamber, and (ii) with the ionization chamber and phantom, for monoenergetic beam with energies between 10 to 200 keV.